May 2019

Petrogenesis of the El Rechuelos Rhyolite, Jemez Mountains Volcanic Field, New Mexico, USA

Kelsy Jo Konkright
kjkonkright@gmail.com

Repository Citation

Konkright, Kelsy Jo, "Petrogenesis of the El Rechuelos Rhyolite, Jemez Mountains Volcanic Field, New Mexico, USA" (2019). *UNLV Theses, Dissertations, Professional Papers, and Capstones*. 3632.
https://digitalscholarship.unlv.edu/thesesdissertations/3632

PETROGENESIS OF THE EL RECHUELOS RHYOLITE,

JEMEZ MOUNTAINS VOLCANIC FIELD,

NEW MEXICO, USA

By

Kelsy Jo Konkright

Bachelor of Science – Geology
University of Alaska Anchorage
2016

A thesis submitted in partial fulfillment
of the requirements for the

Master of Science – Geoscience

Department of Geoscience
College of Science
The Graduate College

University of Nevada, Las Vegas
May 2019

Thesis Approval

The Graduate College
The University of Nevada, Las Vegas

April 4, 2019

This thesis prepared by

Kelsy Jo Konkright

entitled

Petrogenesis of the El Rechuelos Rhyolite, Jemez Mountains Volcanic Field, New Mexico, USA

is approved in partial fulfillment of the requirements for the degree of

Master of Science – Geoscience
Department of Geoscience

Terry Spell, Ph.D.
Examination Committee Chair

Simon Jowitt, Ph.D.
Examination Committee Member

Arya Udry, Ph.D.
Examination Committee Member

Dennis Bazylinski, Ph.D.
Graduate College Faculty Representative

Kathryn Hausbeck Korgan, Ph.D.
Graduate College Dean

ABSTRACT

The El Rechuelos Rhyolite represents volcanic activity preceding the multiple caldera collapse events of the Jemez Mountains volcanic field (JMVF) in northern New Mexico. This study focuses on seven rhyolitic units clustered north of the Valles caldera. These units have been studied in order to interpret their relationships to one another and the eruptive history of the JMVF. Additionally, this study adds to the research on the relationships between effusive and explosive rhyolitic volcanism, and understanding how caldera-forming eruptions develop from silicic systems.

Limited previous research includes K/Ar dates and a few inconsistent ^{40}Ar/^{39}Ar dates, in addition to whole rock geochemistry, petrography, and radiogenic isotope analyses. This previous work has been expanded using comprehensive ^{40}Ar/^{39}Ar geochronology, and more extensive whole rock geochemistry, detailed petrography, and electron microprobe analyses. Five distinct eruptive episodes are characterized by distinctive petrography and geochemistry, which when combined with their ages, suggests that these units are the products of separate, independent magma batches. The Early Rhyolite (7.10 ± 0.04 Ma), is comprised of phenocrysts of plagioclase, quartz, biotite, sanidine, and accessory oxides in a devitrified groundmass. The Intermediate Rhyolite (7.05 ± 0.24 Ma) consists of plagioclase, sanidine, biotite, and minor accessory oxides in a devitrified, altered groundmass. The Pumice Ring Rhyolite (5.61 ± 0.48 Ma) is composed of phenocrysts of plagioclase, biotite, quartz, amphibole, and accessory oxides in a finer crystalline groundmass. The three units comprising the El Rechuelos Rhyolite (2.23 ± 0.15 Ma) appear almost identical to each other petrographically; these units are sparsely porphyritic, comprised primarily of rhyolitic glass and sparse, small crystals of plagioclase, sanidine, biotite, quartz, and accessory oxides. The Young Rhyolite (1.19 ± 0.01 Ma) consists of sanidine, quartz, plagioclase, sparse fayalite, and accessory oxides and zircon in an altered glassy groundmass. All seven of these units plot as rhyolite on the Le Bas Classification Diagram, however there are five distinct suites based on major element comparisons, such as SiO_2 vs. K_2O, Al_2O_3, and CaO. Additionally, trace element geochemical analyses, including Nb vs. Sr, Rb, and Th, indicate five separate magma batches, with only the three 2.23 ± 0.15 Ma units being geochemically related to one another.

Previous studies have disputed the relationships of these units to one another, and which units should be referred to as the El Rechuelos Rhyolite. This study concludes that these seven units represent five separate eruptive episodes, and that only the three 2.23 ± 0.15 Ma units should retain the name of El Rechuelos Rhyolite. Additionally, this study suggests that the Young Rhyolite is a phase of Bandelier Tuff. Geochemical modeling and analysis suggests that the four pre-caldera units are likely products of varying degrees of partial melting and crustal assimilation, while the syn-caldera unit may be a product of fractional crystallization, however more research is needed to fully constrain the petrogenesis of these rhyolites.

ACKNOWLEDGEMENTS

I would like to thank everyone who helped me throughout my time at UNLV. First and foremost, I would like to thank my advisor, Dr. Terry Spell, for his knowledge, support, assistance, and patience throughout this entire project and experience, and for talking me off the ledge a few times. I would like to thank my committee members Dr. Simon Jowitt, Dr. Arya Udry, and Dr. Dennis Bazylinski. I especially would like to thank Kathleen Zanetti for her help in the Nevada Isotope Geochronology Laboratory, Dr. Minghua Ren for his assistance with the electron microprobe, and Dr. Racheal Johnsen for her assistance with my seemingly endless attempts at mineral separation. I would also like to thank Dr. Simon Jowitt for his assistance with geochemical interpretations, willingness to help, great sense of humo(u)r, and general support.

I would like to dedicate this thesis to my family and thank them for their support and encouragement throughout my life. Thank you for introducing me to the outdoors and continuing to feed my curiosity. Thank you to my mother, Nina Hyvonen, for being a great field assistant, and to my entire family for helping me to achieve my goals and for their love and support helping to keep me on track during the many setbacks I faced with this project.

Last, but certainly not least, I would like to thank all of my friends, especially those in the department, for their camaraderie, assistance, and general support, and for helping me to keep my sanity, or at least most of it, throughout the ups and downs of this project.

My time at UNLV was funded by a Teaching Assistantship through the UNLV Department of Geoscience. This thesis project was funded by the Nevada Isotope Geochronology Lab and the Bernada French, Edwards and Olswang Geology, and Graduate Access Funds scholarships. I am incredibly grateful for the opportunities and financial support provided to me by these institutions.

TABLE OF CONTENTS

LIST OF TABLES

LIST OF FIGURES

CHAPTER 1

INTRODUCTION

Large caldera-forming eruptions have occurred throughout Earth’s history (Mason et al., 2004; Self, 2006), resulting in calderas such as the Taum Sauk (Precambrian), La Peligrosa (Jurassic), Yellowstone (Quaternary) and the Valles (Quaternary). Large continental caldera-forming events typically involve silica-rich magmas with high volatile contents (Bachmann and Bergantz, 2008). These large-scale silicic eruptions occur relatively infrequently (Deligne et al., 2010), but can cover large areas in volcanic ash and tephra, potentially causing extensive damage and loss of life. Eruptions such as these can also cause global catastrophic impacts including severe atmospheric and climatic effects (Self, 2006).

Although rhyolitic volcanism has been extensively studied, as both large-scale explosive eruptions and small effusive eruptions of domes and lavas (Cole et al., 2005), the relationships between these types of rhyolitic volcanism are not always well constrained. In some locations, rhyolite domes and flows are found exclusively, but they are also commonly found in association with caldera systems. When found with caldera systems, domes and flows older than the caldera, if preserved, may record the development of the magma system that ultimately led to the caldera-forming event, while effusive eruptions younger than the caldera may represent the remnants of the caldera-forming magma system, or the eruption of new magmas unrelated to the caldera system.

Two major caldera eruptions have occurred in the Jemez Mountains volcanic field, New Mexico, resulting in the Toledo caldera (partially destroyed by subsequent eruptions) and the Valles caldera. This study focuses on the El Rechuelos Rhyolite, a series of six pre-caldera eruptive units, in the Jemez Mountains volcanic field, New Mexico, in addition to a seventh syn-caldera unit. The El Rechuelos Rhyolite records a portion of the eruptive history of the Jemez Mountains volcanic field, preceding these caldera collapse events, while the seventh unit coincides in age with the collapse of the Valles caldera, but the relationship of these units to one another, and to the caldera system is poorly constrained. Thus, this study aims to gain insight into the relationships between these units and the Valles caldera system, in addition to the relationships between the seven individual units.

As these rhyolites have not been extensively studied, the goal of this study is to provide a more complete and comprehensive data set, including more detailed petrography, crystal chemistry, and geochemistry, and updated geochronology utilizing ^{40}Ar/^{39}Ar dating. Interpretations of this data will help to shed light on the relationships of these units to one another, through geochemical modeling and testing of previously proposed hypotheses for generation of these lavas. Additionally, this study will contribute to the investigation of the relationships between effusive and explosive rhyolitic volcanism, and understanding how silicic systems build up to caldera eruptions.

CHAPTER 2

GEOLOGIC SETTING AND PREVIOUS WORK

2.1 The Jemez Mountains Volcanic Field

The Jemez Mountains volcanic field (JMVF) is located in northern New Mexico at the intersection of the Rio Grande rift and the Jemez lineament (Fig. 2.01; Self et al., 1986; Heiken et al., 1990). The intersection of these two zones of crustal weakness has allowed for volcanism at this location (Gardner et al., 1986). The Rio Grande rift is a 15-60 km wide Cenozoic tectonic feature, comprised of a series of north-south trending en echelon sedimentary basins, which bisects New Mexico and southern Colorado (Chapin, 1979; Golombek, 1983, Wolff et al., 2005). Extension of the rift allows for upwelling of the asthenosphere and subsequent volcanism, especially along faults at the margins of the rift. The Jemez lineament is a northeast-trending Paleoproterozoic suture zone that separates the Yavapai terrane to the north from the Mazatzal terrane to the south (Karlstrom et al., 2004). Seismic studies have suggested that the Jemez lineament penetrates the lithosphere and separates low velocity mantle to the north, below the Yavapai terrane, from high velocity mantle to the south, below the Mazatzal terrane. Thus, this interface has been interpreted as the Southern Yavapai-Mazatzal suture (Shaw and Karlstrom, 1999; Magnani et al. 2004). Additionally, the Jemez lineament coincides with an alignment of volcanic centers ranging in age, from ~3 ka (Laughlin et al. 1994) to ~17 Ma, extending from east-central Arizona to southeast Colorado (Goff and Gardner, 2004). It is likely that magmas have taken advantage of the weaknesses associated with the suture zone to reach the surface, allowing for volcanism.

The JMVF, lying on the western edge of the Española Basin, overlies Paleozoic through Cenozoic sedimentary strata and Precambrian basement. Tectonism, encompassing both regional extension and local faulting, has been a partial control of the volcanism in the JMVF, due to extension and upwelling of asthenosphere, and magmas following faults to reach the surface. Episodic Cenozoic regional extension caused rifting beginning at ~30 Ma (Morgan et al., 1986), which then ceased from ~18-13 Ma, resumed from ~13-7 Ma, ceased again at ~7 Ma (Gardner et al., 1986), and resumed again at ~5 Ma with the development of the Pajarito fault zone (Golombek, 1983).

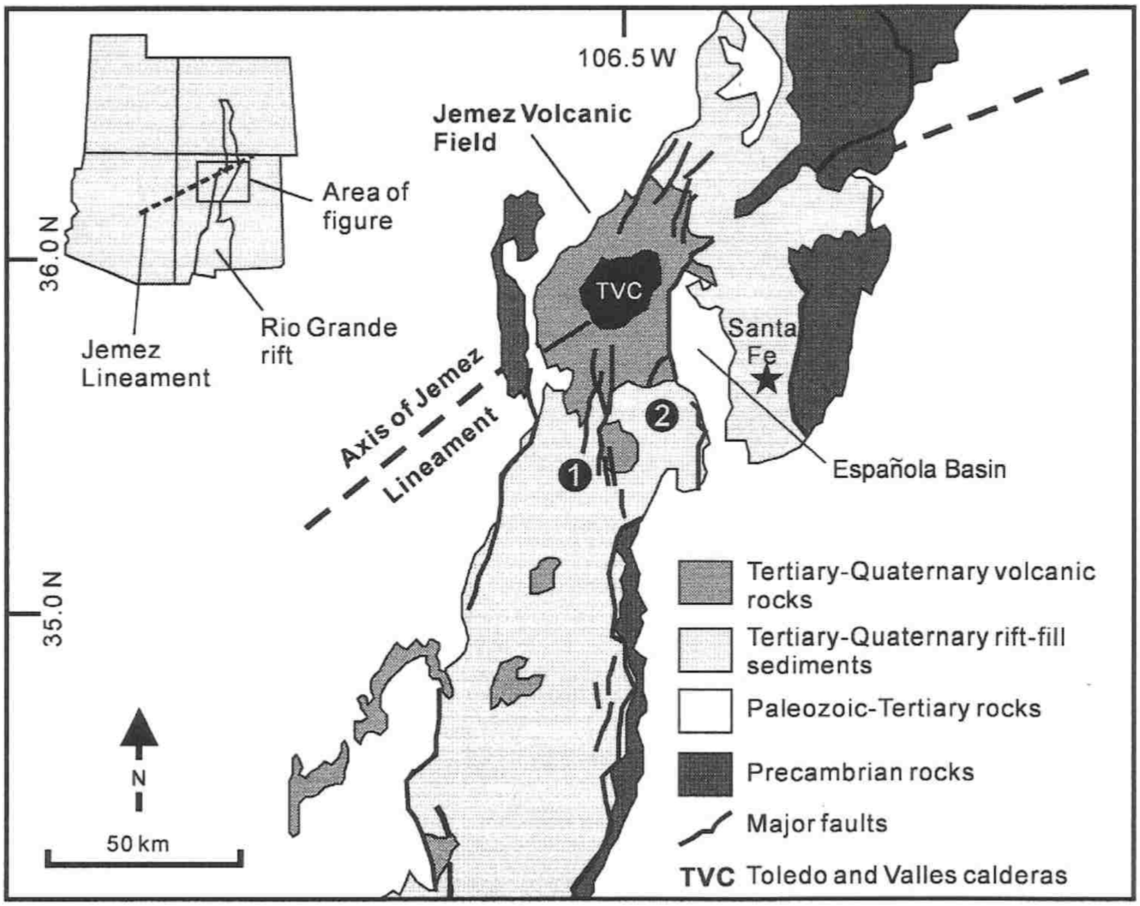

Figure 2.01. Regional map showing relationship between Rio Grande Rift, Jemez Lineament, and Jemez Mountains volcanic field. 1 = Cañada de Cochiti fault zone, 2 = Pajarito fault zone. From Justet (2003), after Self et al. (1986); Gardner and Goff (1984); Baldridge et al. (1983).

In the JMVF, production of voluminous basalts, andesites, dacites, and rhyolites has occurred (Fig. 2.02), dependent upon the varying amounts of evolution of mantle-derived magmas and their interactions with crustal rocks. Volcanism began in the JMVF ~15.3 Ma (Justet, 2003), as recorded by thin alkali basalt flows. These alkaline basalt eruptions were followed by eruptions of basalt, andesite, dacite, and rhyolite, categorized into three groups, first formally described by Bailey et al. (1969); the Keres, Polvadera, and Tewa groups (Fig. 2.03). The Keres Group was erupted from ~13-6 Ma (Gardner and Goff, 1984), and consists of the Paliza Canyon Formation basalt, andesite, and dacite, Canovas Canyon Rhyolite, and the Bearhead Rhyolite (Gardner et al., 1986; Goff et al., 1990; Smith and Lavine, 1996; Justet and Spell, 2001). The Polvadera Group was erupted from ~15-2 Ma (Aldrich, 1986) and is comprised of the Lobato Basalt, Tshichoma Formation andesite and dacite, and El Rechuelos Rhyolite (Loeffler et al., 1988). The Tewa Group eruptions began after ~1.85 Ma (Goff et al., 1986; Heiken et al., 1986; Self et al., 1991; Spell and Harrison 1993; Spell et al., 1996a, 1996b), and include the Lower Bandelier Tuff (LBT), Upper Bandelier Tuff (UBT), and postcollapse Valles Rhyolite.

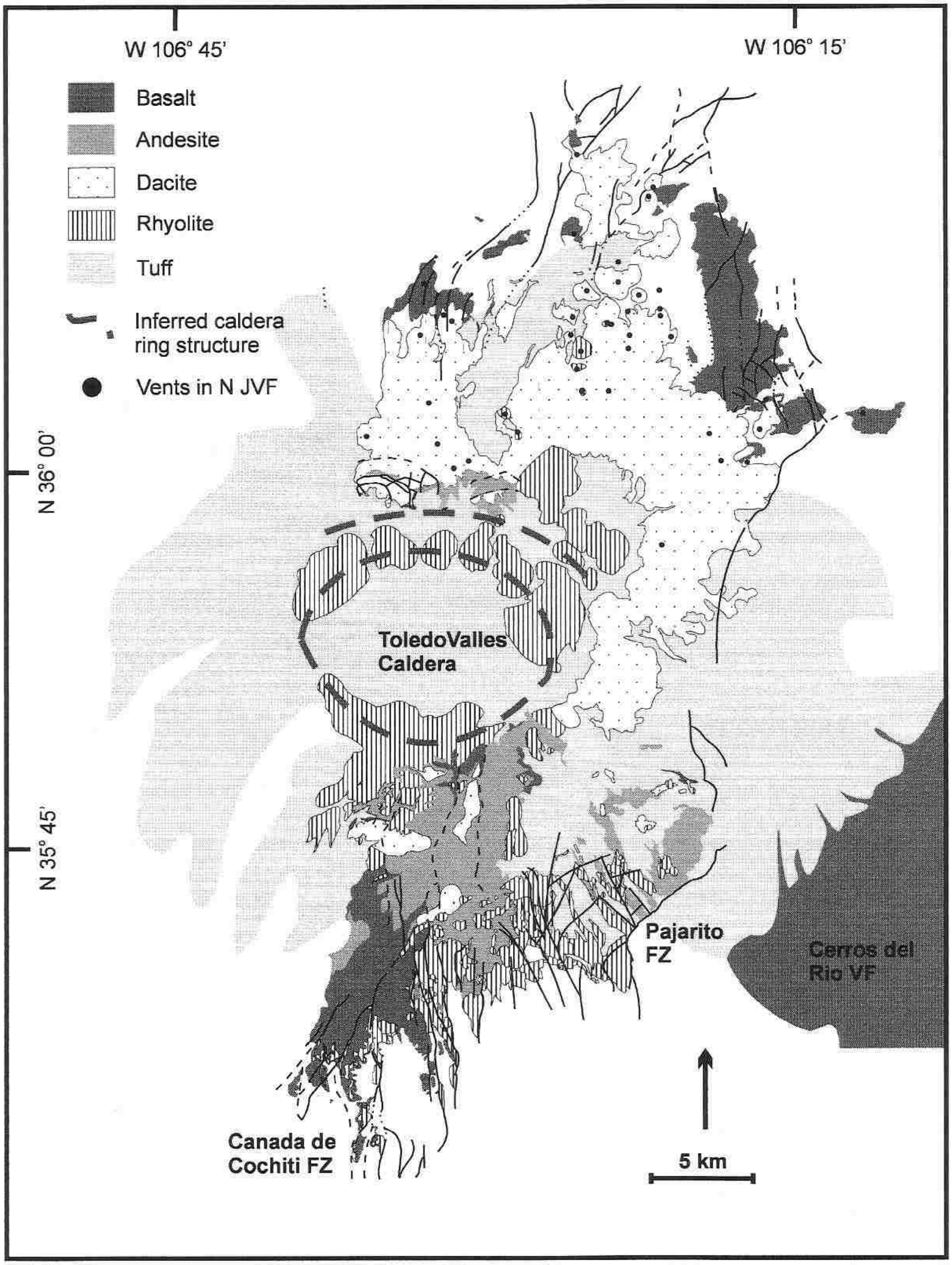

Figure 2.02. Simplified geologic map of the Jemez Mountains volcanic field, NM. From Justet (2003), after Smith et al. (1970).

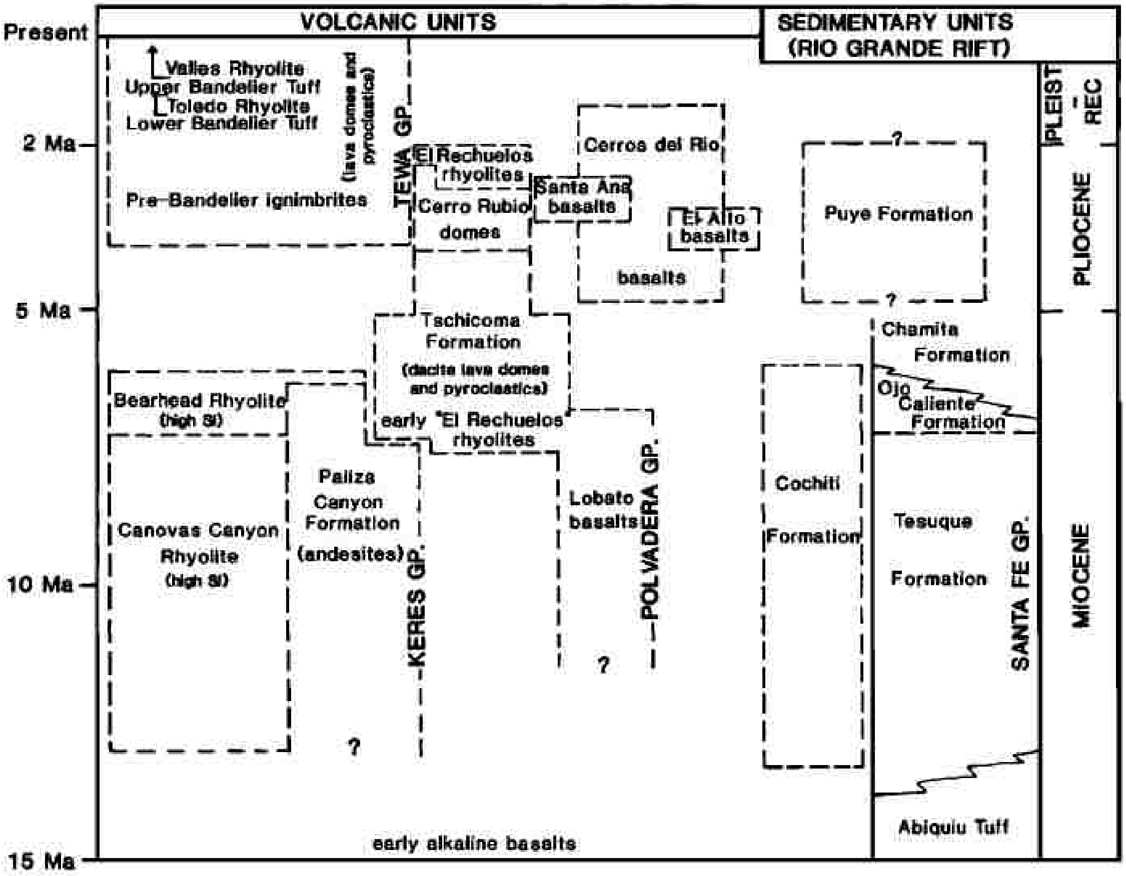

Figure 2.03. Chronostratigraphic chart of major units in the JMVF, using K/Ar ages. From Self et al. (1986).

2.2 The Valles Caldera

The most notable feature of the JMVF is the Valles caldera complex (VCC). First studied in detail in the 1960s (Smith et al., 1961; Smith and Bailey, 1966, 1968; Bailey et al., 1969, Smith et al., 1970), the Valles caldera is now known as the type example of a resurgent dome caldera. By definition, a resurgent dome caldera is classified by uplift of a portion of the caldera floor due to increased pressure within the magma chamber, closely following a caldera-forming eruption. The Valles caldera is a semicircular depression varying in depth from 90 to 650 meters from the caldera floor to the caldera rim, and has a diameter of approximately 19 km measured from east to west and 23 km measured from north to south. Redondo Peak, the resurgent dome within the caldera, is 3,431 meters above sea level, indicating about 1000 meters of local relief. Post-collapse rhyolite domes, flows, and associated pyroclastic rocks have been erupted along ring fractures within the caldera rim. The VCC has undergone two episodes of large-scale ignimbrite eruptions, followed by caldera collapse and resurgence, resulting in the Toledo caldera (embayment) (1.61 Ma), and the younger (1.23 Ma) Valles caldera (Spell et al., 1996b), which largely destroyed the Toledo caldera. Each of these eruptions had a volcanic explosivity index (VEI) of 7 (Newhall and Self, 1982); the Toledo caldera produced ~298 km^3 of ash comprising the Otowi (Lower) Member of the Bandelier Tuff (Cook et al., 2016), while the Valles caldera produced ~400 km^3 of ash comprising the Tshirege (Upper) Member of the Bandelier Tuff (Goff et al., 2014).

Caldera formation generally takes place through several stages (Lipman, 2000), a model which matches the evolution of the VCC. During the first stage, magma buoyantly rises to shallow crustal levels, causing regional tumescence and eruption of small lava domes. The second stage consists of initial vent formation, eruption of large volumes of silicic magma resulting in partial evacuation of the underlying magma chamber, and subsequent caldera collapse, which typically obliterates any evidence of the initial vents. The third stage encompasses resurgence and post-collapse volcanism following renewal of magmatism and replenishment of the magma chamber. Hydrothermal activity and mineralization comprise the fourth stage; although this may be present throughout the caldera formation process, it is typically the dominant activity late in the evolution of the caldera.

2.3 The Polvadera Group

The Polvadera Group erupted from ~15-2 Ma prior to formation of the VCC, is comprised of the Lobato Basalt, Tschicoma Formation andesite and dacite, and the El Rechuelos

Rhyolite- the latter of which is the focus of this study (Fig. 2.04). The majority of the Lobato Basalt, which is tholeiitic in composition, was erupted from ~10.8-7.8 Ma (Manley, 1982; Goff et al., 1989), however mafic lavas in the northern JMVF mapped as Lobato Basalt (Smith et al., 1970; Aldrich and Dethier, 1990), occur interbedded with rift-related Santa Fe Group sediments and have been dated at 14.1 ± 0.3 Ma (Dethier et al., 1986; Aldrich & Dethier, 1990). The Tschicoma Formation is exposed throughout the northern JMVF, from the north to the east of the Valles caldera. This formation is primarily dacite, with lesser amounts of andesite, trachyandesite, and sparse rhyolite, which erupted from ~6.9-2.7 Ma, although the majority of the dacite erupted from ~5.0-2.7 Ma (Dalrymple et al., 1967; Leudke & Smith, 1978; Gardner & Goff, 1984; Goff et al., 1989; Woldegabriel et al., 2001; Goff & Gardner, 2004). The El Rechuelos Rhyolite is comprised of six pre-caldera eruptive units in the northern JMVF, just outside the caldera rim to the north of the VCC, representing four periods of rhyolitic volcanism between ~7.5 and ~2 Ma (Loeffler et al., 1988).

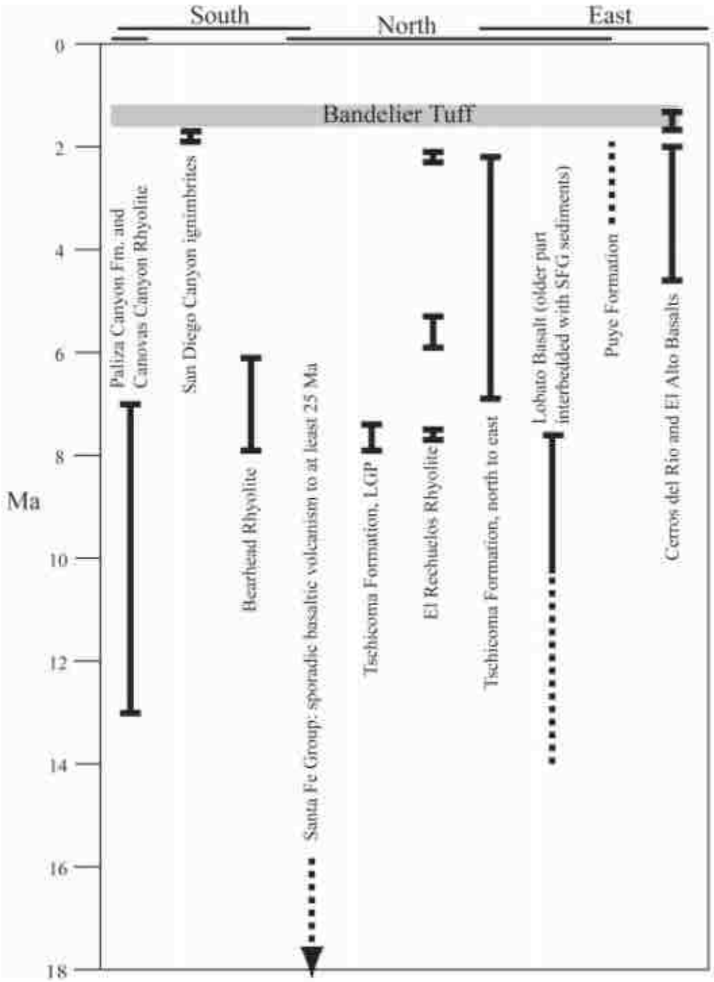

Figure 2.04. Temporal ranges of major JMVF geological units. SFG = Santa Fe Group; LGP = La Grulla Plateau. Dotted lines indicate interbedded volcanic and sedimentary rocks. From Rowe et al. (2007), modified from Goff & Gardner (2004).

2.4 The El Rechuelos Rhyolite

The eruptive units of the El Rechuelos Rhyolite were first studied by Bailey et al. (1969) and have not been a major focus of study since the late 1980s (Loeffler et al., 1988). Bailey et al. (1969) primarily described the location and geomorphology of the units, stating a K/Ar age of ~2.0 Ma on the “largest of the domes,” and that the two units near Canoncito Seco may be older due to their degree of denudation and alteration. Aside from these observations, nothing more was known about these units until Loeffler et al. (1988) began studying the area. More recent work in the JMVF has focused primarily on caldera and post-caldera eruptions, some pre-caldera eruptions, and studies that provide a broad overview of volcanism in the Jemez Mountains (Balsley, 1988; Justet, 2003; Wolff et al., 2005; Rowe et al., 2007; Eichler, 2012).

The El Rechuelos Rhyolite consists of six rhyolitic units, north of the Valles caldera, in the northern JMVF (Fig. 2.05; Bailey et al., 1969; Smith et al., 1970). At least three episodes of rhyolitic volcanism are represented by these six units, based on time spans between previously published ages (Fig. 2.06). Four units have been dated using K/Ar geochronology; one dome at 7.5 Ma, one dome at 5.8 Ma, and two domes at 2.0 Ma (Dalrymple et al., 1967; Loeffler et al., 1988). The fifth unit has been ^{40}Ar/^{39}Ar dated at 2.0 Ma (Kelley et al., 2013), and is the southernmost of three domes erupted along a fracture system striking north-south to the west of Polvadera Peak. The age of this southern dome is in agreement with the K/Ar ages obtained for the other two domes along the fracture system. The remaining sixth unit is a 5.2 Ma rhyodacite pumice ring, originally classified as El Rechuelos Rhyolite by Smith, Bailey, and Ross (1970) based on K/Ar dating, and has since been suggested to be part of the Tschicoma Formation (Loeffler et al., 1988). Loeffler et al. (1988), the only previous study focusing specifically on the El Rechuelos Rhyolite, reported K/Ar geochronology, whole rock major- and trace-element analyses, Sr and Nd isotopic ratios, and petrographic data, and discussed the geochemical and petrogenetic relationships of the six units.

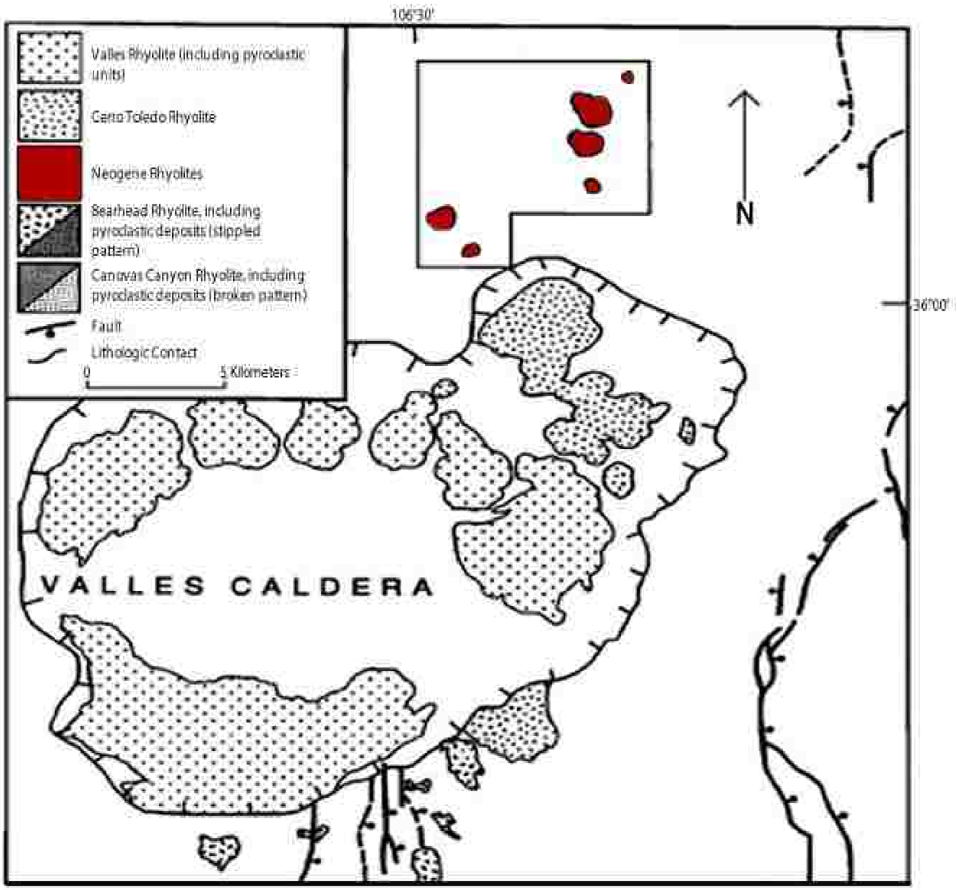

Figure 2.05. Geologic map showing the locations of the El Rechuelos Rhyolite eruptive units, in red, in relation to the Valles caldera. Outlined area shown in greater detail in Fig. 2.06. Modified from Loeffler et al. (1988).

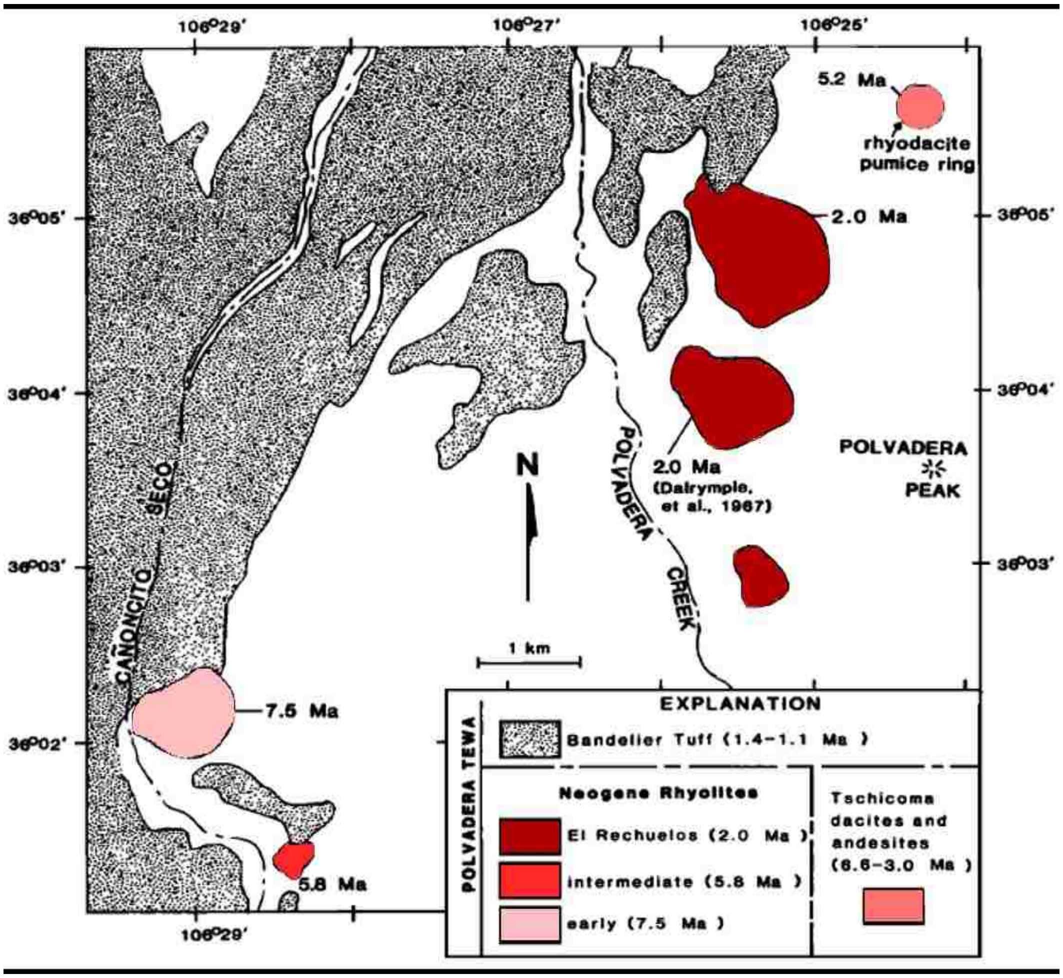

Figure 2.06. Geologic map of the northern Jemez Mountains volcanic field and the locations of the El Rechuelos Rhyolite eruptive units. Modified from Loeffler et al. (1988).

Petrographic observations suggest that the three eruptive episodes, and the pumice ring, are distinct from one another due to differences in crystal size, composition, abundance, and mineral assemblage (Loeffler et al., 1988). The oldest unit (7.5 Ma) was described as a flow-banded biotite rhyolite, and is the larger of the two domes located near Cañoncito Seco (Fig. 2.06; Loeffler et al., 1988). The smaller of these two domes is the intermediate unit (5.8 Ma) which is partially covered by Bandelier tuff, and contains microphenocrysts of anorthoclase-sanidine-quartz myrmekitic intergrowths, devitrified groundmass, and is also strongly flow-banded (Loeffler et al., 1988). The three young units (2 Ma), trending N-S along Polvadera

Creek, are described as nearly aphyric, pumiceous rhyolite and obsidian (Fig. 2.06; Loeffler et al., 1988). The Pumice Ring (5.2 Ma), ~4 km to the north of Polvadera Peak, was not investigated in as much detail, but was described as having ample disequilibrium textures and is distinct from the other units in that it contains amphibole (Loeffler et al., 1988).

Variable Nd isotopic ratios rule out a single magma batch evolving by fractional crystallization and assimilation to produce the six eruptive units, and combined Sr and Nd isotopic ratios rule out direct anatexis of Precambrian crust (Loeffler et al., 1988). Instead, the differing Sr and Nd isotopic ratios are interpreted to represent at least three eruptive episodes (7.5 Ma, 5.8 Ma, and 2.0 Ma) generated by fractional crystallization and lower crustal assimilation of three distinct mantle-derived magmas (Loeffler et al., 1988). Negative εNd values for the Early Rhyolite (εNd = -3.6) and the central dome of the El Rechuelos Rhyolite (εNd = -1.2) suggest derivation from an enriched lithospheric mantle (Loeffler et al., 1988; Liu et al., 2014). Additionally, due to the large span between eruptive ages (7.5-2.0 Ma) of the rhyolites, it is suggested that they did not originate from the same parent magma (Loeffler et al., 1988), although this does not preclude these rhyolites being derived from the same source and having the same magmatic differentiation history.

CHAPTER 3

METHODS

3.1 Sample Collection

Field work and sample collection for this study took place in July 2017 and May 2018. Eruptive units were sampled based on the geologic map of the Jemez Mountains by Smith, Bailey, and Ross (1970), locations and descriptions of Loeffler et al. (1988), the Preliminary Geologic Map of the Polvadera Peak 7.5 Minute Quadrangle by Kempter et al. (2004), and the USGS topographic and orthophoto maps of the Polvadera Peak 7.5 Minute Quadrangle. Twenty-seven samples were collected for additional preparation and analysis, from each of the six units originally mapped as El Rechuelos Rhyolite, plus an additional seventh unit sampled during field work (Appendix A). Samples were collected to obtain unweathered samples with the least alteration possible. Collected samples were examined and selected for further processing and analysis, based on their representative nature and phenocryst populations. Nineteen of the samples were selected for major- and trace-element geochemistry, seven for $^{40}Ar/^{39}Ar$ geochronology, 13 for petrography, and seven for electron microprobe imaging and analysis. All other samples were retained for potential future use.

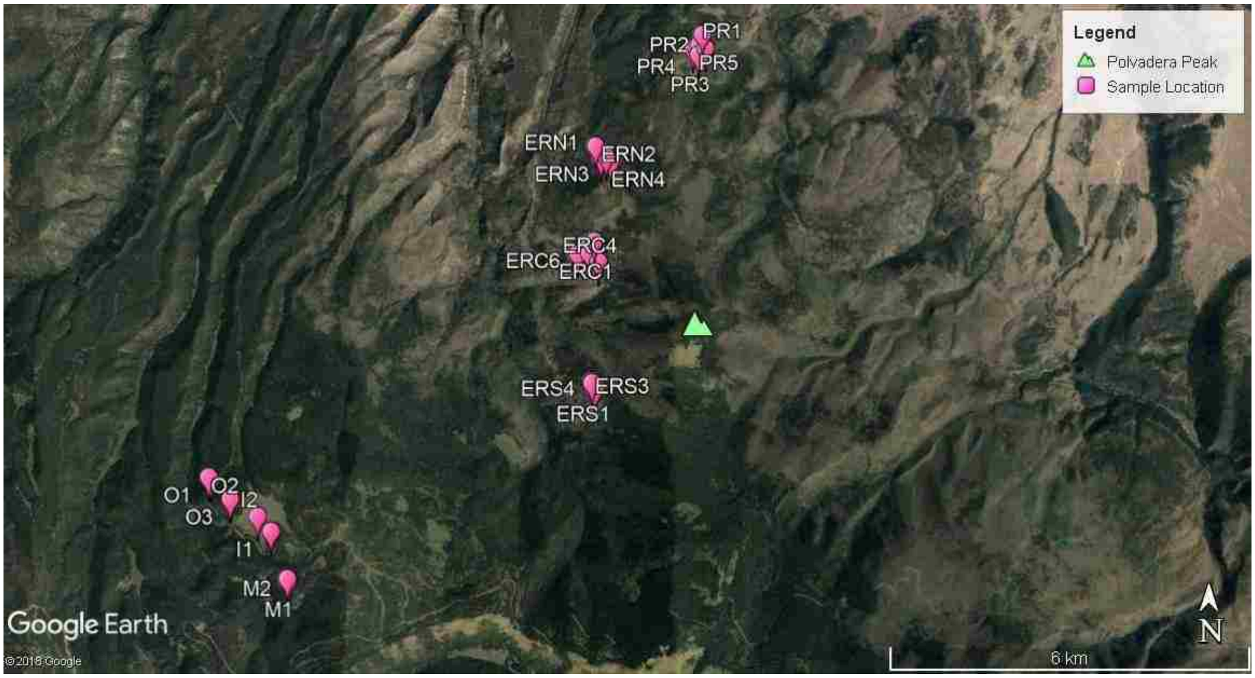

Figure 3.01. Sample locations for this study. Green mountain symbol denotes Polvadera Peak. Image modified from Google Earth.

Figure 3.02. Sample locations for the southwestern portion of field area. Large treeless area is Cienega Redonda. Santa Fe National Forest Road 27 cuts across the figure. Image modified from Google Earth.

Figure 3.03. Sample locations for the northeastern portion of field area. Image modified from Google Earth.

Figure 3.04. Sample locations for the central portion of field area. Green mountain symbol denotes Polvadera Peak. Image modified from Google Earth.

3.2 Sample Preparation

Representative hand samples were cut using a Hillquist rock saw to standard billet dimensions (~22 x 44 mm) for thin section and polished probe section preparation. Billets were sent to Wagner Petrographic where thirteen standard thin sections and seven polished probe sections were prepared for use. The remaining hand samples were set aside for future use.

3.3 Geochemistry

Hand samples with the least weathering and alteration were selected to be prepared for geochemical analysis. Nineteen whole rock hand samples, at least 50 grams each, were selected and sent to the Peter Hooper GeoAnalytical lab at Washington State University (WSU). At WSU, they were powdered, further processed, and analyzed for major and trace elements utilizing X-Ray Fluorescence (XRF) and Inductively Coupled Plasma Mass Spectrometry (ICP-MS) techniques, following the methods described by Johnson et al. (1999) and Knaack et al. (1994), respectively. Calibration of instruments utilizing known standards, to maintain accuracy, is detailed by Johnson et al. (1999) and Knaack et al. (1994). Loss on ignition (LOI) calculations were also completed at WSU, as part of the XRF and ICP-MS analyses. LOI calculations measure the amount of water and volatiles present in each sample, in order to estimate the reliability of mobile elements. Additionally, duplicate samples from this study were run to assess precision of the analyses (Appendices C and D).

3.4 Petrography

Petrographic observations consisted of both hand sample and thin section examination of each eruptive unit. Preliminary observations of crystal assemblages and relative abundances of phenocrysts were done using hand samples. Thin section examination provided more detailed identification of major and accessory mineral phases, in addition to crystal characteristics and petrologic textures. Photomicrographs were produced to record any distinct textures or crystal characteristics present in each section. Modal abundances were determined by point counts of a representative thin section; 600 points were counted on each thin section in order to calculate abundances.

3.5 $^{40}Ar/^{39}Ar$ Geochronology

A portion of remaining sample from each of the seven collected units was processed using a Bico Chipmunk rock crusher and a Bico disk mill to obtain grain sizes suitable for sieving. This material was then sieved through 2000 µm to 50 µm sieve size fractions to obtain suitable size fractions for mineral separation. Some of the samples contained phenocrysts large enough to hand pick using a binocular microscope, while others required more detailed mineral separation techniques, such as density separation and magnetic separation, due to small phenocryst sizes. Four samples required density separations using bromoform, while one required an additional separation, using methylene iodide. Additionally, these samples required the use of a Frantz magnetic separator in order to obtain enough of the desired mineral(s) for $^{40}Ar/^{39}Ar$ geochronology step heating runs. Samples chosen for $^{40}Ar/^{39}Ar$ geochronology are: JM-17-O2-KK, JM-17-I2-KK, JM-17-PR6-KK, JM-17-ERN3-KK, JM-17-ERC5-KK, JM-17-ERS2-KK, and JM-18-M2-KK.

Once the necessary amount of mineral separate from each sample was obtained, the mineral samples were packed and sent to the United States Geological Survey (USGS) TRIGA Reactor in Denver, Colorado for irradiation. The fluence monitor used was Fish Canyon Tuff sanidine (FC-2), with an age of 28.02 ± 0.16 Ma (Renne et al., 1998). Samples were wrapped in aluminum foil and stacked in 6 mm inner-diameter sealed fused silica tubes. Each sample package averaged ~2mm thick, and fluence monitors were placed every 5-10 mm along the tube.

Additionally, synthetic K-glass and optical grade CaF were included in the silica tubes to track neutron induced argon isotope interferences from K and Ca. The packed sample tube was placed in a Cd Lined In-Core Irradiation Tube and irradiated in-core for four hours in the 1 MW TRIGA reactor.

After irradiation, each sample was then analyzed in the Nevada Isotope Geochronology Lab (NIGL) at the University of Nevada Las Vegas. FC-2 standards were placed in a copper sample tray in a high vacuum extraction line, and fused using a 20 W CO_2 laser. All samples were analyzed by the furnace step heating method, utilizing a double vacuum resistance furnace, similar to the Staudacher et al. (1978) design. One sample was analyzed using the laser fusion method, however the majority of the crystals were discovered to be plagioclase, which significantly reduced the yield of $^{40}Ar^*$ (radiogenic ^{40}Ar, produced from radioactive decay of ^{40}K), requiring the backup sample to be analyzed via furnace heating for more accurate results. During furnace step heating, reactive gasses are captured by three GP-50 SAES getters, leaving purified argon which is then transferred to a MAP 215-50 mass spectrometer by expansion. The relative volumes of the extraction line and mass spectrometer allow 80% of the gas to be admitted to the mass spectrometer for laser fusion analyses and 76% for furnace heating analyses. Peak intensities were measured using a Balzers electron multiplier taking measurements through seven cycles; initial peak heights of ^{36}Ar, ^{37}Ar, ^{38}Ar, ^{39}Ar, and ^{40}Ar were determined by linear regression of the seven cycles to the time of gas admission to the mass spectrometer.

Mass spectrometer discrimination and sensitivity were monitored by analyzing atmospheric argon and blanks. Measured $^{40}Ar/^{36}Ar$ ratios averaged 388.41 ± 0.02% during this work, thus a discrimination correction of 0.7608 (4 AMU) was applied to measured isotope ratios. The sensitivity of the mass spectrometer was ~6 x 10^{-17} mol mV^{-1} with the multiplier operated at a gain of 36 over the Faraday. Line blanks averaged 2.88 mV for mass 40 and 0.01 mV for mass 36 for laser fusion analyses and 12.41 mV for mass 40 and 0.03 mV for mass 36 for furnace heating analyses. Discrimination, sensitivity, and blanks were relatively constant over the period of data collection.

Computer automated operation of the sample stage, CO_2 laser, extraction line and mass spectrometer, in addition to final data reduction and age calculations, were done using LabSPEC software, version 3.1c (Idleman, 2000). Isochron regression and weighted mean plots were completed using Isoplot software, and Matlab curve fit was used to determine J and uncertainty in J at each standard position.

For $^{40}Ar/^{39}Ar$ analyses, a plateau segment consists of 3 or more contiguous gas fractions that have analytically indistinguishable ages, meaning that all plateau steps overlap in age at $\pm 2\sigma$ analytical error, and comprise a significant portion of the total gas released (>50%). Total gas (integrated) ages are calculated by weighting by the amount of ^{39}Ar released, whereas plateau ages are weighted by the inverse of the variance. Inverse isochron diagrams are examined for each sample to check for the effects of excess argon. Reliable isochrons are based on the MSWD criteria of Wendt and Carl (1991) and, as for plateaus, must comprise contiguous steps and a significant fraction of the total gas released. All analytical data are reported at the confidence level of 1σ (standard deviation).

3.6 Electron Microprobe

Prior to microprobe analysis, photomosaics were produced for each polished thin section, to map out the thin section and determine phenocrysts to be analyzed on the JEOL JXA-8900 probe at the UNLV Electron Microanalysis and Imaging Laboratory (EMIL). Thin sections were cleaned with deionized water and placed in a vacuum desiccator to remove remaining moisture. Following desiccation, samples were carbon coated for electron microprobe work. Carbon coating was done by placing samples in a Denton Vacuum DV-502A evaporator, evacuated to approximately 10^{-5} millitorr, in which an electric current was passed through an ultra-pure carbon rod to deposit a carbon coating approximately 20 µm thick on the surface of the thin section.

Three polished thin sections (JM-17-ERN3-KK, JM-17-ERC5-KK, and JM-17-ERS2-KK) lacked a suitable number of phenocrysts, requiring grain mounts to be made of those samples. Mineral separates leftover from ^{40}Ar/^{39}Ar geochronology separations were epoxy mounted in 1-inch rounds, then polished using a Buehler Ecomet 6 Grinder-Polisher, using a series of 16, 13, and 9 µm polishing discs, followed by hand polishing with 1 µm silicon diamond solution on an 8” Buehler Texmet polishing cloth affixed to a glass plate. These samples were then cleaned and coated using the previously stated methods.

Once carbon coated, thin sections or grain mounts were loaded into the probe and electron dispersive spectroscopy (EDS) was performed on selected phenocrysts to identify elements present to verify mineral phases, before analyzing with the probe. Back scatter electron (BSE) images were then produced for each of the target areas, to identify textural changes and chemical zonation in each crystal of interest. BSE images are produced by bombarding a targeted area with electrons, using a scanning beam of focused electrons, which subsequently releases scattered electrons from the surface of the sample. These rebounded electrons are detected and recorded as a digital signal by the BSE detectors. The number of back scattered electrons detected is proportional to the mean atomic number (Z) of the targeted area or sample, meaning that areas that appear brighter correspond with greater average Z, while darker areas correspond with lower average Z. This makes BSE images very useful in determining different phases and/or compositional differences within a phase.

Using the BSE images as a guide, rim to rim and core to rim traverses were plotted in order to document any zonation present, in addition to spot analyses. Electron microprobe analyses were performed under operating conditions of 15 kV accelerating voltage, 10 nA beam current, and 10 μm beam size. Targeted phases included feldspar crystals, mafic minerals, and oxide minerals. Feldspars were analyzed for the following elements: Si, Mg, K, Ti, Na, P, Ca, Fe, Al, Mn, and Ba. Mafic and oxide minerals were analyzed for the following elements: Si, Mg, K, Ti, Na, P, Ca, Fe, Al, Mn and Ba, in addition to F, S, Cl, Cr, and Nb for some samples.

After BSE images were produced, and traverses and spot analyses were planned, mineral standards were run before analysis of the samples, to ensure proper calibration. Standards used at EMIL were as follows: Cr-Augt164905, Microcln143966, Ilmenite96189, SM-Albite, Plag-115900, SM-Apatite, CM2-agcl, MAC-fluorite, MAC-pyrite, Chromite117075, CM2-baf2, Gel-Nb, SM-Cr-Augite, Anothcls133868, Gel-Hf, REE-cepo4, REE-lapo4, MAC-zircon, F-Ap104021, and SM-Ilmenite. After completion of these steps, predetermined traverses and set points were analyzed for chemical compositions.

CHAPTER 4

RESULTS

4.1 Petrography

4.1.1 Petrography of the Early Rhyolite

Early Rhyolite samples (JM-17-O1-KK and JM-17-O2-KK; Fig. 3.02) are coarsely porphyritic (~37% crystals; Table 4.01) with crystals in a devitrified groundmass. Primary minerals include, in order of decreasing abundance, plagioclase, quartz, biotite, and sanidine with accessory oxides and microphenocrysts of the same minerals. Cumulophyric clusters are visible throughout this unit, especially those incorporating plagioclase and biotite.

Plagioclase crystals within the Early Rhyolite samples are subhedral to euhedral and range in size from ~0.1 to 3.0 mm. Albite and carlsbad twinning is common in the plagioclase, in addition to concentric, oscillatory zonation (Fig. 4.01). Plagioclase crystals in this unit also less commonly display reaction rims, sieve texture, and inclusions of oxides and zircon (Fig. 4.01).

Quartz crystals are anhedral and range in size from ~0.1 to 1.3 mm. Biotite crystals are subhedral to euhedral and range in size from ~0.2 to 1.1 mm. Embayment, intergrowth, and oxide inclusions are also present in some of the biotite crystals (Fig. 4.01). Sparse sanidine crystals are subhedral to euhedral and range from ~0.1 to 1.0 mm.

Figure 4.01. Left, JM-17-O1-KK, zoned plagioclase displaying sieve texture and reaction rim. Center, JM-17-O2-KK, plagioclase displaying sieve texture with intergrown biotite. Right, JM-17-O2-KK, embayed biotite. Images taken in cross-polarized light (XPL).

4.1.2 Petrography of the Intermediate Rhyolite

The Intermediate Rhyolite (JM-18-M2-KK; Fig. 3.02) is sparsely porphyritic (~4% crystals, Table 4.01) with a devitrified, flow banded groundmass. Groundmass has undergone extensive alteration to clay (Fig. 4.02). Major mineral phases include plagioclase, sanidine, and biotite, with minor accessory oxides.

Plagioclase is the dominant feldspar in the Intermediate Rhyolite; crystals range from ~0.2 to 2.0 mm in size and are anhedral to subhedral. Plagioclase crystals display albite and carlsbad twinning, alteration to clay minerals, and uncommonly, zonation (Fig. 4.02).

Sanidine and biotite are sparse in the Intermediate Rhyolite and do not display any distinguishing characteristics. Sanidine crystals range from ~0.2 to 0.3 mm in size and are subhedral to euhedral. Biotite crystals range from <0.1 to 0.8 mm in size and are anhedral to subhedral.

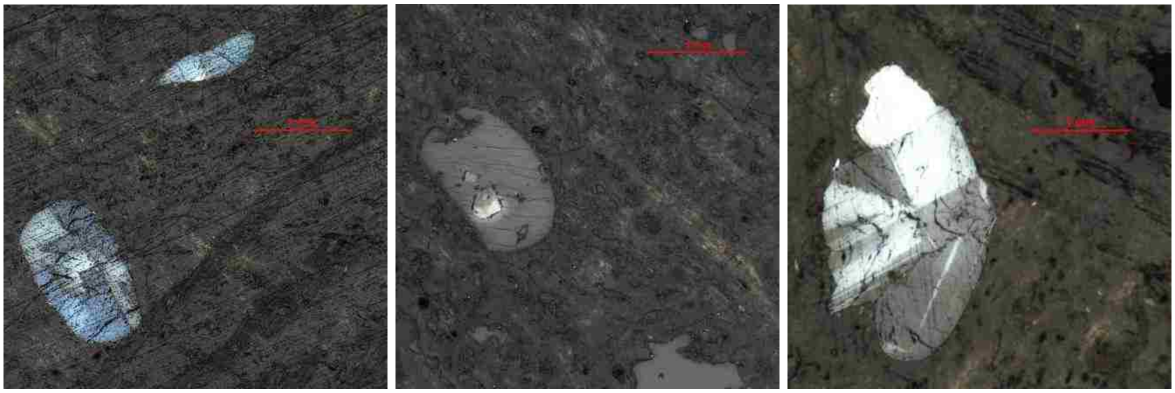

Figure 4.02. Left, JM-18-M2-KK, plagioclase in altered groundmass. Center, JM-18-M2-KK, sanidine in altered groundmass. Right, JM-18-M2-KK, plagioclase in altered groundmass. Images taken in XPL.

4.1.3 Petrography of the Pumice Ring Rhyolite

Pumice Ring Rhyolite samples (JM-17-PR3-KK and JM-17-PR6-KK; Fig. 3.03) are porphyritic (~21% crystals; Table 4.01) with larger crystals set in a finer crystalline groundmass. Primary minerals include plagioclase, biotite, quartz, amphibole, and accessory oxides. The groundmass is weathered and altered, with visible sericite throughout.

Plagioclase crystals are anhedral to euhedral and range in size from <0.1 to 1.3 mm. Albite and carlsbad twinning are prevalent, as is concentric, oscillatory zonation (Fig. 4.03). Dissolution features, such as resorption, reaction rims, and sieve texture are also displayed in plagioclase, but are less common.

Biotite crystals are subhedral to euhedral and range from <0.1 to 1.1 mm in size. Oxide inclusions are common in biotite, and sparse resorption textures are also displayed. Biotite is present as individual phenocrysts, but in some instances form as glomerocrysts with amphibole and oxides. Amphiboles are subhedral to euhedral, range in size from <0.1 to 1.1 mm, and display some oxide inclusions. Amphibole is more abundant in JM-17-PR6-KK. Quartz crystals range in size from ~0.2 to 1.0 mm and are anhedral to subhedral. Dissolution features are fairly common, including resorption and reaction rims (Fig. 4.03).

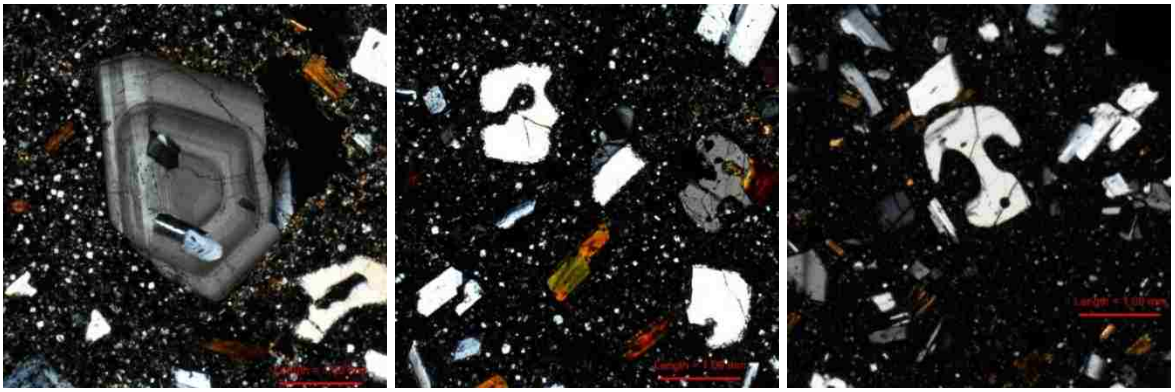

Figure 4.03. Left, JM-17-PR3-KK, zoned plagioclase and embayed quartz. Center, JM-17-PR3-KK, embayed quartz with reaction rim, biotite, amphibole, and groundmass. Right, JM-17-PR6-KK, embayed quartz. Images taken in XPL.

4.1.4 Petrography of the El Rechuelos Rhyolite

For the purposes of this study, the El Rechuelos Rhyolite domes have been subdivided, North to South, as follows; ERN, ERC, and ERS. Petrographically, the three El Rechuelos Rhyolite domes are very similar. In general, the El Rechuelos Rhyolite is sparsely porphyritic (~2-4% crystals; Table 4.01) with a vitrophyric groundmass. The unit is comprised primarily of rhyolitic glass and sparse, small crystals of plagioclase, sanidine, biotite, quartz, and oxides.

Northern Dome

The northern El Rechuelos dome (Fig. 3.03) is sparsely porphyritic, containing ~4% crystals (Table 4.01). Samples from the northern dome (JM-17-ERN1-KK and JM-17-ERN3-KK) are very similar, however ERN1 displays a more pumiceous groundmass and contains more vesicles, while ERN3 contains less vesicles and more microlites of plagioclase that are also slightly larger. The most abundant mineral in these samples is plagioclase, present as both phenocrysts and microlites. Plagioclase is subhedral to euhedral and ranges in size from <0.1 to 2 mm. Albite and carlsbad twinning are common (Fig. 4.04). Plagioclase displaying sieve texture are present, although sparse.

Sanidine crystals range in size from <0.1 to 2 mm, are anhedral to subhedral, and uncommonly display resorption textures. Biotite crystals are primarily <0.1 mm but can range up to ~0.2 mm in size and are subhedral to euhedral. Quartz crystals are also primarily <0.1 mm but can range up to ~1.2 mm in size, are anhedral, and some are resorbed. Spherulites are also present throughout these samples, ranging in size from <0.1 to 0.8 mm.

Central Dome

The central El Rechuelos dome (Fig. 3.04) is very sparsely porphyritic, with only ~2% crystals (Table 4.01) set in a glassy, vesicular groundmass. Plagioclase and sanidine occur in comparable abundance in these samples (JM-17-ERC5-KK and JM-17-ERC6-KK). These samples contain small phenocrysts (~0.1-0.5 mm) of plagioclase and sanidine, in addition to microlites of plagioclase, sanidine, and biotite, all less than ~0.1 mm in size (Fig. 4.04). Spherulites are also present in the samples from the central dome, although less abundant than in samples from the northern dome. Spherulites measure <0.1 to 0.5 mm in size. ERC5 and ERC6 are very similar, although ERC6 displays perlitic texture, elongated rather than rounded vesicles, and more weathering and alteration to clay which is not commonly seen in other samples of the El Rechuelos Rhyolite.

Southern Dome

The southern El Rechuelos dome (Fig. 3.04) is also very sparsely porphyritic with ~2% crystals (Table 4.01) in a glassy groundmass. Plagioclase is the major phase in these samples (JM-17-ERS2-KK and JM-17-ERS4-KK). These samples contain small phenocrysts (~0.1-0.5

mm) of plagioclase, in addition to microlites of plagioclase and biotite, less than ~0.1 mm in size (Fig. 4.04). Spherulites are also present in this unit, ranging in size from <0.1 to 0.7 mm. ERS2 and ERS4 are generally similar, although ERS2 contains vesicles while ERS4 does not, and ERS4 contains more microlites and spherulites than ERS2.

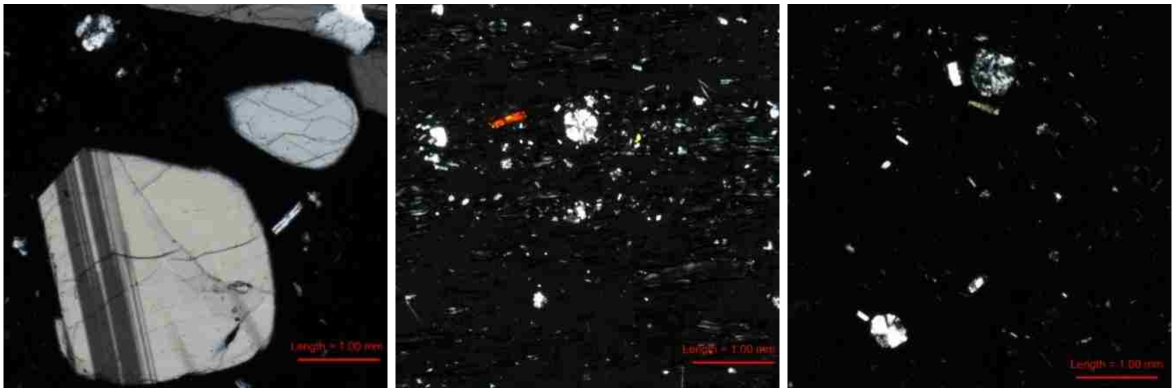

Figure 4.04. Left, JM-17-ERN3-KK, plagioclase, quartz, and spherulites in glassy groundmass. Center, JM-17-ERC5-KK, spherulites and microlites of plagioclase, sanidine, and biotite in glassy groundmass. Right, JM-17-ERS2-KK, spherulites and microlites of plagioclase and biotite in glassy groundmass. Images taken in XPL.

4.1.5 Petrography of the Young Rhyolite

Young Rhyolite samples (Fig. 3.02) are porphyritic (~27% crystals, Table 4.01) with large crystals in an altered glassy groundmass. Primary minerals in these samples (JM-17-I1-KK and JM-17-I2-KK) include sanidine, quartz, plagioclase, and accessory oxides and zircon.

Sanidine is the dominant feldspar in these samples. Sanidine crystals are anhedral-euhedral and range in size from <0.1 to 2.0 mm. Quartz crystals are anhedral and range in size from ~0.2 mm to 3.0 mm. Some quartz crystals are embayed (Fig. 4.05). Plagioclase crystals range in size from <0.1 to 3.0 mm and are anhedral. Plagioclase in this unit displays carlsbad and albite twinning. Sample I2 additionally contains sparse fayalite crystals measuring ~0.6 to 1.0 mm in size (Fig. 4.05).

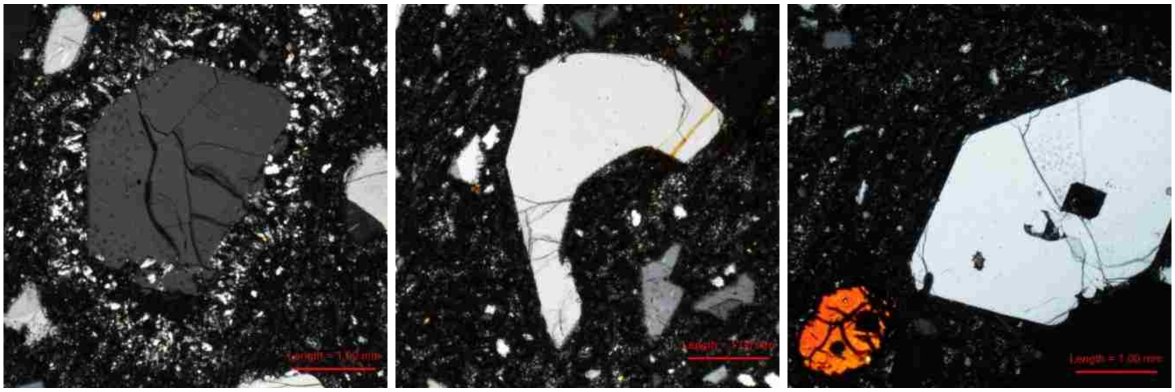

Figure 4.05. Left, JM-17-I1-KK, quartz with devitrified groundmass. Center, JM-17-I1-KK, embayed quartz. Right, JM-17-I2-KK, fayalite and quartz surrounded by groundmass. Images taken in XPL.

Table 4.01. Modal abundances of crystals and groundmass based on point count results.

Sample Name:	JM-7/4/17-O1-KK	JM-5/21/18-M2-KK	JM-7/27/17-PR3-KK	JM-7/5/17-ERN1-KK	JM-7/29/17-ERC5-KK	JM-7/28/17-ERS2-KK	JM-7/4/17-I1-KK
Unit	Early Rhyolite	Intermediate Rhyolite	Pumice Ring Rhyolite	El Rechuelos Rhyolite North	El Rechuelos Rhyolite Central	El Rechuelos Rhyolite South	Young Rhyolite
Point Count Results							
Quartz	13	0	6	1	0	0	54
Plagioclase	155	16	92	10	2	8	6
Sanidine	4	2	0	2	2	0	91
Biotite	10	1	18	2	1	1	0
Amphibole	0	0	2	0	0	0	0
Oxides	9	6	6	3	0	0	5
Microphenocrysts	28	0	0	6	5	4	4
Vesicles	14	41	30	155	99	123	6
Groundmass	367	534	446	421	491	464	434
Total	600	600	600	600	600	600	600
Modal Abundance of Crystals							
Quartz	5.9	0.0	4.8	4.2	0.0	0.0	33.8
Plagioclase	70.8	64.0	74.2	41.7	20.0	61.5	3.8
Sanidine	1.8	8.0	0.0	8.3	20.0	0.0	56.9
Biotite	4.6	4.0	14.5	8.3	10.0	7.7	0.0
Amphibole	0.0	0.0	1.6	0.0	0.0	0.0	0.0
Oxides	4.1	24.0	4.8	12.5	0.0	0.0	3.1
Microphenocrysts	12.8	0.0	0.0	25.0	50.0	30.8	2.5
Modal Abundance of Groundmass							
Vesicles	3.7	7.1	6.3	26.9	16.8	21.0	1.4
Groundmass	96.3	92.9	93.7	73.1	83.2	79.0	98.6
Percent Crystals	36.5	4.2	20.7	4.0	1.7	2.2	26.7
Percent Groundmass	63.5	95.8	79.3	96.0	98.3	97.8	73.3

4.2 ^{40}Ar/^{39}Ar Geochronology

Geochronology results are presented here, from the oldest to youngest eruptive unit. All data can be found in Appendix B. Ages are summarized in table 4.02. Uncertainties are quoted at one sigma. Preferred ages are calculated by taking the mean and standard deviation of selected portions of the step heating runs, with inconsistent/outlier steps rejected. Rejections are made based on evidence of low radiogenic yields, unusual Ca/K ratios, and/or anomalous step ages that are inconsistent with the majority of steps.

Table 4.02. Summarized ^{40}Ar/^{39}Ar data.

Sample Name	Unit	Phase Dated	Age
JM-7/4/17-O2-KK	Early Rhyolite	Plagioclase Biotite	7.51 ± 0.26 Ma 8.05 ± 0.18 Ma
JM-5/21/18-M2-KK	Intermediate Rhyolite	Plagioclase	7.05 ± 0.24 Ma
JM-7/27/17-PR6-KK	Pumice Ring Rhyolite	Biotite Amphibole	5.61 ± 0.48 Ma 4.31 ± 2.31 Ma
JM-7/5/17-ERN3-KK	El Rechuelos Rhyolite North	Plagioclase	2.23 ± 0.15 Ma
JM-7/29/17-ERC5-KK	El Rechuelos Rhyolite Central	Feldspar + Glass	1.78 ± 0.07 Ma *
JM-7/28/17-ERS2-KK	El Rechuelos Rhyolite South	Feldspar + Glass	2.97 ± 0.06 Ma *
JM-7/4/17-I2-KK	Young Rhyolite	Anorthoclase	1.19 ± 0.01 Ma

* denotes unreliable age

4.2.1 Early Rhyolite

Plagioclase

JM-17-O2-KK plagioclase produced a moderately discordant 10 step age spectrum with a total gas age of 9.70 ± 0.05 Ma. No plateau or isochron ages were produced for this sample. A preferred age of 7.51 ± 0.26 Ma was calculated using steps 1 through 8 (82.3% of the total ^{39}Ar released; Fig. 4.06). Steps 9 and 10 were rejected because they were inconsistent with the majority of the steps, yielding significantly older ages. Relatively high radiogenic yields and consistently high Ca/K ratios indicate that a pure, unaltered plagioclase separate was analyzed.

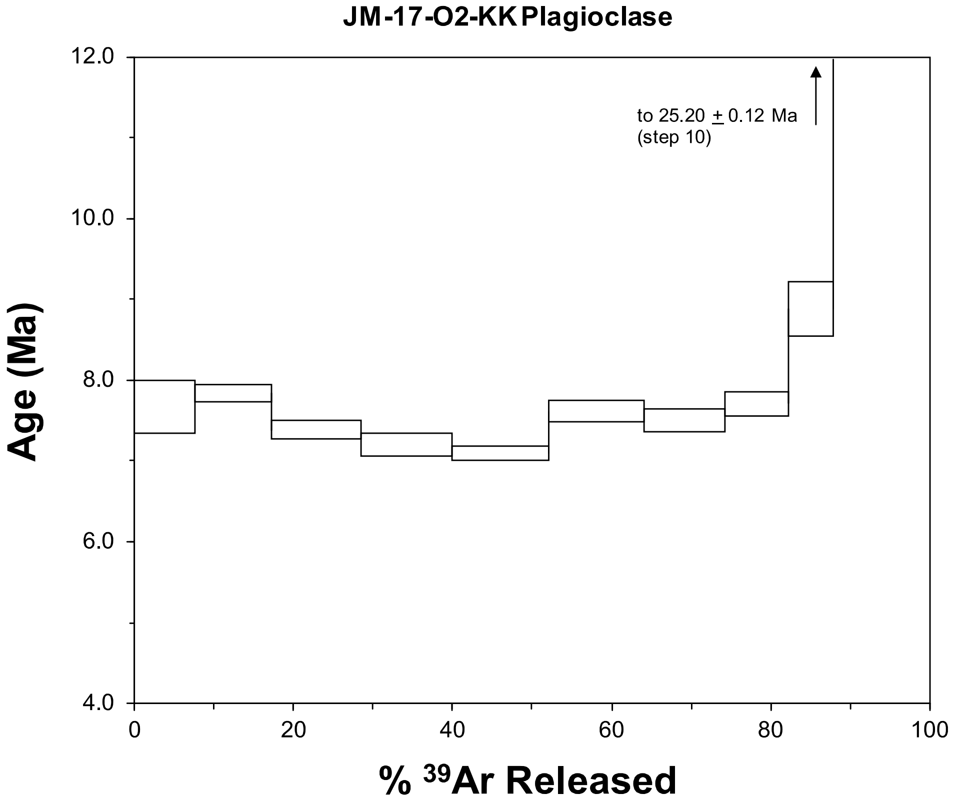

Figure 4.06. ^{40}Ar/^{39}Ar age spectrum for JM-17-O2-KK Plagioclase.

Biotite

JM-17-O2-KK biotite produced a moderately discordant 14 step age spectrum and yielded a total gas age of 8.97 ± 0.04 Ma. No plateau or isochron ages were defined for this sample. Steps 7 through 14 (60.4% of the total ^{39}Ar released) yield a preferred age of 8.05 ± 0.18 Ma (Fig. 4.07). Steps 1 through 6 were rejected because they yield ages inconsistent with the majority of the steps, generating ages both younger and older, and had low radiogenic yields. Consistently low Ca/K ratios indicate that the sample analyzed was a pure biotite separate, but low radiogenic yields indicate that it was not completely unaltered.

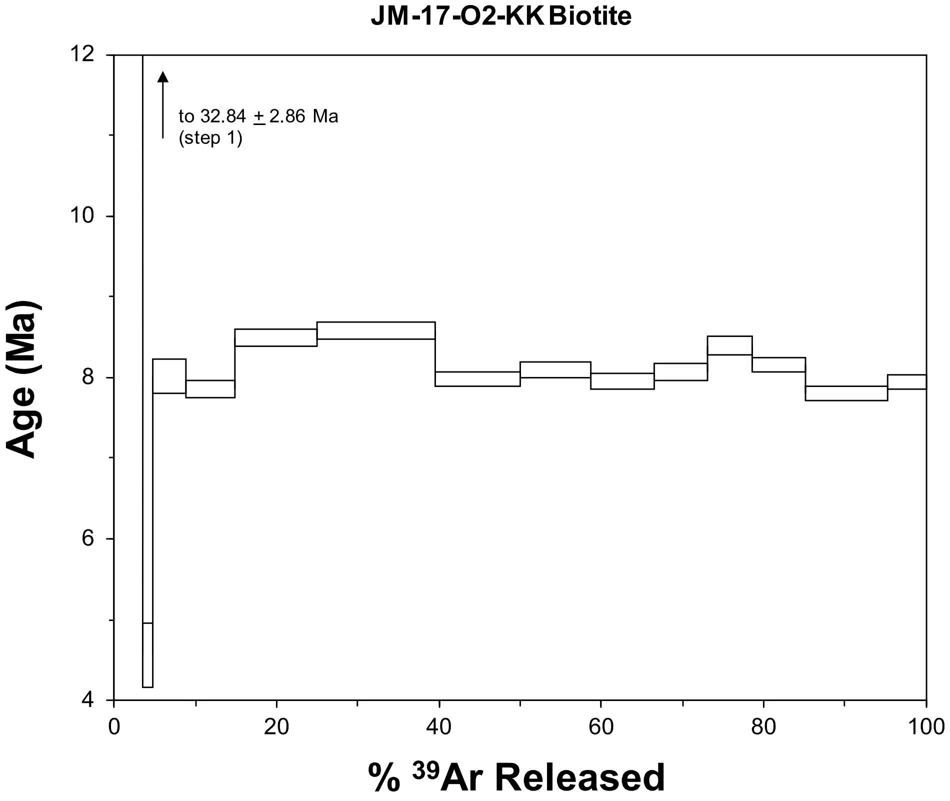

Figure 4.07. ^{40}Ar/^{39}Ar age spectrum for JM-17-O2-KK Biotite.

4.2.2 Intermediate Rhyolite

Plagioclase

Plagioclase from sample JM-18-M2-KK produced a generally concordant 12 step age spectrum which yielded a total gas age of 7.27 ± 0.03 Ma. No isochron or plateau ages were produced for this sample. Steps 3 through 12 (90.0% of the total ^{39}Ar released) define a preferred age of 7.05 ± 0.24 Ma (Fig. 4.08). Steps 1 and 2 were rejected based on low radiogenic yields and ages inconsistent with the majority of the steps, with one step being younger and one older. Low radiogenic yields and slightly low Ca/K ratios indicate that the sample analyzed was not a pure, completely unaltered plagioclase separate.

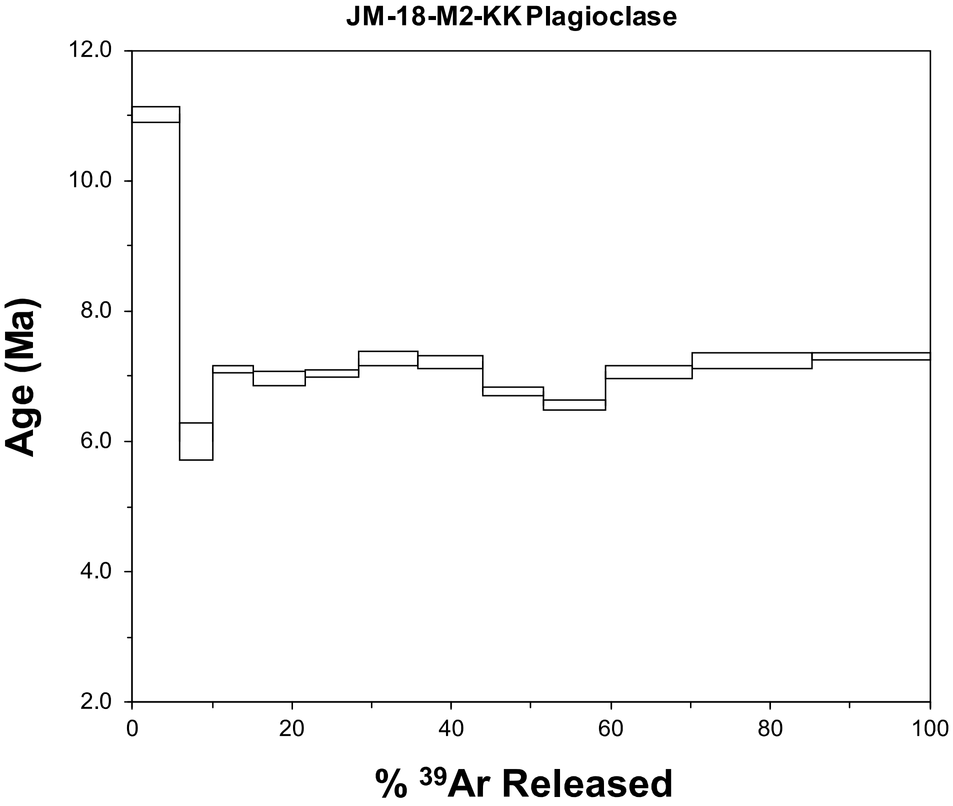

Figure 4.08. ^{40}Ar/^{39}Ar age spectrum for JM-18-M2-KK Plagioclase.

4.2.3 Pumice Ring Rhyolite

Biotite

JM-17-O2-KK biotite yielded a discordant 12 step age spectrum and a total gas age of 5.30 ± 0.04 Ma. No plateau or isochron ages were produced for this sample. A preferred age of 5.61 ± 0.48 Ma was calculated using steps 2 through 12 (90.6% of the total ^{39}Ar released; Fig. 4.09). Step 1 was rejected based on low radiogenic yield and an anomalously low age compared to the majority of the steps. Consistently low Ca/K ratios indicate that the sample analyzed was a pure biotite separate, but very low radiogenic yields indicate that it was not completely unaltered.

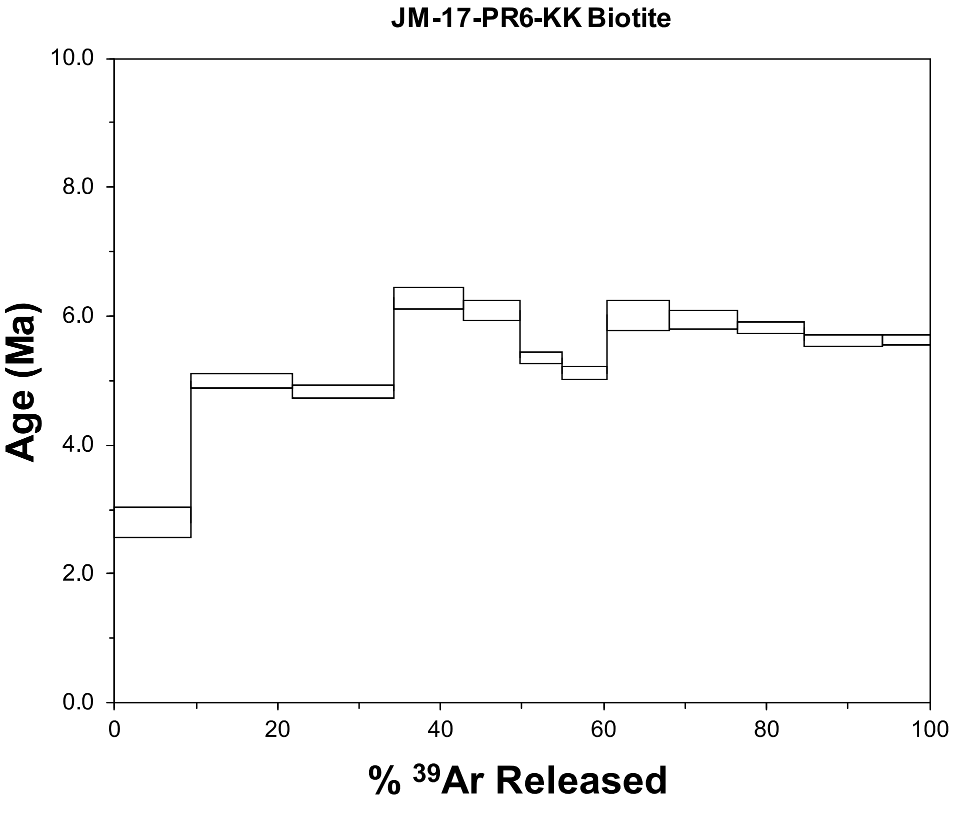

Figure 4.09. ^{40}Ar/^{39}Ar age spectrum for JM-17-PR6-KK Biotite.

Amphibole

A highly discordant age spectrum was produced for JM-17-PR6-KK amphibole, yielding a total gas age of 2.27 ± 0.09 Ma. A preferred age of 4.31 ± 2.31 Ma was calculated using only positive age steps 3 through 5 (81.7% of the total ^{39}Ar released; Fig. 4.10). Steps 1, 2, and 6 were rejected based on negative radiogenic yields. Low and negative radiogenic yields and inconsistent Ca/K ratios indicate that the sample analyzed was not a pure, completely unaltered amphibole separate.

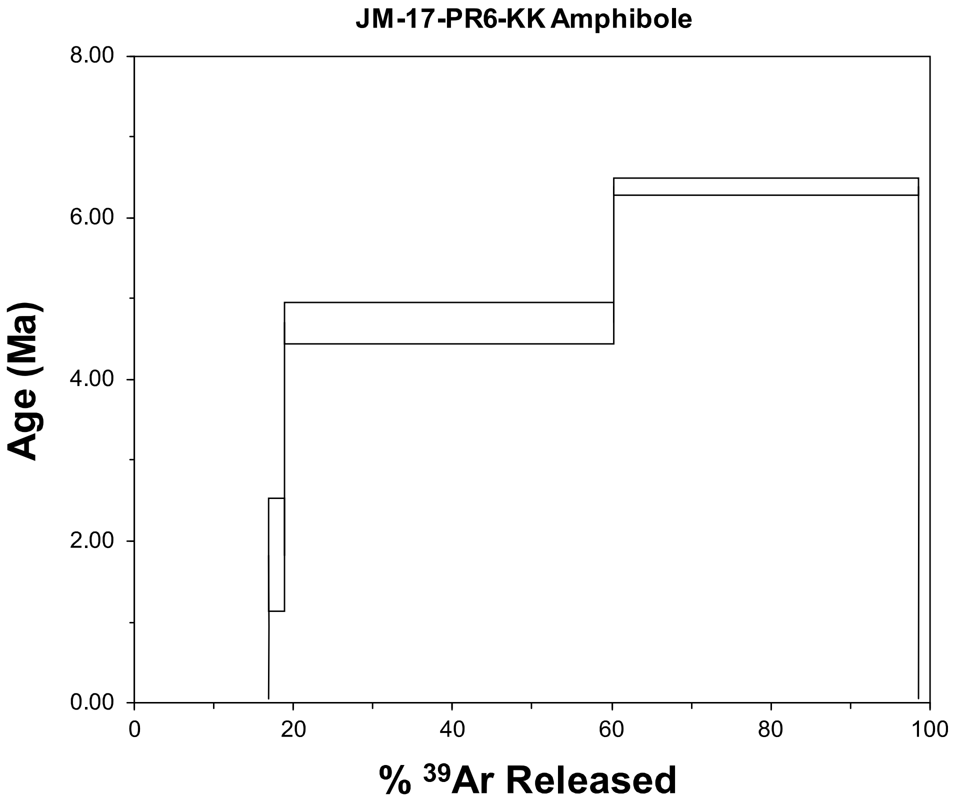

Figure 4.10. ^{40}Ar/^{39}Ar age spectrum for JM-17-PR6-KK Amphibole.

4.2.4 El Rechuelos Rhyolite Northern Dome

Plagioclase

JM-17-ERN3-KK plagioclase produced a moderately concordant 14 step age spectrum and yielded a total gas age of 2.47 ± 0.01 Ma. No isochron or plateau ages were produced for this sample, however a pseudo isochron was produced, with an age of 1.92 ± 0.02 Ma (Fig. 4.11). A pseudo isochron is produced from step heating runs with 40-50% of ^{39}Ar released in 3 or more steps, rather than the usual 50% or more gas released. A preferred age of 2.23 ± 0.15 Ma was calculated from steps 5 through 13 (78.3% of the total ^{39}Ar released). Steps 1 through 4 and 14 were rejected based on low radiogenic yields and anomalously old ages compared with the majority of steps. Low radiogenic yields and low Ca/K ratios indicate that the sample analyzed was not a pure, completely unaltered plagioclase separate. Mineral separation for this unit, in addition to the other El Rechuelos units, was very difficult, as heavy liquid density separations did not sufficiently remove the glass, despite numerous rounds of separations with differing densities.

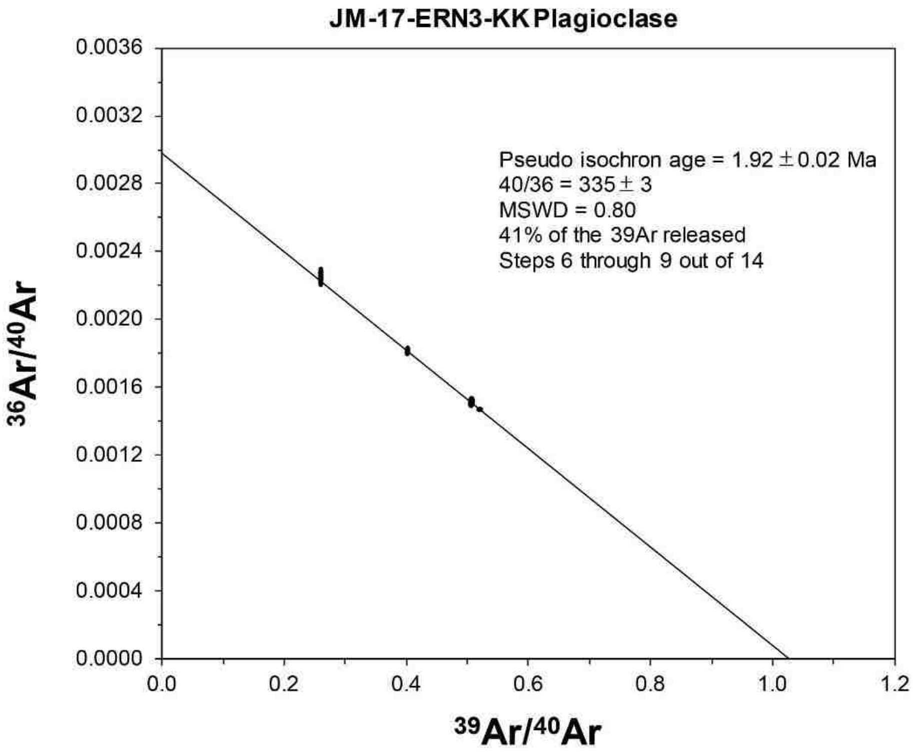

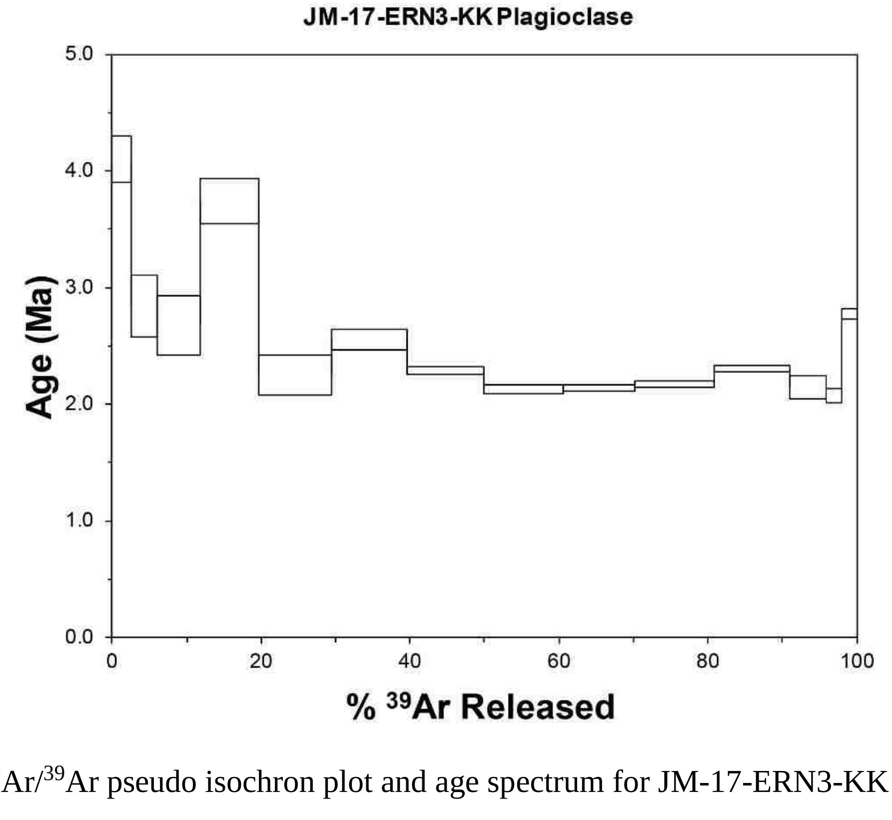

Figure 4.11. ^{40}Ar/^{39}Ar pseudo isochron plot and age spectrum for JM-17-ERN3-KK Plagioclase.

4.2.5 El Rechuelos Rhyolite Central Dome

Feldspar Plus Glass

JM-17-ERC5-KK feldspar plus glass produced a highly discordant 11 step age spectrum and did not yield an isochron or a plateau age. The total gas age is 1.78 ± 0.07 Ma (Fig. 4.12). A preferred age could not be calculated for this sample. Due to extremely low radiogenic yields and the highly discordant age spectrum, this sample does not provide a reliable age constraint. Low radiogenic yields and inconsistent Ca/K ratios indicate that the analyzed sample was not a pure feldspar separate and contained hydrated glass, which was expected, based on the difficulties of the mineral separation.

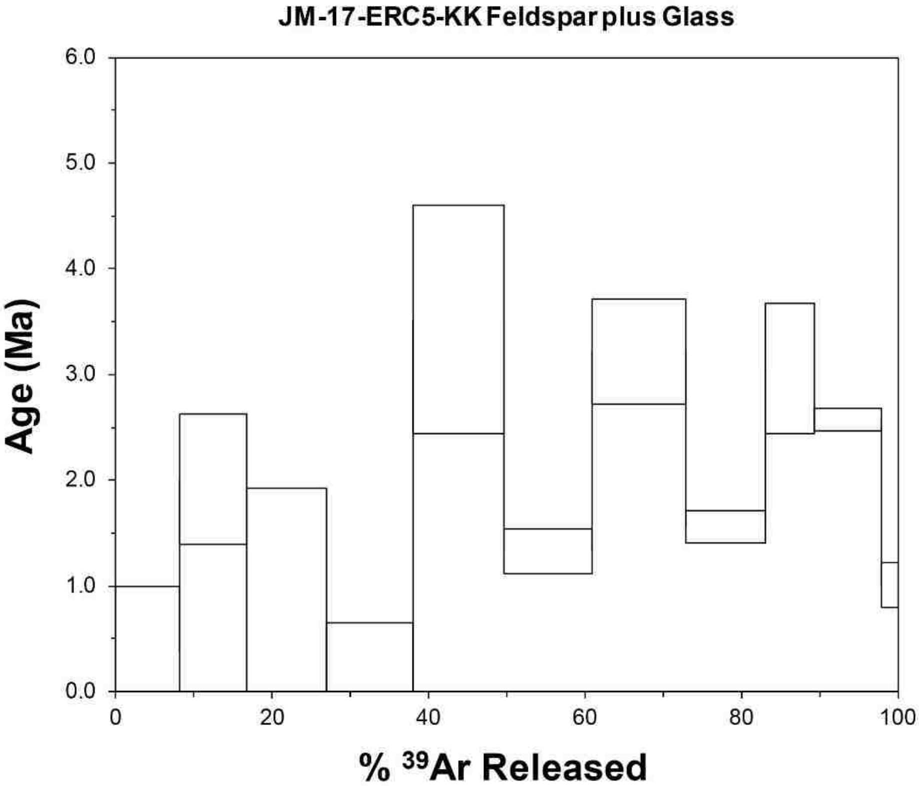

Figure 4.12. ^{40}Ar/^{39}Ar age spectrum for JM-17-ERC5-KK Feldspar plus Glass.

4.2.6 El Rechuelos Rhyolite Southern Dome

Feldspar Plus Glass

JM-17-ERS2-KK feldspar plus glass produced a highly discordant 13 step age spectrum and yielded neither an isochron nor a plateau age. The total gas age is 2.97 ± 0.06 Ma (Fig. 4.13). A preferred age could not be calculated for this sample. Due to extremely low radiogenic yields and the highly discordant age spectrum, this sample does not give a reliable age constraint. Low radiogenic yields and inconsistent Ca/K ratios indicate that the analyzed sample was not a pure feldspar separate and contained hydrated glass, which was expected, based on the difficulties of the mineral separation.

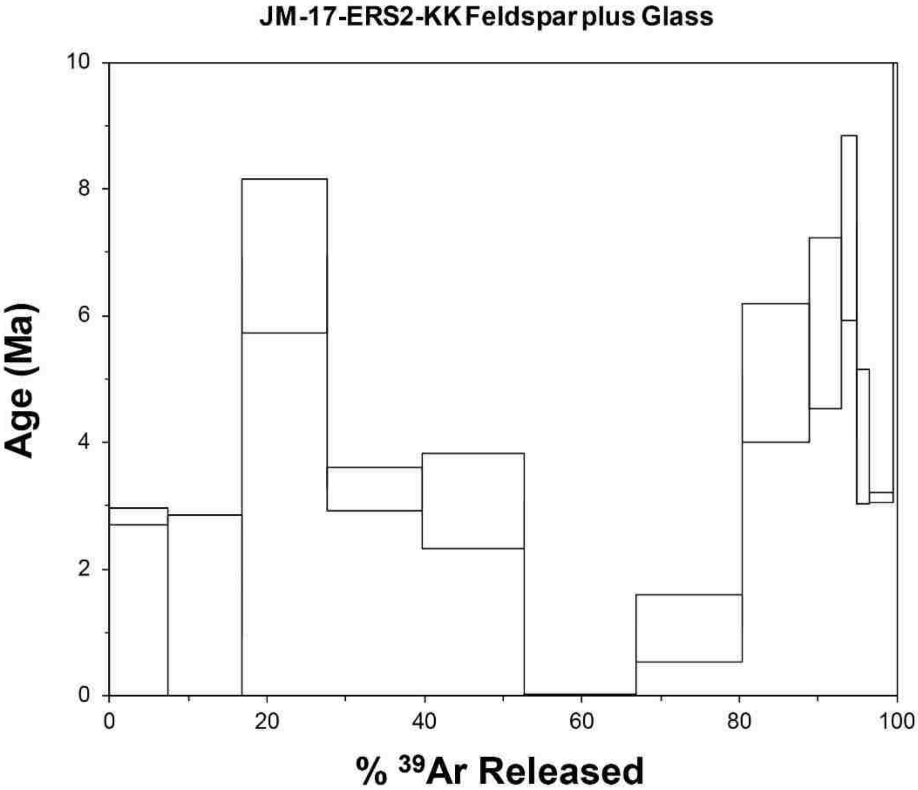

Figure 4.13. ^{40}Ar/^{39}Ar age spectrum for JM-17-ERS2-KK Feldspar plus Glass.

4.2.7 Young Rhyolite

Anorthoclase

Anorthoclase from sample JM-17-I2-KK produced a generally concordant 13 step age spectrum, with a total gas age of 1.22 ± 0.01 Ma (Fig. 4.14). A slightly younger plateau age of 1.19 ± 0.01 Ma is defined from steps 5 through 12 (86.2% of the total ^{39}Ar released). Steps 6 through 11 produce an isochron age of 1.09 ± 0.07 Ma, with 63% of the ^{39}Ar released. Although statistically valid, this isochron is poorly constrained, as the data cluster together. Radiogenic yields and Ca/K ratios indicate that a pure, unaltered anorthoclase separate was analyzed. The plateau age of 1.19 ± 0.01 Ma is the preferred age for this sample.

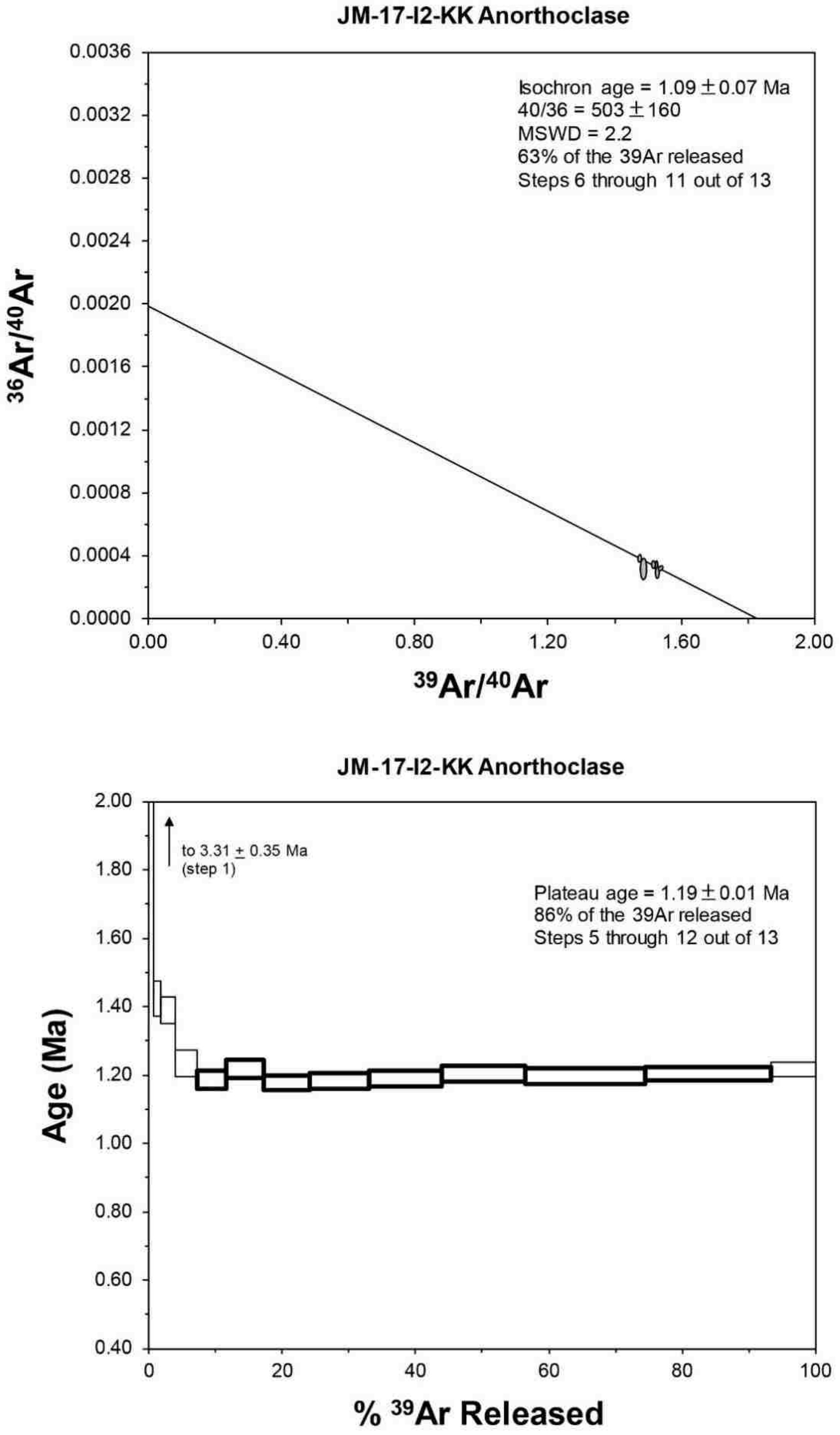

Figure 4.14. ^{40}Ar/^{39}Ar isochron plot and age spectrum for JM-17-I2-KK Anorthoclase. Plateau shown in bold.

4.3 Geochemistry

4.3.1 Major Element Geochemistry

All analyzed samples are classified as rhyolite on the Le Bas et al. (1986) classification diagram (Fig. 4.15). The samples plot as four distinct clusters, with the Early, Pumice Ring, and Young rhyolites plotting as separate groups, and the north, central, and south El Rechuelos units and the Intermediate Rhyolite plotting together as a fourth cluster. Appendix C contains the XRF major element data.

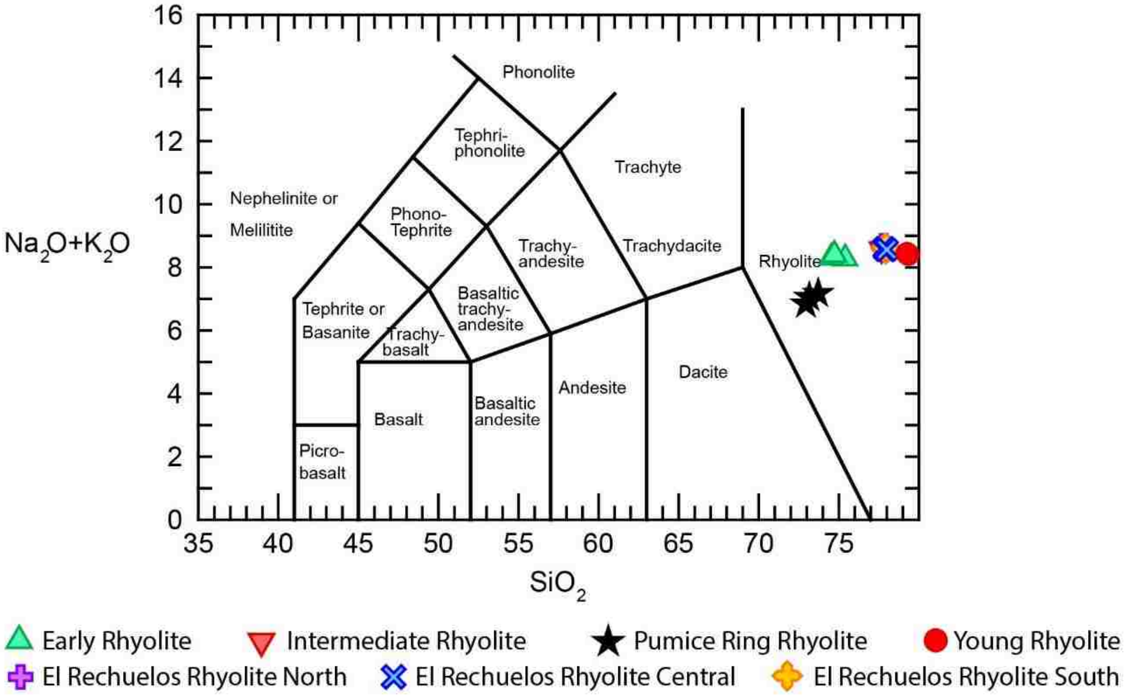

Figure 4.15. XRF data for the seven units plotted on the Le Bas (1986) classification diagram. Oxides are in weight percent and normalized to 100% volatile free.

On Harker variation diagrams (major elements versus SiO_2), the units generally plot in four distinct clusters, as described above (Fig. 4.16). On most plots, the Intermediate Rhyolite and the El Rechuelos Rhyolite samples plot together, while the Early Rhyolite, Pumice Ring

Rhyolite, and Young Rhyolite all plot as separate groups. Some general trends are apparent between major elements and increasing SiO_2. Al_2O_3 and CaO display a nearly linear decrease, while TiO_2 and MgO show a general decrease. With the exception of one sample of the Pumice Ring Rhyolite and the Young Rhyolite, there is a general decrease of FeO. There is a general increase in K_2O. Na_2O and P_2O_5 do not show any apparent trends.

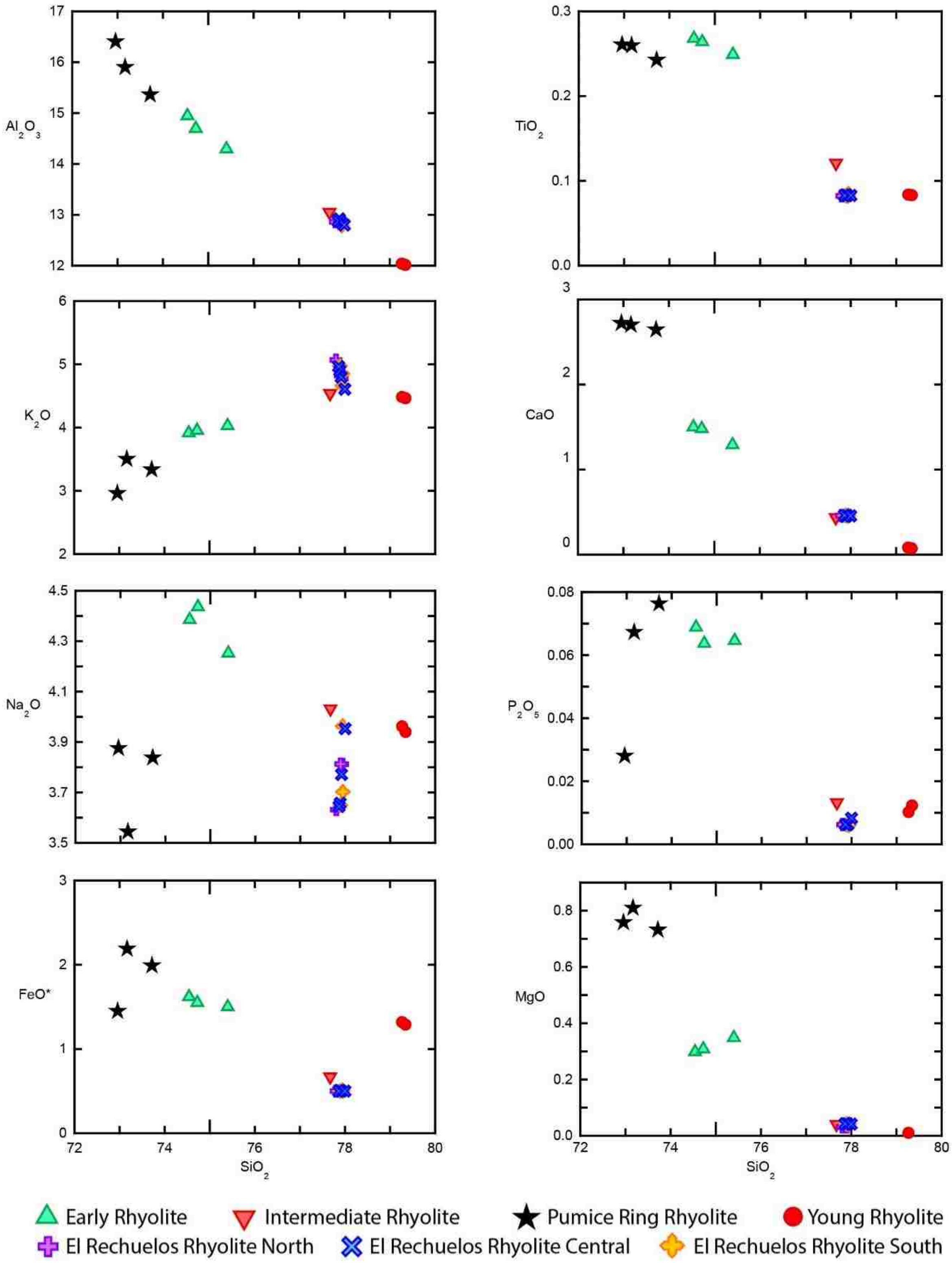

Figure 4.16. Major element Harker variation diagrams of the seven units. Oxides in weight percent and normalized to 100% volatile free. Two-sigma uncertainty is smaller than symbols shown.

4.3.2 Trace Element Geochemistry

Compatible and incompatible trace elements were plotted to show potential chemical evolution trends, such as those produced by fractional crystallization. When plotting trace elements, an incompatible, immobile trace element, such as Ta, Th, Y, or Nb, should be used on the x-axis. For this study, Nb was chosen, as it is highly immobile and incompatible, and exhibits a wide range of concentrations. Incompatible elements are those that partition into the melt more readily than into a crystal structure, due to the size of their ionic radii and bonded charge states (Rollinson, 1993; Chapter 4). Immobile elements are those that are resistant to modification by hydration or alteration (Rollinson, 1993; Pearce, 1996; Jowitt et al., 2014). All trace element data are located in Appendices C and D.

The plots of trace elements versus Nb can be grouped based on their trends with increasing Nb (Fig. 4.17, 4.18). Elements for which an increase with Nb is seen exhibit incompatible behavior, whereas those that display a decrease show compatible behavior. Plots of Ce, Nd, Lu, Yb, Y, Ba, and Zn show an increase in content from the Pumice Ring Rhyolite to the Early Rhyolite, then a decrease from the Early Rhyolite to the El Rechuelos units, then an increase from the El Rechuelos units to the Young Rhyolite. Eu shows an increase in content from the Pumice Ring Rhyolite to the Early Rhyolite, then a decrease in content, while U shows an increase from the Pumice Ring Rhyolite to the El Rechuelos units then a decrease. There is a general increase of Ta, Th, and Rb, and a general decrease of Sr.

The Young Rhyolite samples have the highest concentrations of incompatible trace elements and the lowest concentrations of compatible trace elements. The Pumice Ring Rhyolite samples generally have the lowest concentrations of incompatible elements and the highest concentrations of compatible trace elements. The Early, Intermediate, and El Rechuelos rhyolites tend to have intermediate amounts of incompatible and compatible trace elements. Exceptions to these trends can be seen in Zn and Ba. The Pumice Ring and Early Rhyolite samples contain about the same amount of Zn, while the Young Rhyolite contains significantly more Zn than any of the other samples. The Early Rhyolite samples contain more Ba than the Pumice Ring samples and the El Rechuelos samples contain less Ba than the Young samples.

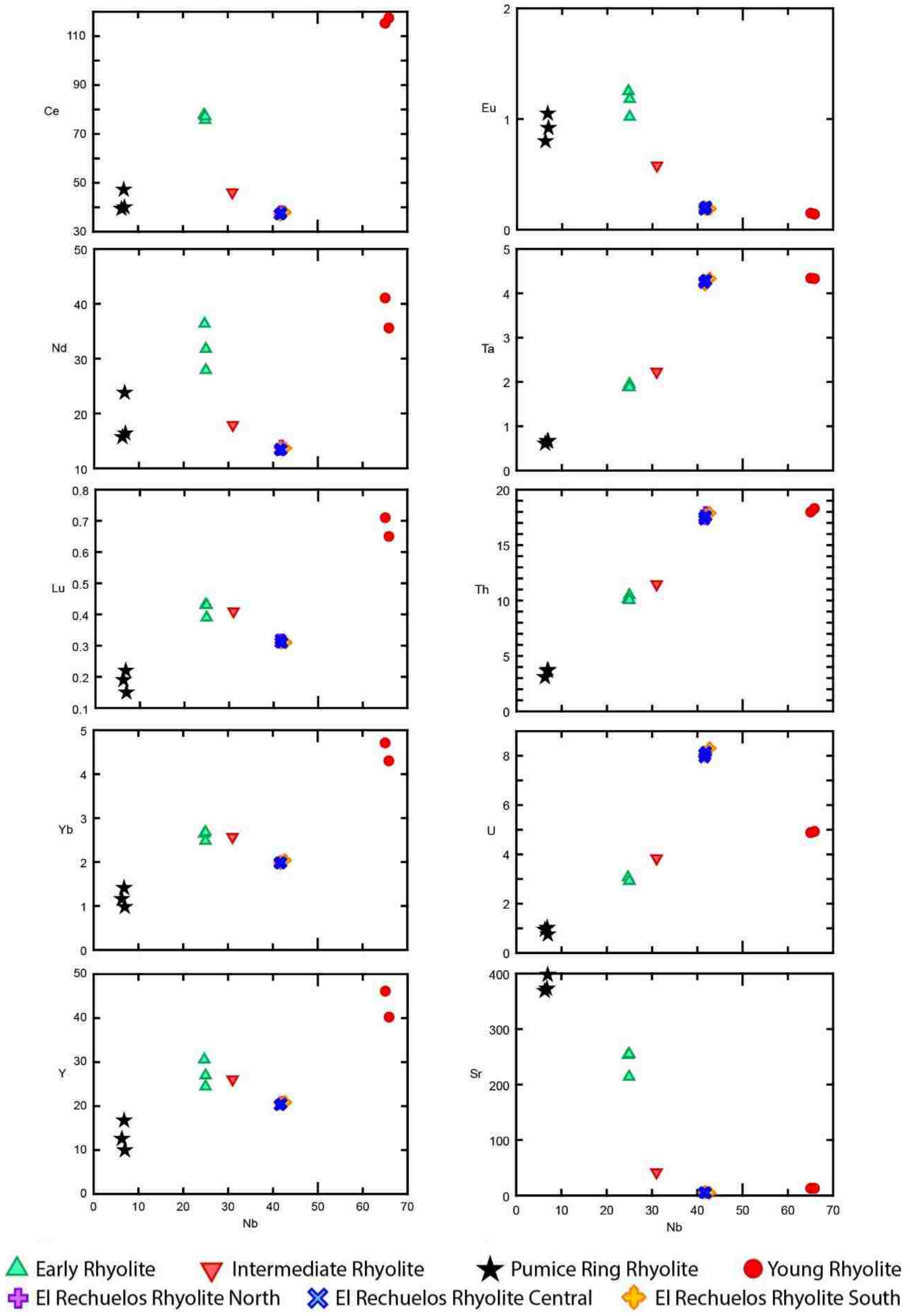

Figure 4.17. Trace elements (ICP-MS) versus Nb (ICP-MS). Trace elements in ppm. Two-sigma uncertainty is smaller than symbols shown.

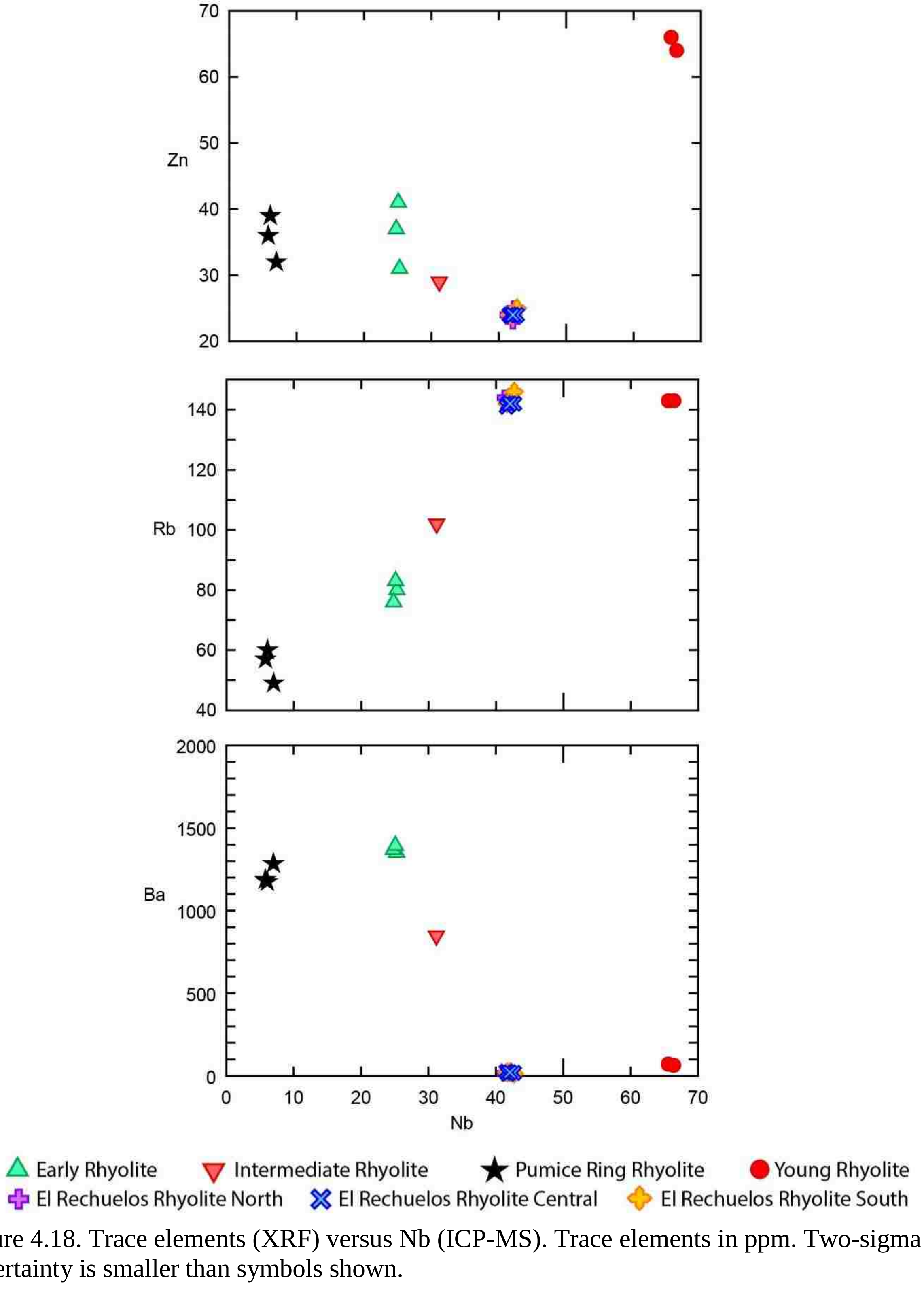

Figure 4.18. Trace elements (XRF) versus Nb (ICP-MS). Trace elements in ppm. Two-sigma uncertainty is smaller than symbols shown.

4.3.3 Ratios of Incompatible Trace Elements

Ratios of similarly incompatible trace elements are plotted because relative proportions of these elements may represent the initial composition of the magma, as they tend to be relatively unaffected by processes such as fractional crystallization (Liu et al., 2014). Plotted elemental ratios were chosen because the elements are similarly incompatible, having small ionic radii and high charges, in addition to being highly immobile. Nb was again chosen for the x-axis, due to its incompatible and immobile nature. In general, these plots do not follow any trends with increasing Nb, and there is a large variability in ratios between units (Fig. 4.19).

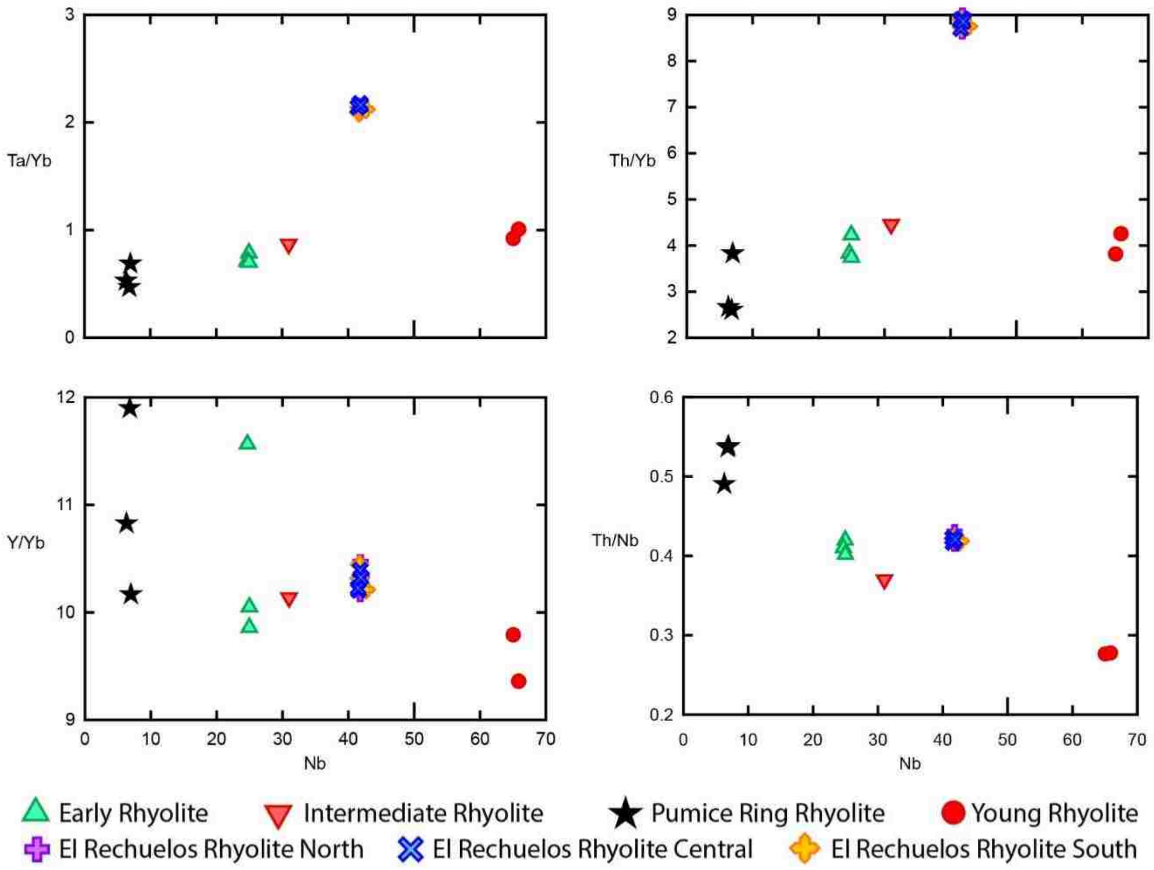

Figure 4.19. Ratios of incompatible trace elements (ICP-MS) versus Nb (ICP-MS). Trace elements in ppm. Two-sigma uncertainty is smaller than symbols shown.

4.3.4 REE and Primitive Mantle Multi-Element Variation Diagrams

On rare earth element (REE) plots, the elements are arranged from lightest to heaviest on the x-axis, versus normalized rock/chondrite values on a logarithmic scale on the y-axis. All seven of the units exhibit a generally similar pattern, but are distinct from one another (Fig. 4.20). There is generally a negative slope among the light rare earth elements (LREE) and a flat to slightly positive slope among the heavy rare earth elements (HREE). Ratios of La/Yb indicate negative slopes for the REEs for all units. Additionally, a negative Eu anomaly is typically present, although it varies among the units, especially for the Pumice Ring Rhyolite where there is little to no anomaly (Eu/Eu* = ~0.694-0.813). The Early Rhyolite has a very small Eu anomaly (Eu/Eu* = ~0.557-0.647), whereas the Young Rhyolite has a large Eu anomaly (Eu/Eu* = ~0.054-0.062). The Intermediate Rhyolite has a moderate europium anomaly (Eu/Eu* = ~0.408) and the El Rechuelos units all have an identical Eu anomaly that is also relatively large (Eu/Eu* = ~0.194). Aside from the Eu anomaly, the overall abundance of REEs varies, with the Young Rhyolite having the highest concentrations overall, and the El Rechuelos Rhyolite having the lowest LREE concentrations while the Pumice Ring Rhyolite has the lowest HREE concentrations.

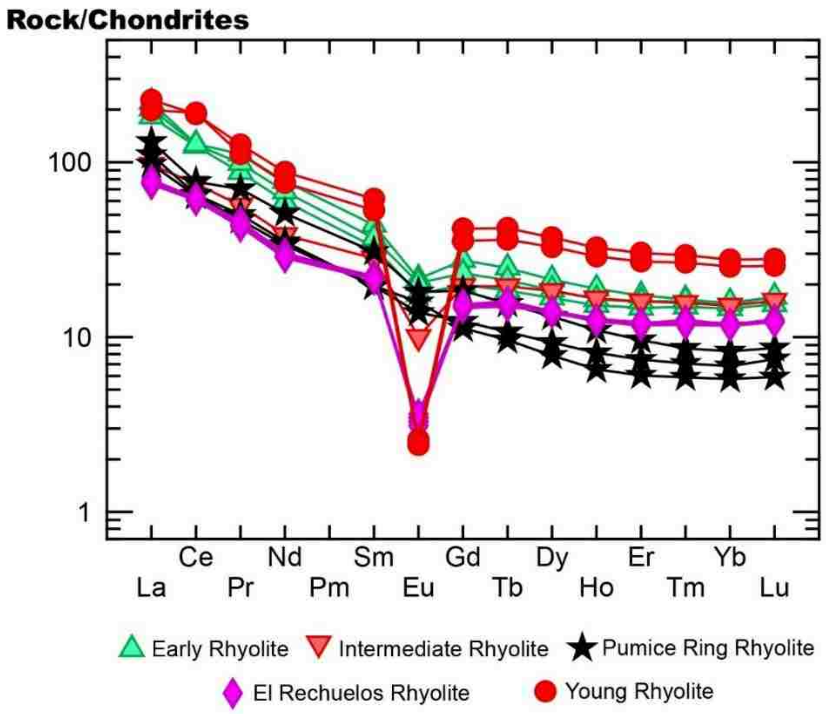

Figure 4.20. Normalized rare earth element diagram. All El Rechuelos Rhyolite samples plotted in same color for simplification. Chondrite normalizing values from Sun and McDonough (1989).

A primitive mantle-normalized multi-element variation diagram is shown in Fig. 4.21. A major positive Pb anomaly for all units can be seen on this diagram, and major distinctions can be seen between units, especially in Ba, Nb, Sr, and Eu where values vary widely. The Early and Pumice Ring rhyolites have positive Ba anomalies, while the other units have negative Ba anomalies. The Intermediate Rhyolite has a very minimal negative Ba anomaly, the Young Rhyolite has a large, negative Ba anomaly, and the El Rechuelos units have negative Ba anomalies that are identical. The Pumice Ring Rhyolite has a large, negative Nb anomaly, differing from the small Nb anomalies of all other units. Additionally, the Sr and Eu anomalies for the Early and Pumice Ring units are smaller than the Sr and Eu anomalies of the other units.

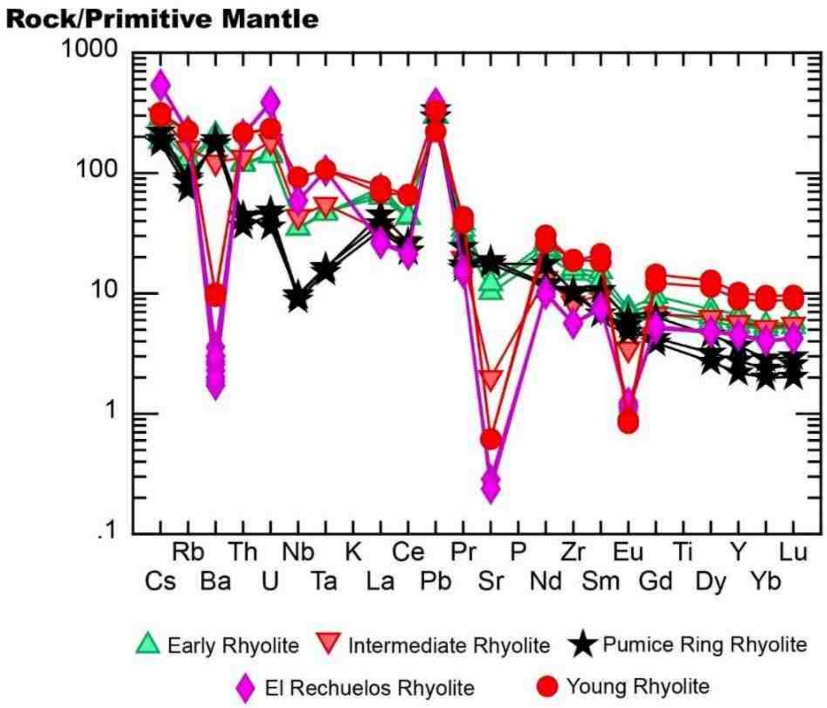

Figure 4.21. Normalized multi-element variation diagram. All El Rechuelos Rhyolite samples plotted in same color for simplification. Primitive mantle values from Sun and McDonough (1989).

4.4 Mineral Major Element Compositions

Feldspar phenocrysts were analyzed via electron microprobe for samples JM-17-O2-KK (Early Rhyolite), JM-18-M2-KK (Intermediate Rhyolite), JM-17-PR6-KK (Pumice Ring Rhyolite), JM-17-ERN-KK (northern dome of El Rechuelos Rhyolite), and JM-17-I2-KK (Young Rhyolite). Thin sections for samples JM-17-ERC5-KK (central dome of El Rechuelos Rhyolite) and JM-17-ERS2-KK (southern dome of El Rechuelos Rhyolite) did not contain suitable feldspar phenocrysts for analysis, due to lack of abundance and small size of crystals. Crystal targets included some euhedral phenocrysts, and phenocrysts with dissolution features and/or petrographically visible rims. Where possible, rim to rim transects were obtained. Data tables for analyzed feldspars can be found in Appendix E.

Additionally, some mafic and oxide minerals were analyzed for samples JM-17-O2-KK, JM-18-M2-KK, JM-17-PR6-KK, JM-17-ERN-KK, JM-17-ERC5-KK, JM-17-ERS2-KK, and JM-17-I2-KK. Crystal targets included biotite, amphibole, and bright areas (identified by backscatter EMP images) indicative of oxides, for documentation of crystal chemistry. Data tables for analyzed mafic and oxide minerals can be found in Appendices F and G.

4.4.1 EPMA of the Early Rhyolite

Although the Early Rhyolite contains both sanidine and plagioclase feldspar, sanidine is sparse compared to plagioclase, and was not analyzed by EPMA. As detailed in the petrography section of this chapter, plagioclase crystals are subhedral to euhedral and display albite and carlsbad twinning and concentric, and oscillatory zonation.

Analyzed plagioclase from this unit generally falls into two compositional groups, based on ternary feldspar plots; oligoclase ranging from ~An_{24}-An_{33} rims to ~An_{27}-An_{38} cores and andesine ranging from ~An_{47}-An_{50} for both cores and rims (Fig. 4.23). Weak normal zonation is found in some of the more sodic plagioclase feldspar crystals in the Early Rhyolite, but no zonation is found in the calcic plagioclase (Fig. 4.22).

Mafic and oxide minerals were identified through quantitative EPMA spot analyses and include biotite, magnetite, ilmenite, apatite, and zircon (Appendix F). Biotite averages ~14.5-22.0% Fe and ~12.5-15.0% Mg.

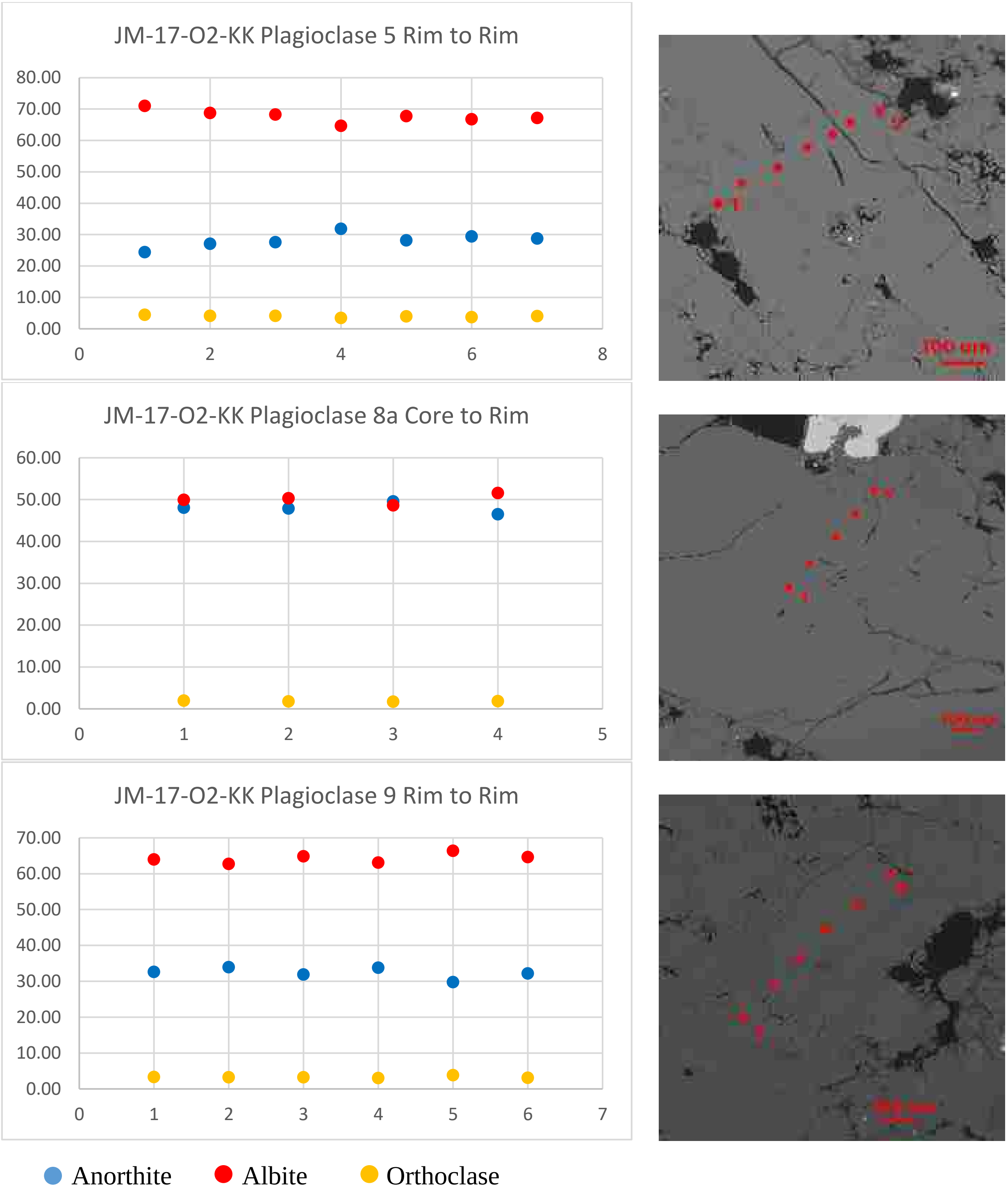

Figure 4.22. Representative EPMA transects across plagioclase crystals in the Early Rhyolite, along with BSE images of each analyzed crystal with transect plotted in red. Percent Anorthite, Albite, and Orthoclase denoted by symbols.

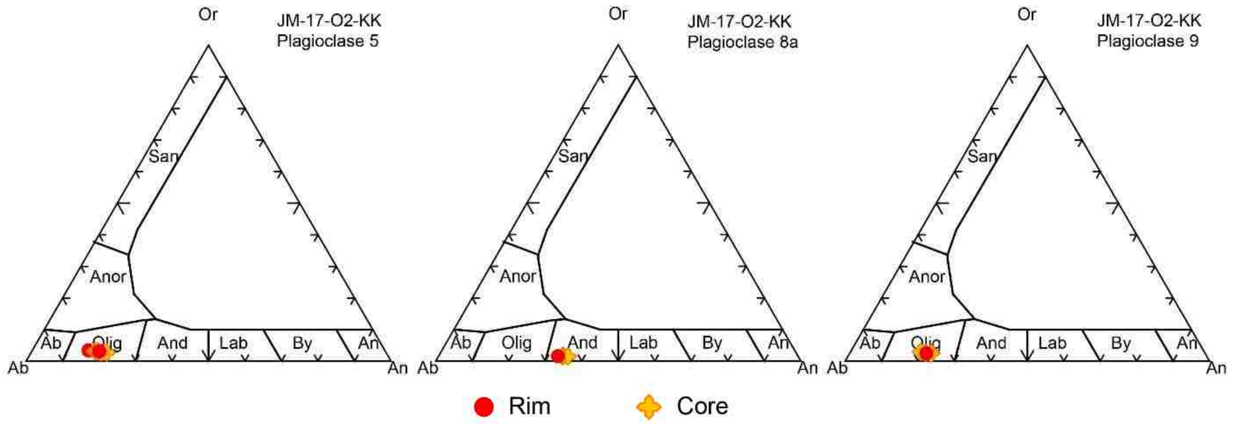

Figure 4.23. Ternary diagrams of plagioclase from the Early Rhyolite.

4.4.2 EPMA of the Intermediate Rhyolite

The feldspar population of the Intermediate Rhyolite consists of both sanidine and plagioclase feldspar. As described in the petrography section, plagioclase is the dominant feldspar; sanidine is sparse. Plagioclase crystals are anhedral to subhedral, display albite and carlsbad twinning, and are not typically zoned, while sanidine crystals are subhedral to euhedral.

Both plagioclase and sanidine were analyzed from this sample, and representative transects are shown. No significant chemical zonation is observed among feldspar crystals in this unit (Fig. 4.24). Compositions of plagioclase from the Intermediate Rhyolite are on the albite-oligoclase boundary (Fig. 4.25), ranging from ~An$_{10}$-An$_{20}$ for both rims and cores. Sanidine ranges in composition from ~Or$_{53}$-Or$_{55}$ for both rims and cores.

Oxide minerals in the Intermediate Rhyolite were identified through quantitative EPMA spot analyses and include magnetite and ilmenite.

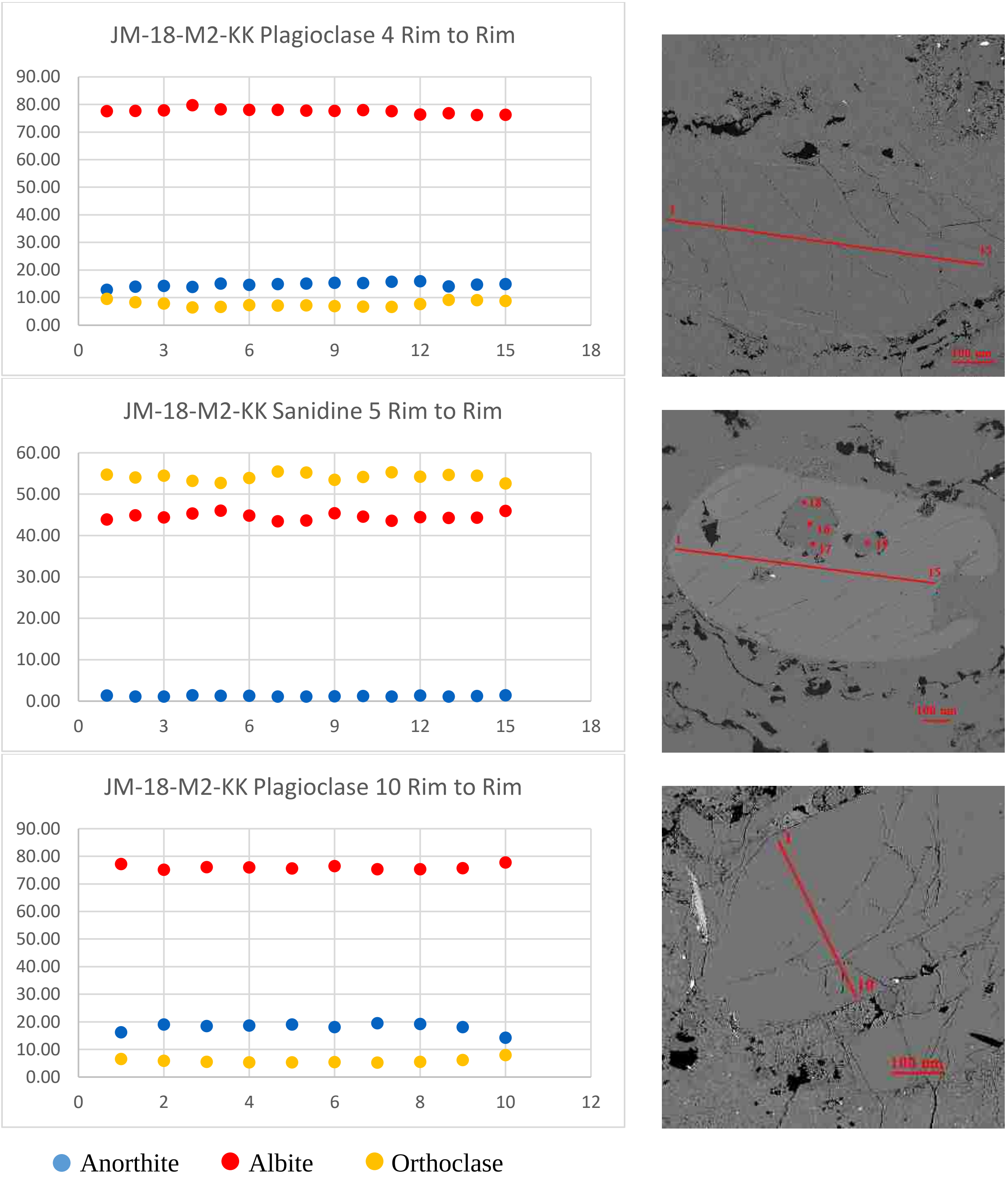

Figure 4.24. Representative EPMA transects across feldspar crystals in the Intermediate Rhyolite, along with BSE images of each analyzed crystal with transect plotted in red. Percent Anorthite, Albite, and Orthoclase denoted by symbols.

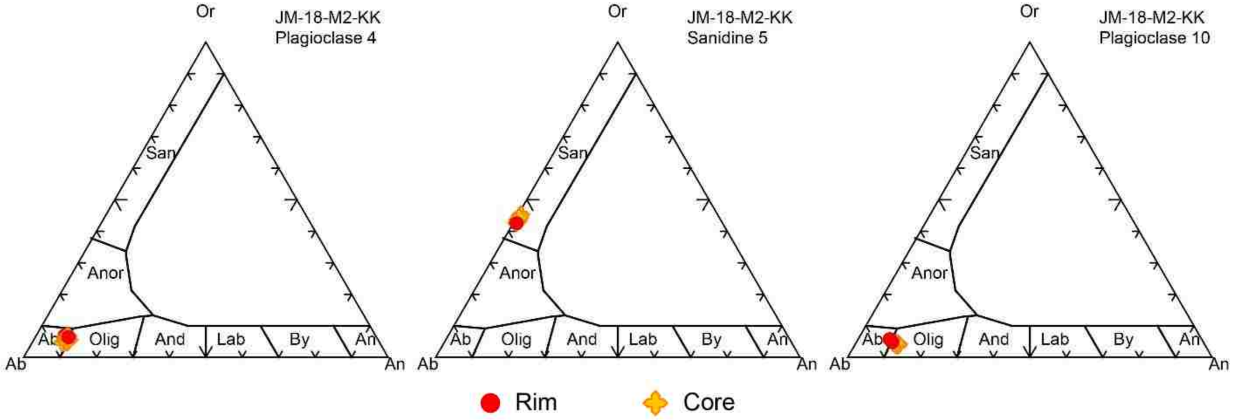

Figure 4.25. Ternary diagrams of feldspars from the Intermediate Rhyolite.

4.4.3 EPMA of the Pumice Ring Rhyolite

The Pumice Ring Rhyolite contains only one feldspar phase, plagioclase. As discussed in the petrography section, plagioclase crystals are anhedral to euhedral, commonly displaying albite and carlsbad twinning and concentric, oscillatory zonation.

Plagioclase feldspars in the Pumice Ring Rhyolite display patchy zonation (Fig. 4.26). Both the core and rim compositions of plagioclase in this unit range from oligoclase to andesine with normally zoned rims ranging from An_{36}-An_{51} and normally zoned cores ranging from An_{31}-An_{53} (Fig. 4.27).

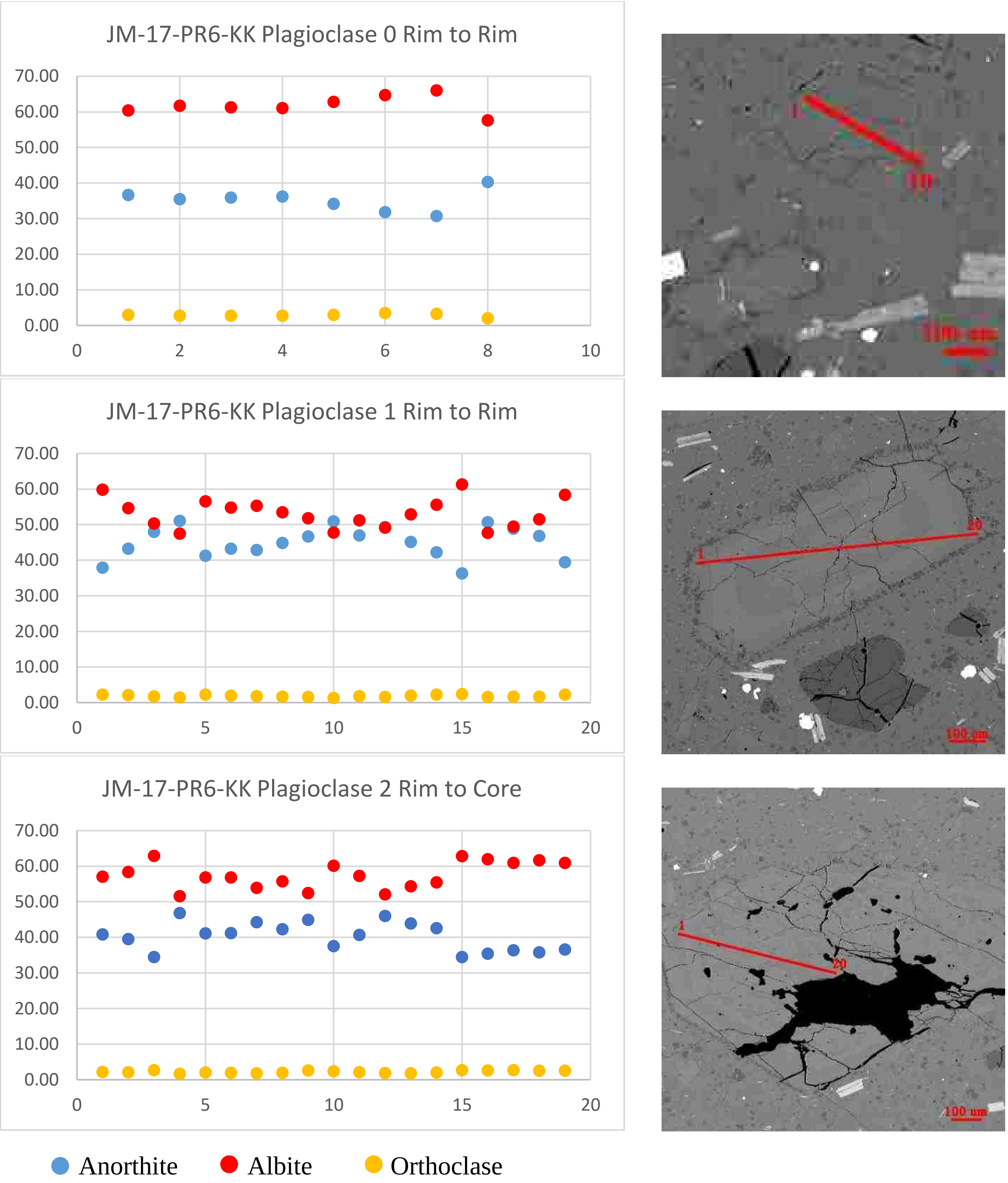

Figure 4.26. Representative EPMA transects across plagioclase crystals in the Pumice Ring Rhyolite, along with BSE images of each analyzed crystal with transect plotted in red. Percent Anorthite, Albite, and Orthoclase denoted by symbols.

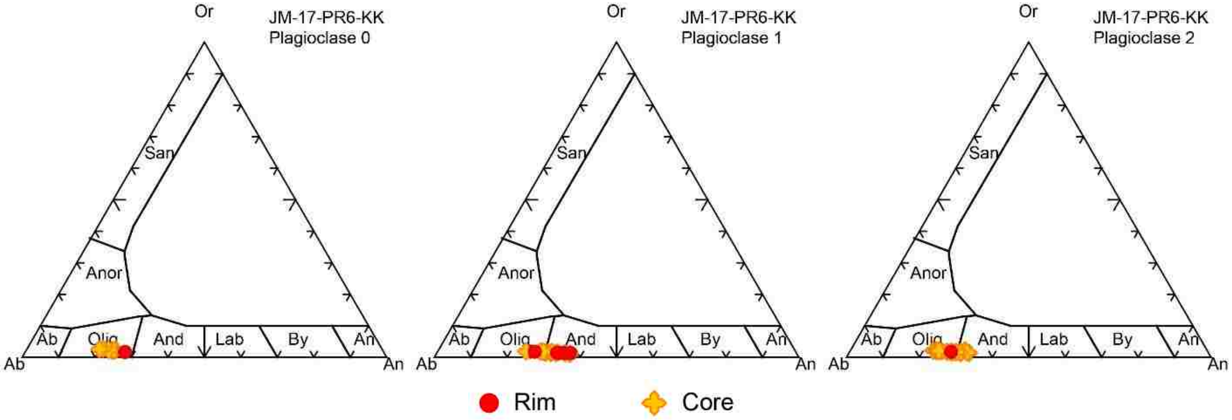

Figure 4.27. Ternary diagrams of plagioclase from the Pumice Ring Rhyolite.

Amphibole and biotite are abundant and relatively large in this unit, allowing for multiple analyses of each, including transects (Appendices F and G). As discussed in the petrography section of this chapter, both amphibole and biotite crystals are subhedral to euhedral.

Petrographic observations did not indicate that amphibole from this sample are optically zoned, nor did EPMA analyses detect any chemically zoned amphibole, although BSE imaging showed one zoned amphibole (Fig. 4.28, 4.29). EPMA transects indicate zonation within biotite (Fig. 4.29). Normal zonation is found among biotite crystals in the Pumice Ring Rhyolite, as the rims are typically less magnesium-rich than the cores.

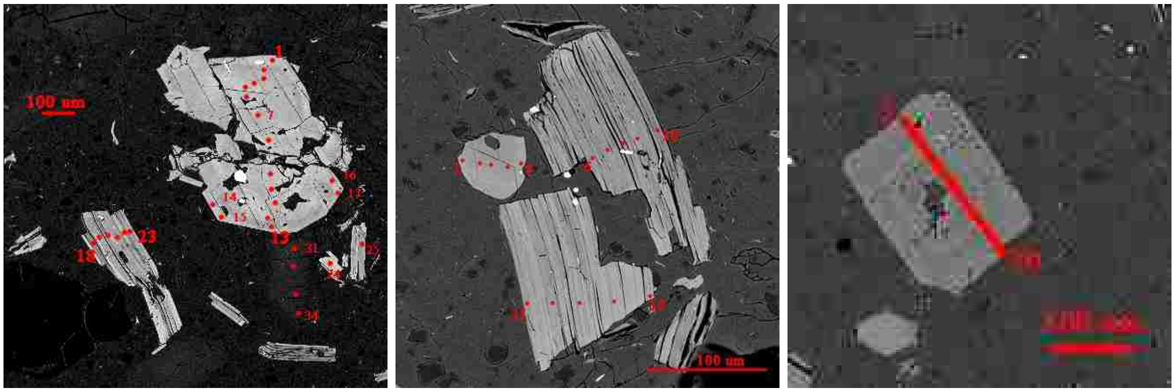

Figure 4.28. BSE images of JM-17-PR6-KK. Left, amphibole 1 and biotite 1a. Center, amphibole 4, biotite 4a and 4b. Right, amphibole 5.

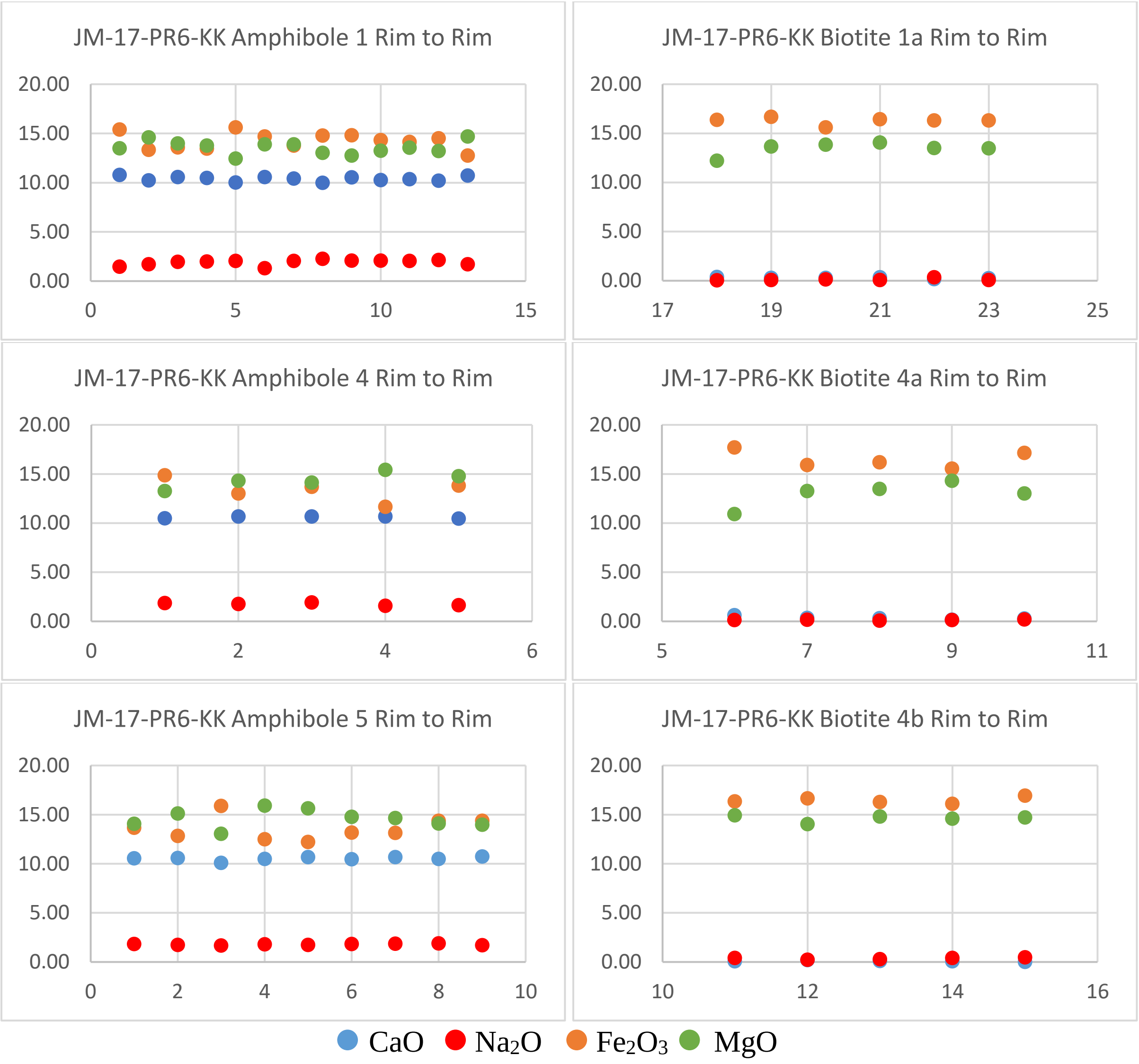

Figure 4.29. Representative EPMA transects across amphibole and biotite crystals in the Pumice Ring Rhyolite. Weight Percent CaO, Na_2O, Fe_2O_3, and MgO denoted by symbols.

4.4.4 EPMA of the El Rechuelos Rhyolite

Feldspars in the El Rechuelos Rhyolite consists of both sanidine and plagioclase feldspar, however, crystals are typically small and very sparse. Feldspar crystals large enough for analysis were only found in the northern El Rechuelos unit. As detailed in the petrography section, plagioclase is the dominant feldspar, and crystals are subhedral to euhedral, while sanidine crystals are anhedral to subhedral.

Zonation is not observed among feldspar crystals in the El Rechuelos Rhyolite (Fig. 4.30). Both plagioclase and sanidine were analyzed for this sample, and representative transects are shown. The core and rim compositions of plagioclase from the El Rechuelos Rhyolite are on the albite-oligoclase boundary, ranging from ~An_{12}-An_{16} (Fig. 4.31). Sanidine compositions range from ~Or_{69}-Or_{71} for both cores and rims.

Mafic and oxide minerals were identified through quantitative EPMA spot analyses in each of the three El Rechuelos domes (Appendix F). The northern dome contains magnetite, ilmenite, and zircon. The central dome contains allanite, zircon, ilmenite, magnetite, and amphibole (~10.0% Fe, ~16.0% Mg). The southern dome contains amphibole (~14.5-21.5% Fe, ~7.5-15.5% Mg), biotite (~12.0-20.0% Fe, ~12.5-15.5% Mg), zircon, and ilmenite.

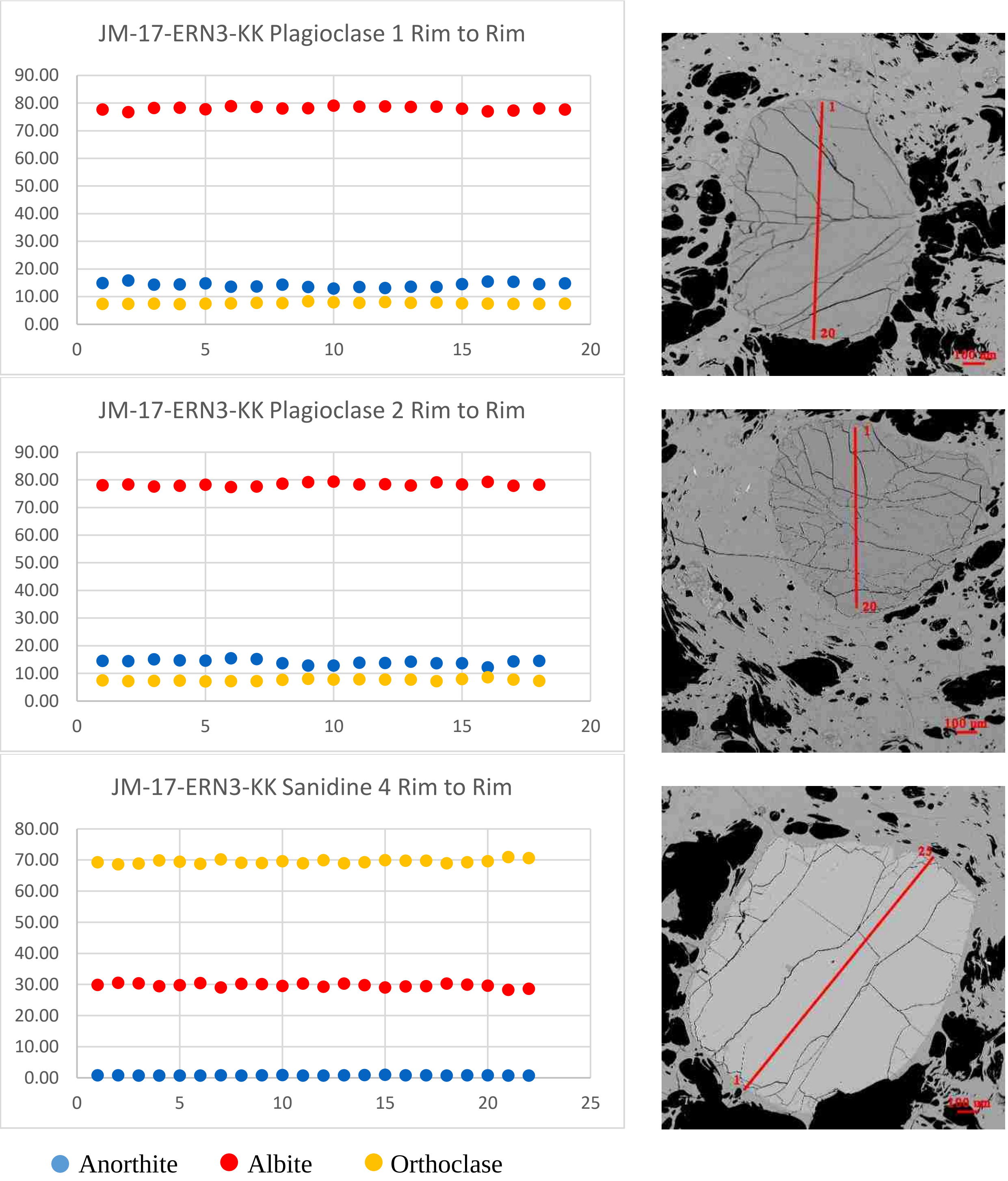

Figure 4.30. Representative EPMA transects across feldspar crystals in the northern dome of the El Rechuelos Rhyolite, along with BSE images of each analyzed crystal with transect plotted in red. Percent Anorthite, Albite, and Orthoclase denoted by symbols.

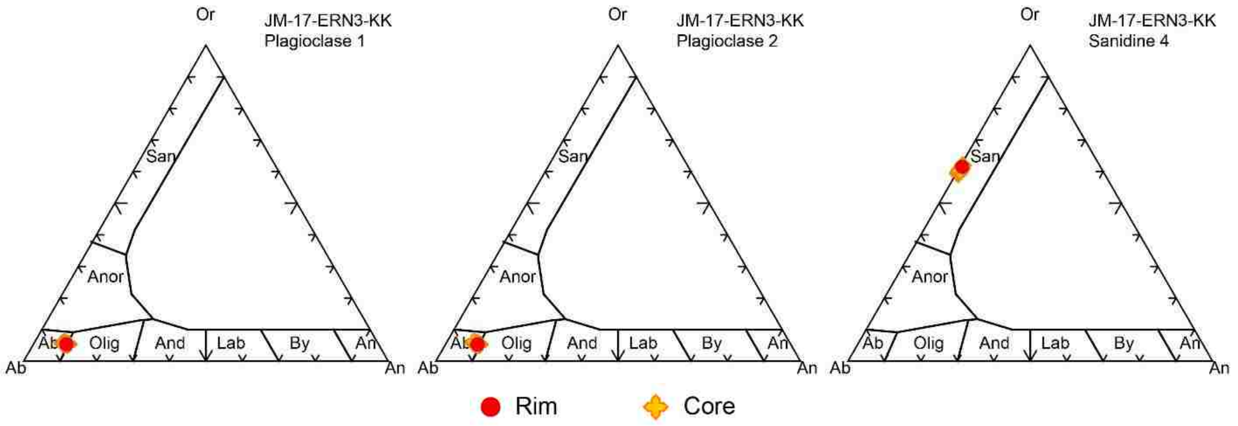

Figure 4.31. Ternary diagrams of feldspar from the northern dome of the El Rechuelos Rhyolite.

4.4.5 EPMA of the Young Rhyolite

The feldspar population of the Young Rhyolite consists of both anorthoclase and plagioclase feldspar. As discussed in the petrography section, anorthoclase (originally thought to be sanidine from petrographic observations) is the dominant feldspar. Plagioclase is sparse in this unit, thus was not analyzed. Anorthoclase crystals are anhedral to euhedral and do not commonly display any unique characteristics, petrographically or chemically.

No significant zonation is observed among anorthoclase crystals in the Young Rhyolite (Fig. 4.32). The core and rim compositions of anorthoclase from the Young Rhyolite are near the sanidine-anorthoclase boundary, with compositions ranging from ~Or_{39}-Or_{47} (Fig. 4.33).

Mafic and oxide minerals in the Young Rhyolite were identified through quantitative EPMA spot analyses and include fayalite, magnetite, and zircon (Appendix F). Fayalite averages ~58.0-62.0% Fe and ~3.5-4.0% Mg, with Fo# from ~5.4-6.0%.

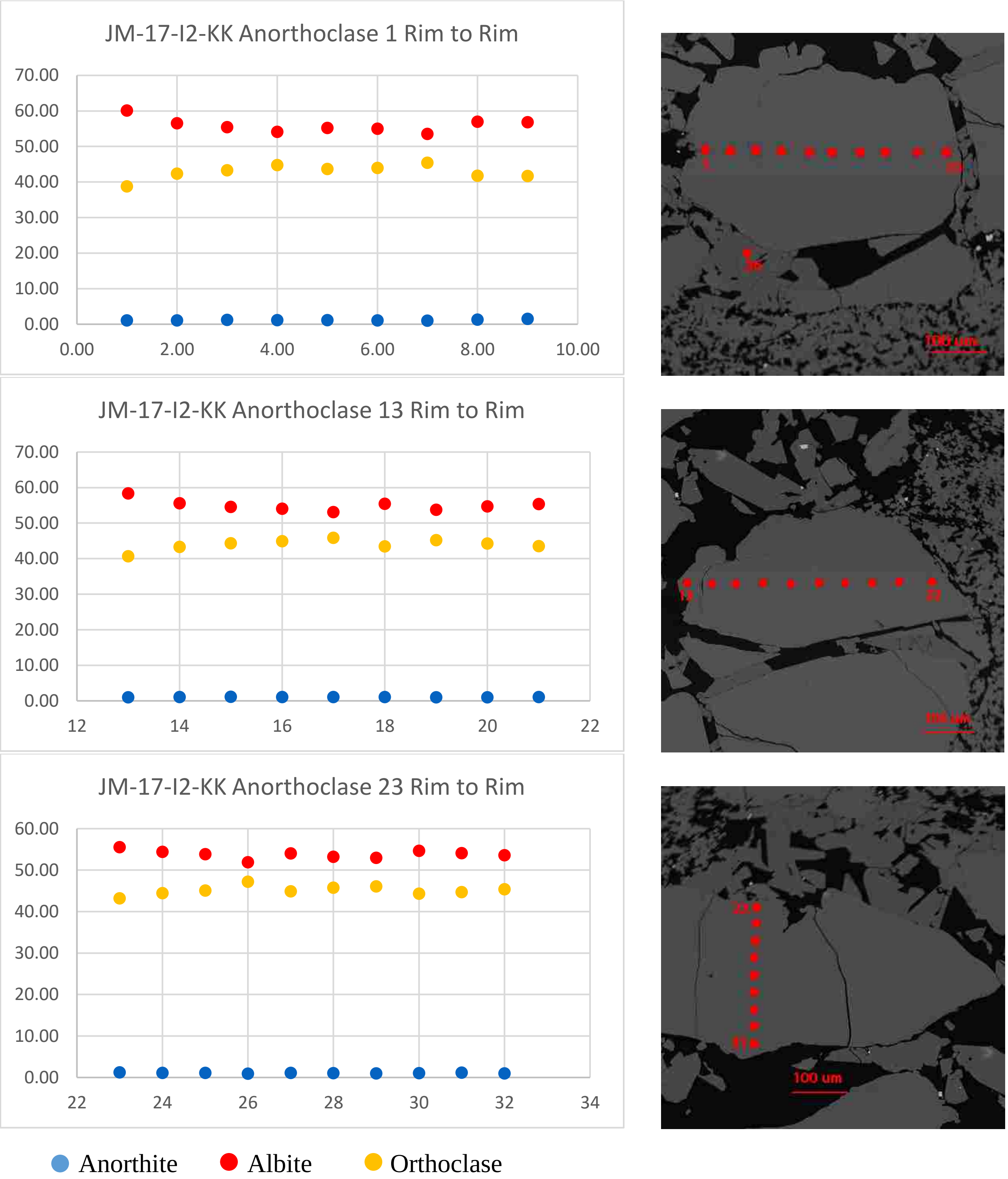

Figure 4.32. Representative EPMA transects across anorthoclase crystals in the Young Rhyolite, along with BSE images of each analyzed crystal with transect plotted in red. Percent Anorthite, Albite, and Orthoclase denoted by symbols.

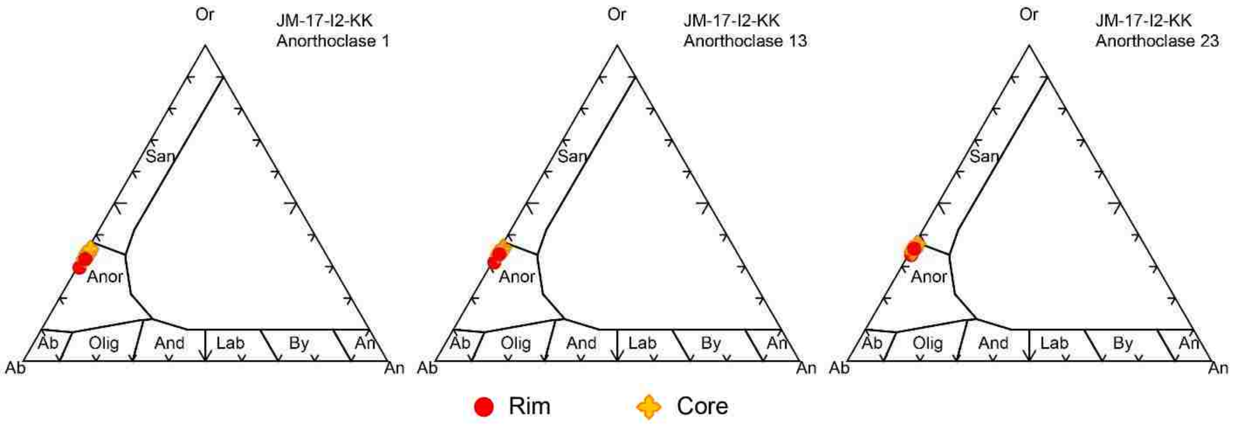

Figure 4.33. Ternary diagrams of anorthoclase from the Young Rhyolite.

CHAPTER 5

DISCUSSION

5.1 Interpretations of ^{40}Ar/^{39}Ar Geochronology

As the ages of these rhyolites have previously been poorly constrained, ^{40}Ar/^{39}Ar ages are reported for all of the units examined in this study in an attempt to determine more accurate and precise constraints on eruptive timing. Previously reported ages were primarily obtained using K/Ar geochronology (Dalrymple et al., 1967; Loeffler et al., 1988), aside from the El Rechuelos units which have been inconsistently dated using ^{40}Ar/^{39}Ar geochronology (Justet, 2003; Kelley et al., 2013). In general, K/Ar ages may be questionable as it is not possible to check for excess argon, argon loss, alteration, or other problems which may affect accuracy (McDougall and Harrison, 1999).

The K/Ar age obtained by Loeffler et al. (1988) on biotite from the Early Rhyolite is 7.54 ± 0.28 Ma, which is indistinguishable at two-sigma uncertainties from the ages determined in this study using ^{40}Ar/^{39}Ar dating. The ^{40}Ar/^{39}Ar spectra suggest the presence of excess argon for both the plagioclase (U-shaped spectrum) and biotite (discordant spectrum) samples from the Early Rhyolite (Figs. 4.01, 4.02). If excess argon is present, it is likely that biotite may have taken in more of the excess argon from the magma than plagioclase, due to its crystal structure and high volatile content, therefore the plagioclase sample is likely to have produced a more accurate age. If the plagioclase contains excess argon, the most conservative approach is to assign a maximum age of 7.10 ± 0.04 Ma (the minimum on the age spectrum) for the Early Rhyolite.

The Intermediate Rhyolite is significantly older than previously thought, as the preferred age obtained from plagioclase during this study is 7.05 ± 0.24 Ma (Fig. 4.03), whereas the previous K/Ar age on “feldspar plus glass” was 5.80 ± 0.20 Ma (Loeffler et al., 1988).

The Pumice Ring Rhyolite yielded an ^{40}Ar/^{39}Ar preferred age of 5.61 ± 0.48 Ma from biotite (Fig. 4.04). The K/Ar age on biotite from Loeffler et al. (1988) was 5.21 ± 0.25 Ma, indistinguishable from the age obtained during this study, given analytical uncertainties. The spectrum on the amphibole from this sample is too discordant for a reliable age to be determined from, thus the biotite age of 5.61 ± 0.48 Ma is considered the most reliable.

The El Rechuelos units have been previously dated at approximately 2.0 Ma, using both K/Ar and ^{40}Ar/^{39}Ar geochronology. Dalrymple et al. (1967) reported a K/Ar age of 2.02 ± 0.06 Ma on obsidian, Loeffler et al. (1988) reported a K/Ar age of 2.01 ± 0.06 Ma on feldspar, Justet (2003) reported ^{40}Ar/^{39}Ar ages of 2.21 ± 0.01 Ma on sanidine and 2.9 ± 0.7 Ma on plagioclase, and Kelley et al. (2013) determined a ^{40}Ar/^{39}Ar age of 2.09 ± 0.02 Ma on an unreported phase. This study has found that the northern El Rechuelos dome has a preferred age of 2.23 ± 0.15 Ma (Fig. 4.06) based on plagioclase analysis, which overlaps previous ages at two-sigma uncertainties. The highly discordant spectra for the central and southern domes yield total gas ages of 1.78 ± 0.07 Ma and 2.97 ± 0.06 Ma, respectively, on a mixture of feldspar and glass (Fig. 4.07, 4.08) and are considered unreliable ages. Thus, based on geochemical and petrographic data indicating these three domes represent the same unit (section 4.1; 4.3), an age of 2.23 + 0.15 Ma is assumed for the three El Rechuelos Rhyolite domes.

This study has determined a plateau age of 1.19 ± 0.01 Ma for the Young Rhyolite based on an anorthoclase analysis (Fig. 4.09). This age generally coincides with the range of ages typically found for the Bandelier Tuff (1.19-1.25 Ma; Spell et al., 1996b; Phillips et al., 2007), however this unit does not share the same petrographic characteristics as typical Bandelier Tuff (section 4.1).

The ages of these seven units suggest that they were produced from at least four separate eruptive episodes (Fig. 5.01). As individual magma systems typically do not persist for more than a few hundred thousand years, the million year-plus spans between these eruptive events suggests that they must have been derived from separate magma batches. Although the Early and Intermediate rhyolites overlap temporally, petrography and geochemistry indicate that these rhyolites are not magmatically related to one another (section 4.1; 4.3), thus they represent eruptions of distinct magmas, bringing the total number of eruptive episodes to five.

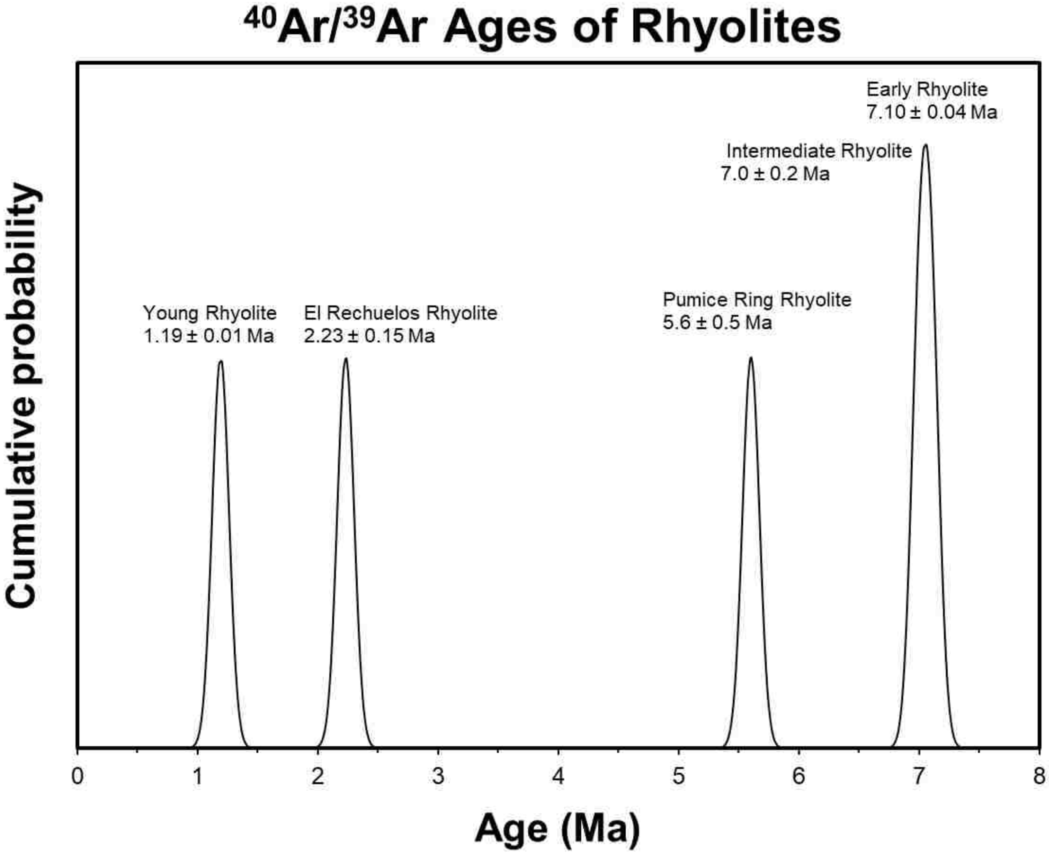

Figure 5.01. Probability distribution plot of ^{40}Ar/^{39}Ar ages for rhyolites in this study. Uncertainty of 0.07 Ma was used to generate plot, in order to better display distinctive episodes. Actual uncertainties indicated for each unit.

5.2 Crystallization History of Units

Petrographic observations indicate that these seven units represent a total of five different magma batches. Observations of distinct textures (or lack thereof), mineral assemblages, and modal abundances indicate major differences among the units (Table 4.01). Disequilibrium features, including embayment, sieve textures, reaction rims, zonation, and resorption are commonly seen in multiple units. These textures indicate open-system processes such as magma mixing, recharge, crustal melting, or underplating, which may cause changes in temperature, volatile content, and/or magma chemistry (Hibbard, 1995; Streck, 2008).

The Early Rhyolite is the most coarsely porphyritic and contains abundant plagioclase phenocrysts. This unit also displays disequilibrium features, especially among plagioclase (reaction rims and sieve texture) and biotite (embayment), suggesting open-system processes in the magma chamber such as magma mixing. Disequilibrium textures such as these have been interpreted by Hibbard (1995) and Streck (2008) to be caused by open-system processes.

Although indistinguishable in age from the Early Rhyolite, the Intermediate Rhyolite likely underwent equilibrium crystallization prior to eruption, as it does not display any significant disequilibrium textures, only very uncommon optical zonation. Interpretations of such textures have been discussed by Hibbard (1995).

The Pumice Ring Rhyolite is very distinct from the other units, in that it contains abundant amphibole and considerably more biotite. This unit displays ample disequilibrium features, indicating that underplating by a more primitive magma and/or magma mixing likely occurred during evolution of the magma prior to eruption. Disequilibrium features, such as resorption and reaction rims, are common among plagioclase, biotite, and quartz crystals in this unit. Hibbard (1995) and Streck (2008) have suggested that disequilibrium features such as these can be attributed to open-system processes such as magma mixing and those associated with underplating (melting and assimilation) during evolution of a magma.

The El Rechuelos units largely appear to have undergone equilibrium crystallization prior to eruption, as they do not display significant disequilibrium features. Features interpreted to be associated with equilibrium crystallization, such as a lack of zonation, have been discussed by Hibbard (1995). These units are nearly identical, comprised primarily of glass and very few phenocrysts. Although uncommon, resorption can be seen in sanidine and quartz, and sparse sieve texture can be seen in plagioclase crystals in the northern unit.

The Young Rhyolite may have been generated with minor input from open-system processes, as embayment can be seen in quartz crystals throughout the sample. Embayment can be attributed to a change in temperature or chemistry associated with potential underplating or magma mixing (Hibbard, 1995; Streck, 2008). This unit is unique in this study, as it contains abundant sanidine, and sparse fayalite crystals.

5.3 Interpretations of Crystal Chemistry

Crystal textures and chemical zonation can help constrain the magmatic histories of igneous units (Loomis, 1982; Tepley et al., 2000; Ginibre et al., 2004; Streck, 2008; Shcherbakov et al., 2011). For example, normal zonation in plagioclase, which is present in multiple units, records chemical changes that suggest typical fractional crystallization. Reverse zonation, embayment, sieve textures, and reaction rims indicate open-system processes, including changes in temperature, volatile content, and/or melt composition, which can be caused by such processes as magma mixing, recharge, crustal melting, or underplating (Hibbard, 1995; Streck, 2008).

Instances in which major compositional changes (i.e. reverse zoning; rimward increase of An content in plagioclase) occur in conjunction with dissolution textures are likely caused by magma recharge and mixing, as concluded in numerous studies, such as Tepley et al. (2000), Ginibre et al. (2004), and Shcherbakov et al. (2011). Alternatively, smaller changes, such as oscillatory zonation, are interpreted to be associated with convection occurring during fractional crystallization and crystal settling (Loomis, 1982; L'Heuruex and Fowler, 1994). Normal zonation, which records decreases in An content from core to rim, is typically interpreted to be characteristic of magmas following the liquid line of descent for cooling and fractional crystallization (Streck, 2008).

Based on electron microprobe analyses, there are two populations of plagioclase in the Early Rhyolite; unzoned andesine and predominantly unzoned oligoclase. Although weak normal zonation is present in some oligoclase crystals, it is not common. The two distinct plagioclase populations and lack of zonation among the andesine and some of the oligoclase suggest interaction of a less evolved magma with the rhyolitic magma. It is likely that the more sodic plagioclase began crystallizing from a rhyolitic magma, as fractional crystallization was occurring so weak zonation developed in some, then a more mafic magma was intruded into the chamber, transferring some of the more calcic plagioclase into the rhyolitic magma. As mafic rejuvenation has been suggested as a trigger for eruptions (Anderson, 1976; Blake, 1981; Pallister et al., 1992), this phenomenon may have triggered the eruption of the Early Rhyolite, allowing little time for reverse zoned rims to form on the more sodic plagioclase. Reaction rims and sieve texture on plagioclase, and embayment and intergrowth of biotite indicate open-system processes during crystallization. Together, these characteristics indicate typical fractional crystallization of the magma, combined with an increase in temperature and possible recharge causing resorption and formation of reaction rims.

Pumice Ring Rhyolite plagioclase displays oscillatory and patchy normal zonation (Fig. 4.26). Plagioclase in this unit display two episodes of normal zonation, having cores normally zoned from An_{31}-An_{53}, and rims normally zoned from An_{36}-An_{51}. Normal zonation can also be seen within biotite (Fig. 4.28), recorded by a decrease in Mg from core to rim. Furthermore, petrographic textures, including resorption, sieve texture, and reaction rims also indicate open-system processes occurred concurrently with crystallization, prior to eruption of this rhyolite. This suggests that fractional crystallization began, then there was an episode of mafic rejuvenation causing resorption and recrystallization, then fractional crystallization continued.

No evidence of zonation is seen in plagioclase or potassium feldspars from the Intermediate Rhyolite (Fig. 4.24), El Rechuelos Rhyolite (Fig. 4.30), or Young Rhyolite (Fig. 4.32). Furthermore, none of these units display notable disequilibrium features, suggesting that these units each underwent equilibrium crystallization prior to eruption.

5.4 Interpretations of Whole Rock Geochemistry

Although all seven units plot as rhyolite on the Le Bas et al. (1986) classification diagram, they are geochemically very distinct. The data suggest that these seven units were generated from five distinct magma batches, and only the three ~2 Ma units are geochemically related to one another. The three units dated at ~2 Ma were apparently generated from the same magma system, as evidenced by their nearly identical major and trace element geochemistry and age (Fig. 4.16-4.21).

Major element compositions generally show four distinct clusters of data among the seven units, with only the Intermediate Rhyolite (7.05 ± 0.24 Ma) and the El Rechuelos Rhyolite units (2.23 ± 0.15 Ma) clustering together (Fig. 4.16). Despite the Intermediate and El Rechuelos units appearing similar on major element plots, these units are likely derived from separate magma batches, based on the large amount of time (over 4 Ma) between the eruptions of the units (Fig. 5.01). Trends among some of the major elements (Al_2O_3, CaO, TiO_2, and MgO decrease and K_2O increases with increasing SiO_2) generally suggest that the lavas are becoming more evolved with decreasing age; it is unlikely that these trends are due to fractional crystallization, given the range of eruptive ages. The Pumice Ring Rhyolite does not follow this trend, indicating that it is distinct from the other units in this study. Additionally, Na_2O, P_2O_5, and FeO do not follow any trends typical of magma evolution, suggesting that the seven units were produced from separate magma batches.

Trace element data additionally show some general trends that suggest potential magma differentiation among some of the units, and once again set the Pumice Ring Rhyolite apart from the other units (Fig. 4.17-4.18). Plots of Ce, Nd, Lu, Yb, Y, Ba, and Zn show an increase in concentration from the Pumice Ring Rhyolite to the Early Rhyolite, then a decrease from the Early Rhyolite to the El Rechuelos Rhyolite, then an increase from the El Rechuelos Rhyolite to the Young Rhyolite. Eu shows an increase in concentration from the Pumice Ring Rhyolite to the Early Rhyolite, then a decrease in content, while U shows an increase from the Pumice Ring Rhyolite to the El Rechuelos Rhyolite then a decrease. There is a general increase of Ta, Th, and Rb, and a general decrease of Sr. Plots of immobile, incompatible trace element ratios do not follow any linear trends, and there is a large variability in ratios between units. The data shown in these plots set the less evolved Pumice Ring Rhyolite apart and suggest a change in evolution with the trend changes among the remaining units; increasing concentrations of incompatible elements from the Early to the El Rechuelos rhyolites could be interpreted as a fractional crystallization trend, however the ages of the units are not compatible with this model. Additionally, the Young Rhyolite does not consistently follow this trend, setting it apart from the others as well.

Although there are some correlations among whole rock geochemical trends with decreasing age that appear similar to those of simple fractional crystallization, this is likely fortuitous, as these trends are not consistently seen among all major and trace element diagrams, agreeing with the interpretations of Loeffler et al. (1988). If the seven units were sourced from the same evolving magma batch, the data should show stronger trends and correlations among oxides on the major element diagrams; decreasing compatible element concentrations and increasing incompatible element concentrations with increasing Nb content on trace element diagrams; and linear trends among plots of immobile, incompatible trace element ratios. Additionally, the ages of these units (Fig. 5.01) make fractional crystallization from the same evolving magma batch impossible, as single magma batches typically only persist for a few hundred thousand years (Bachmann and Huber, 2016), significantly less time than the million year-plus spans between these units.

Rare earth element plots show that relative REE concentrations vary among the units (Fig. 4.20), which can suggest fractionation (or lack thereof) of certain minerals prior to eruption (Pearce et al., 1984; Rollinson, 1993; Liu et al., 2014). The Young Rhyolite is the most evolved of the seven units, as it contains the highest concentration of REEs, and largest negative Eu anomaly (depletion), indicative of extensive feldspar fractionation. The El Rechuelos Rhyolite has the lowest LREE concentrations (La/Yb = ~6.08), indicating LREE depletion relative to the other units in this study, and suggests fractionation of accessory phases, such as monazite and allanite. The Pumice Ring Rhyolite is enriched in LREEs relative to HREEs (La/Yb = ~15.33-

16.67), which suggests extensive fractionation of hornblende prior to eruption. Interpretations of REE concentrations relative to feldspar, hornblende, and accessory mineral fractionation have been discussed by Pearce et al. (1984) and Rollinson (1993; Chapter 4).

On the multi-element variation diagram (Fig. 4.21), the strong negative anomalies of Ba, Sr and Eu seen for the El Rechuelos and Young rhyolites suggest extensive feldspar fractionation prior to the eruptions of these units. The Intermediate Rhyolite also likely underwent pre-eruptive feldspar fractionation, based on negative anomalies of Ba, Sr, and Eu, but not nearly as much as the El Rechuelos and Young rhyolites. Conversely, the positive anomaly (enrichment) in Ba and small negative anomalies in Sr and Eu for the Early and Pumice Ring rhyolites suggest very minimal feldspar fractionation prior to the eruptions of these units. Interpretations of such anomalies have been discussed by Rollinson (1993; Chapter 4) and Liu et al. (2014).

The Pumice Ring Rhyolite is unique from the other rhyolites studied. It is the least evolved of the seven units, yet falls in the middle of the eruptive period. This unit also has a volcanic arc signature and is characteristic of an A_2 type granitoid, differing from the other units in this study (Fig. 5.02-5.03); the other units plot as within plate (continental; A type) granitoids that are A_1 type (Pearce et al., 1984; Eby, 1992). A_1 granitoids are derived from rift, plume, or hotspot settings, while A_2 granitoids are derived from post-collisional, post-orogenic, or anorogenic settings (Eby, 1992). These data indicate that the Pumice Ring unit likely should not be classified with the other rhyolites of the Polvadera Group, but rather with the Tschicoma Formation, as suggested by Loeffler et al. (1988).

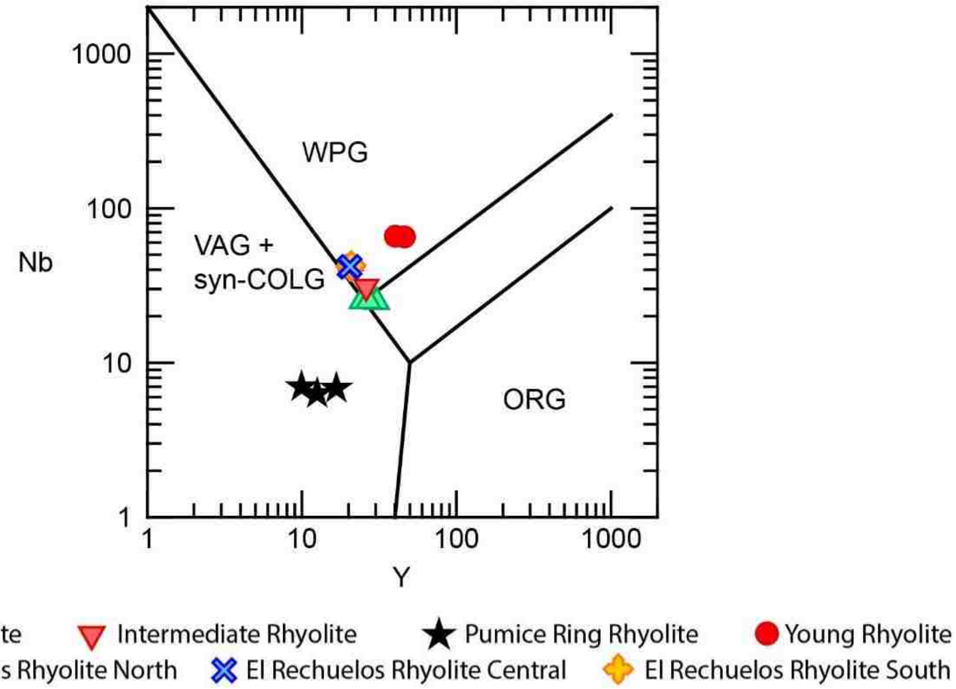

Figure 5.02. Nb-Y discriminant diagram for syn-collision granites (syn-COLG), volcanic arc granites (VAG), within plate granites (WPG) and ocean ridge granites (ORG). After Pearce et al. (1984).

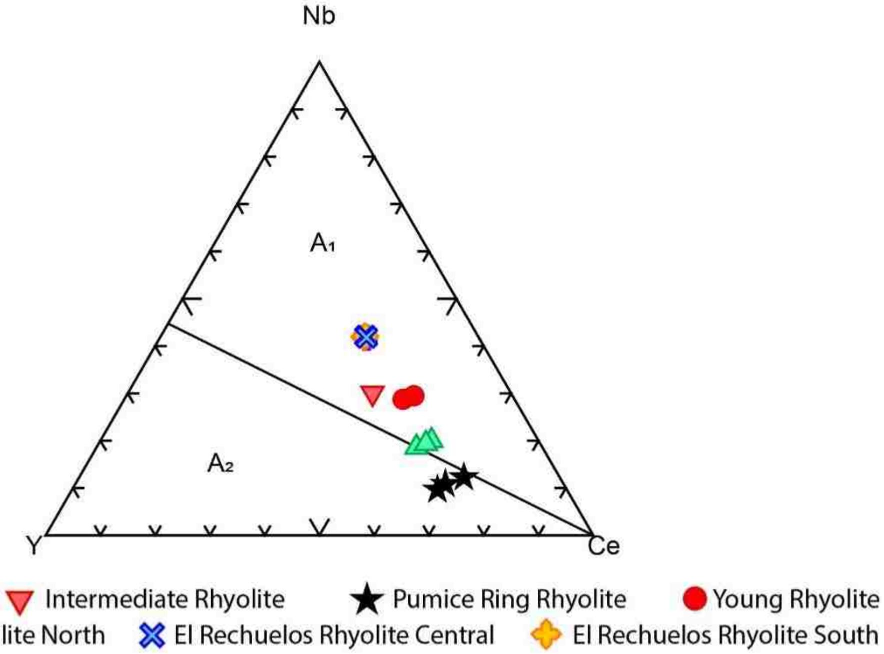

Figure 5.03. Differentiation between A_1 and A_2 type granitoids. Dashed line corresponds to Y/Nb ratio of 1.2. After Eby (1992).

Due to similar age, the Young Rhyolite (1.19 ± 0.01 Ma) has been compared with the Bandelier Tuff (1.19-1.25 Ma; Spell et al., 1996b; Phillips et al., 2007). Trace element geochemical data for the Upper Bandelier Tuff (UBT; Balsley, 1988) was plotted along with the Young Rhyolite data from this study. In addition to sharing a similar age, these units appear to be geochemically similar (Fig. 5.02), except for the immobile, incompatible trace element ratios (Fig. 5.03), where the Young Rhyolite deviates from the Bandelier Tuff for plots of Y/Yb and Th/Yb. On a normalized REE diagram and normalized multi-element variation diagram, the Young Rhyolite and the Bandelier Tuff share very similar patterns, and the Young Rhyolite is within the range of values for the Bandelier Tuff (Fig. 5.06). Although the Young Rhyolite shares some similarities with the Bandelier Tuff, such as containing potassium feldspar (anorthoclase) with nearly identical composition (Crow et al., 1978), the Young Rhyolite does not have petrographic features typical of a tuff (section 4.1). The Young Rhyolite also contains fayalite, a characteristic common to some phases of Bandelier Tuff. These data suggest that the Young Rhyolite is related to the Bandelier system, although it may represent a specific phase or sub-unit within the Bandelier Tuff. Warshaw and Smith (1988) have found that the phases of Bandelier Tuff containing fayalite were generated under lower oxygen fugacity conditions than phases that do not contain fayalite, so it is possible that differences in oxygen fugacity conditions during the eruptions of the different phases could explain the variation seen between the Bandelier Tuff and the Young Rhyolite. Alternatively, the Young Rhyolite may be a previously overlooked and unmapped post-collapse, extra-caldera rhyolite, although this is less likely. More research is required to sufficiently test these hypotheses.

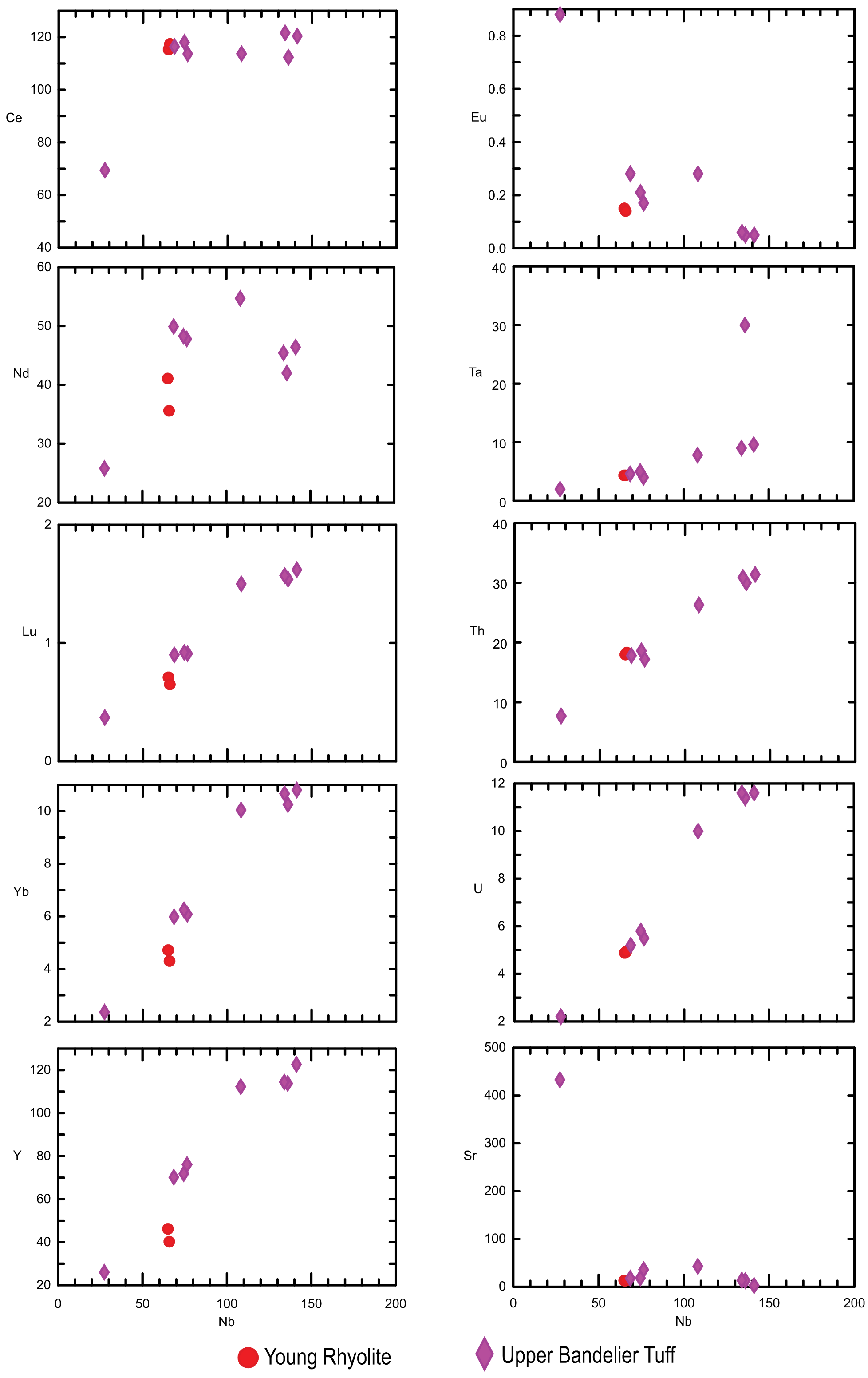

Figure 5.04. Trace elements versus Nb. Young Rhyolite trace elements measured by ICP-MS, Upper Bandelier Tuff trace elements measured by XRF and INAA. Trace elements in ppm. Two-sigma uncertainty is smaller than symbols shown. Upper Bandelier Tuff data from Balsley (1988).

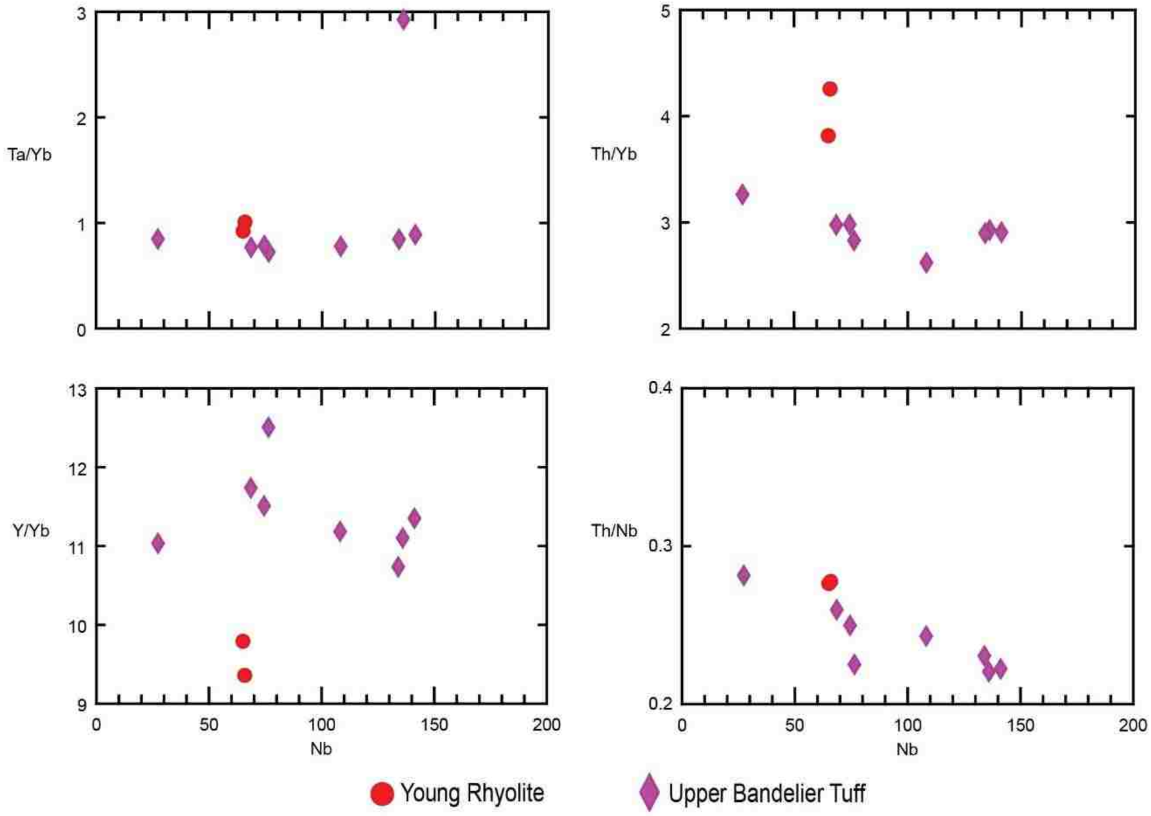

Figure 5.05. Ratios of incompatible trace elements versus Nb. Trace elements in ppm. Two-sigma uncertainty is smaller than symbols shown. Upper Bandelier Tuff data from Balsley (1988).

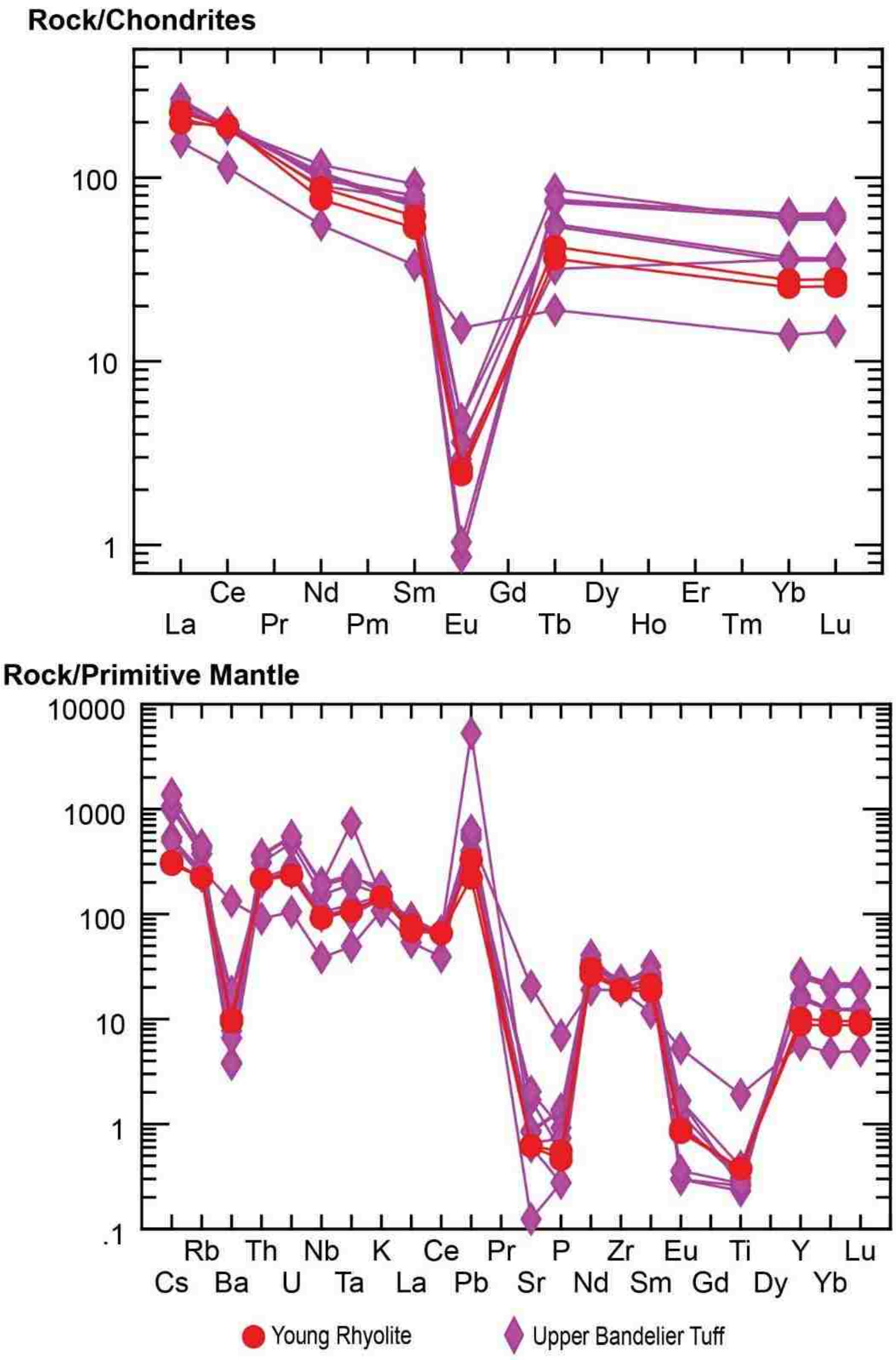

Figure 5.06. Normalized rare earth element diagram and normalized multi-element variation diagram. Upper Bandelier Tuff data from Balsley (1988). Chondrite normalizing values and primitive mantle values from Sun and McDonough (1989).

5.5 Petrogenetic Models

Based on Sr and Nd isotopic data, Loeffler et al. (1988) suggested that the Neogene rhyolites of the northern Jemez may have been derived from parent magmas that produced temporally similar basalt flows in the area, in combination with minor assimilation of lower crust. Other models were tested, and ruled out, in an attempt to constrain the petrogenesis of the rhyolites. These include simple fractional crystallization of a single magma with upper crustal assimilation (not consistent with Nd isotopic ratios), and direct crustal anatexis (not consistent with Sr and Nd isotopic ratios) (Loeffler et al., 1988). As the Sr and Nd isotopic ratios were considered consistent with generation of the rhyolites from a mantle-derived magma, by fractional crystallization and minor lower crustal assimilation, Loeffler et al. (1988) tested this model using the Lobato Basalt as a parental composition, due to its temporal similarity to the rhyolites. Using models and equations from DePaolo (1981) and Farmer and DePaolo (1983), Loeffler et al. (1988) showed that 5.1% of lower crustal assimilation, with composition ^{87}Sr/^{86}Sr= 0.7057, ^{143}Nd/^{144}Nd= 0.511867 (εNd= -15), 350 ppm Sr, and 50 ppm Nd, with the Lobato Basalt allowed for production of a lava isotopically similar to the oldest unit, and that less than 2% of lower crustal assimilation, with composition ^{87}Sr/^{86}Sr 0.7060, ^{143}Nd/^{144}Nd= 0.511867 (εNd= -15), 350 ppm Sr, and 40 ppm Nd, allowed for production of a lava isotopically similar to the El Rechuelos Rhyolite. Loeffler et al. (1988) suggested that the El Alto Basalt, that lacked Nd data at the time, be investigated as a more suitable parental composition for the El Rechuelos Rhyolite, based on their temporal similarity with one another. Loeffler et al. (1988) further hypothesized that the rhyolites were likely fractionated in lower-crustal magma chambers, but also proposed a more complex alternative; the parental magmas of the rhyolites were themselves contaminated by lower crust before they were fractionally crystallized in an upper crustal magma chamber, without significant assimilation.

Based on this previous work, trace element geochemical modeling of fractional crystallization was completed using the geochemical data obtained in this study for the rhyolites, and that from Wolff et al. (2005) for the Lobato Basalt and El Alto Basalt. Loeffler et al. (1988) mentioned fractionation modeling using observed phenocryst phases, but did not refer to any data or previous studies, thus this modeling is being newly introduced here. Initial trace element geochemical modeling suggests that the Lobato Basalt may be a suitable choice as a parental composition for the Early and Intermediate rhyolites, while the El Alto Basalt may be a suitable choice as a parental composition for the El Rechuelos and Young rhyolites. These models also made it increasingly more clear that the Pumice Ring Rhyolite is not related to any of the other rhyolites, or the Lobato or El Alto basalts.

Detailed trace element geochemical modeling of fractional crystallization was done using the equation for Rayleigh fractionation:

$$C_L/C_0 = F^{(D-1)}$$

where C_L is the concentration of a trace element in the melt, C_0 equals the initial concentration of a trace element in the primary magma, F equals the fraction of melt remaining, and D equals the bulk partition coefficient for the fractionating mineral assemblage (Rollinson, 1993). This modeling was done in a step-wise fashion, working from the selected basalt composition to an intermediate composition, then to a rhyolitic composition. Basalt data points from the Lobato and El Alto basalts were selected after considering the data from Wolff et al. (2005), and selecting two end member points and one mid-range point for each unit to represent a range of potential starting compositions. Common mineral assemblages were used for the basalts (plagioclase, orthopyroxene, clinopyroxene, olivine, and magnetite) and intermediate compositions (plagioclase, hornblende, orthopyroxene, clinopyroxene, olivine, and magnetite), while mineral assemblages for the rhyolites were determined through petrography. Reasonable modal abundances were estimated for the basalts and intermediate compositions, while measured modal abundances from point counting were used for the rhyolites. Representative partition coefficients suitable for each composition were sourced from the GERM website (http://earthref.org/KDD/). Using these parameters, modeling was done in a step-wise fashion. The original basalt compositions were modeled to 40% fractional crystallization, using reasonable mineral assemblages, modal abundances, and partition coefficients for basalt. Once modeling reached 40% fractional crystallization of basalt, mineral assemblages, modal abundances, and partition coefficients were adjusted to reflect intermediate compositions, and modeled again to 40% fractional crystallization of an intermediate composition. Once 40% fractional crystallization of the intermediate composition was reached, reasonable partition coefficients, observed mineral assemblages, and measured modal abundances were substituted in to represent rhyolitic compositions, in an attempt to generate models that allowed for production of rhyolites matching those measured in this study. Modal abundances and partition coefficients were adjusted within reasonable bounds at each stage, but the modeling did not generate rhyolites similar to those measured in this study. Fractional crystallization modeling details are contained in Appendix H.

This modeling of fractional crystallization shows that the basalts hypothesized by Loeffler et al. (1988) to represent the parental compositions of the rhyolites may not be suitable choices (Fig. 5.07-5.08). As stated by Loeffler et al. (1988), there is a lack of cogenetic intermediate rocks, which makes it difficult to constrain the detailed evolution of the rhyolites, as there are many variables to consider, including potential parental compositions, mineral assemblages, and mineral/melt partition coefficients. The model generated in this study for fractional crystallization does not demonstrate that any of these rhyolites were produced from the basalts selected as parental compositions (Fig. 5.07-5.08). The Lobato Basalt does not produce a fractional crystallization trend that generates rhyolitic lavas similar to the Early Rhyolite or Intermediate Rhyolite, and the El Alto Basalt does not generate a fractional crystallization trend that allows for the production of the El Rechuelos Rhyolite or Young Rhyolite. Furthermore, this modeling indicates that none of the rhyolites are related to one another by simple fractional crystallization.

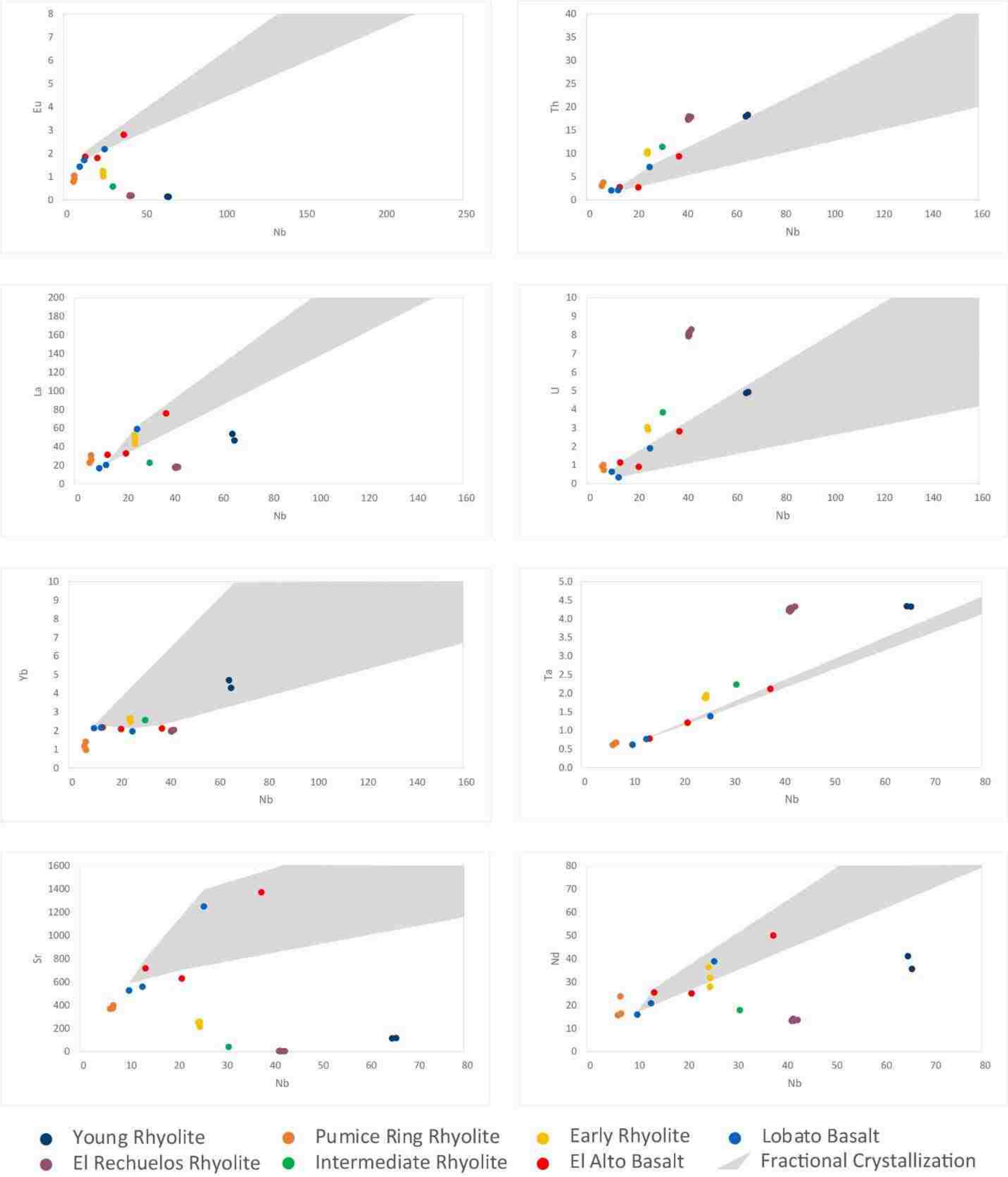

Figure 5.07. Fractional crystallization trends of selected trace elements versus Nb. Grey area indicates envelope of calculated fractional crystallization trends.

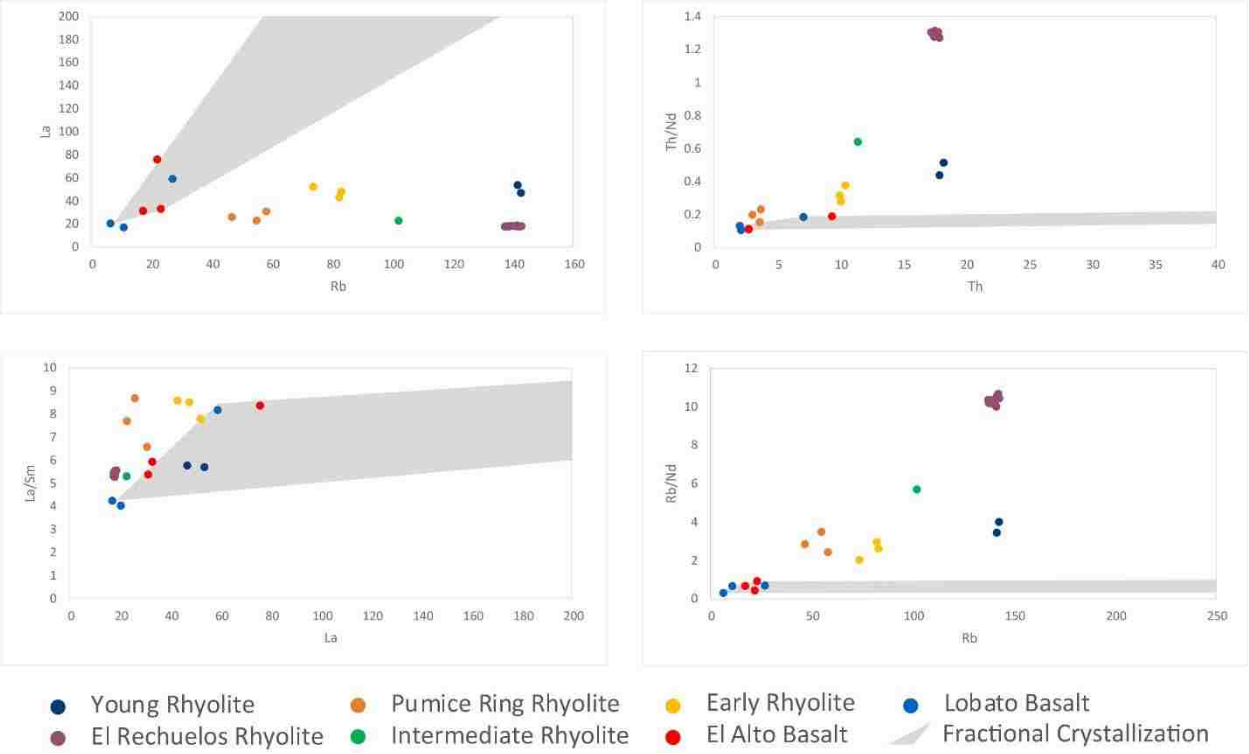

Figure 5.08. Fractional crystallization trends of selected trace elements and trace element ratios. Grey area indicates envelope of calculated fractional crystallization trends.

As trace-element modeling suggested that these rhyolites are not related through simple fractional crystallization, other models were proposed and preliminarily tested. Plots of various incompatible element ratios were plotted for the rhyolites, along with the Lobato and El Alto basalts (Wolff et al., 2005), in an attempt to constrain the petrogenesis of the units in this study. Nb/La versus Th/La was plotted to investigate crustal input (Fig. 5.09a; Liu et al., 2014). Nb/La versus Nb/U was plotted to distinguish crustal input from mantle input (Fig. 5.09b; Tian et al., 2010). La/Sm versus Gd/Yb was plotted because high Gd/Yb ratios are associated with deeper sourcing of melt, while variations in La/Sm ratios suggest either crustal contamination, or melting of an enriched source (Fig. 5.09c; Jowitt and Ernst, 2013; Kingsbury, 2017). Nb/Ta versus Nb was plotted to help constrain a crustal or mantle source (Fig. 5.09d; Green, 1995).

Ce/Yb versus Ce was plotted to discern possible partial melting from fractional crystallization (Fig. 5.10; Liu et al., 2014); Lobato intermediate composition rocks were added to this plot for comparison (Singer and Kudo, 1986).

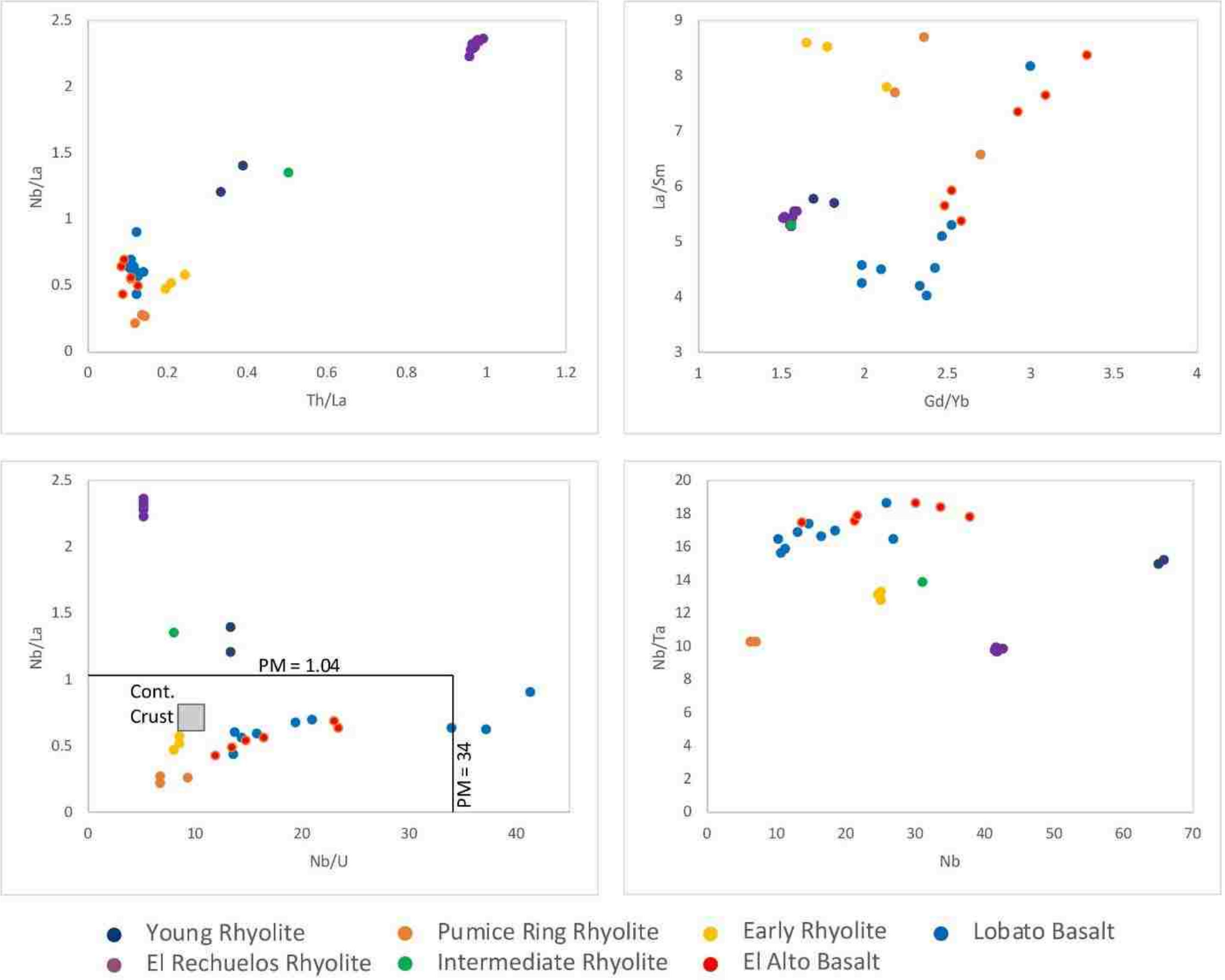

Figure 5.09. Geochemical trace element ratios of rhyolites of this study with Lobato and El Alto basalts. Basalt data from Wolff et al. (2005). a) Nb/La versus Th/La, after Liu et al. (2014). b) Nb/La versus Nb/U, after Tian et al. (2010). Primitive mantle (PM) values from Sun and McDonough (1989), continental crust values from Rudnick and Fountain (1995). c) La/Sm versus Gd/Yb, after Jowitt and Ernst (2013) and Kingsbury et al. (2017). d) Nb/Ta versus Nb, after Green (1995).

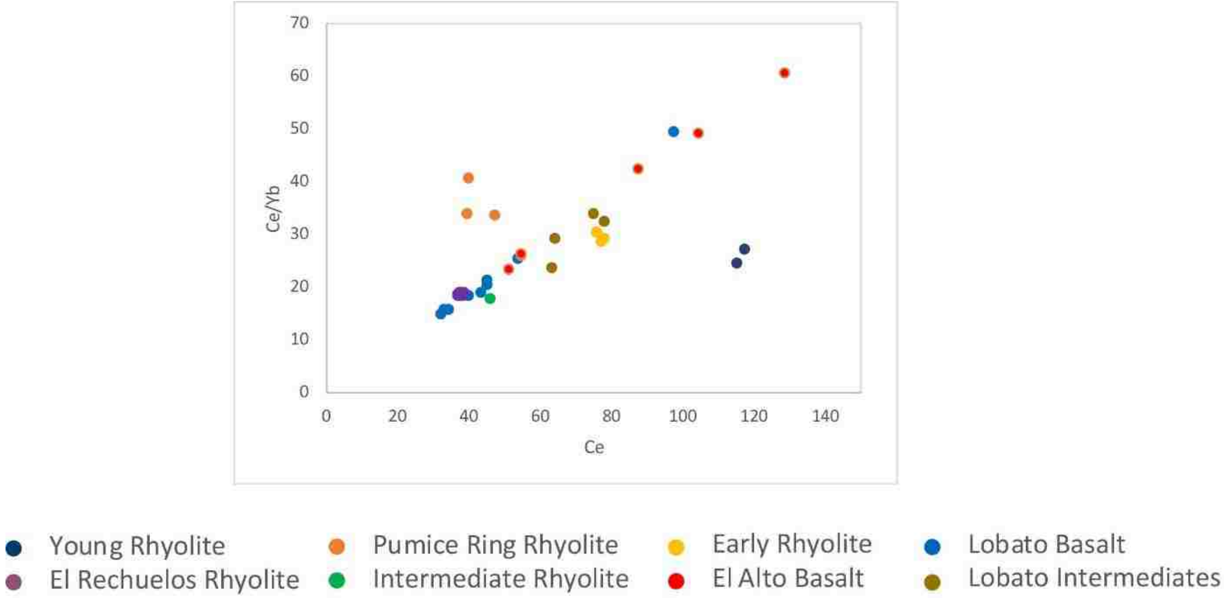

Figure 5.10. Ce/Yb versus Ce, after Liu et al. (2014). Lobato Intermediate compositions from Singer and Kudo (1986).

These plots indicate that the rhyolites investigated in this study have distinct petrogenetic histories, due to their differences in incompatible trace element geochemistry. It is likely that the Early Rhyolite is derived from partial melting and assimilation of crust, as the incompatible element ratios have a signature similar to continental crust, including high La/Sm, low Nb/La, Nb/U, and Th/La. This unit also falls along the trend for partial melting on the plot of Ce/Yb versus Ce. The Pumice Ring Rhyolite also yields incompatible element ratios similar to continental crust, suggesting partial melting, however, this unit does not follow the same trend for partial melting as the Early Rhyolite. Additionally, this unit has a volcanic-arc signature, setting it apart from the other units; it is possible that this unit is derived from a different source, which can account for the arc signature and unique differentiation trend. The Intermediate Rhyolite and the El Rechuelos Rhyolite have significantly lower amounts of crustal input, but still fall on the trend of partial melting, suggesting that these units may have been produced by smaller amounts of partial melting than the units with more crustal input. It is possible that the partial melting that generated these units is caused by underplating by mafic sills associated with the Yavapai-Mazatzal suture zone beneath the Jemez lineament (Magnani et al., 2005). These plots suggest that the Young Rhyolite does not have a major crustal component and may be produced from fractional crystallization of a mantle-derived source, but this source is not the Lobato or El Alto basalts, as demonstrated throughout this section. The compositions of the Lobato and El Alto basalts were added to the normalized REE and normalized multi-element variation diagrams, to compare trace element concentrations, further indicating that the rhyolites are not related to one another, nor are they related to the Lobato Basalt or the El Alto Basalt, based on the vast differences among trace element concentrations (Fig. 5.11).

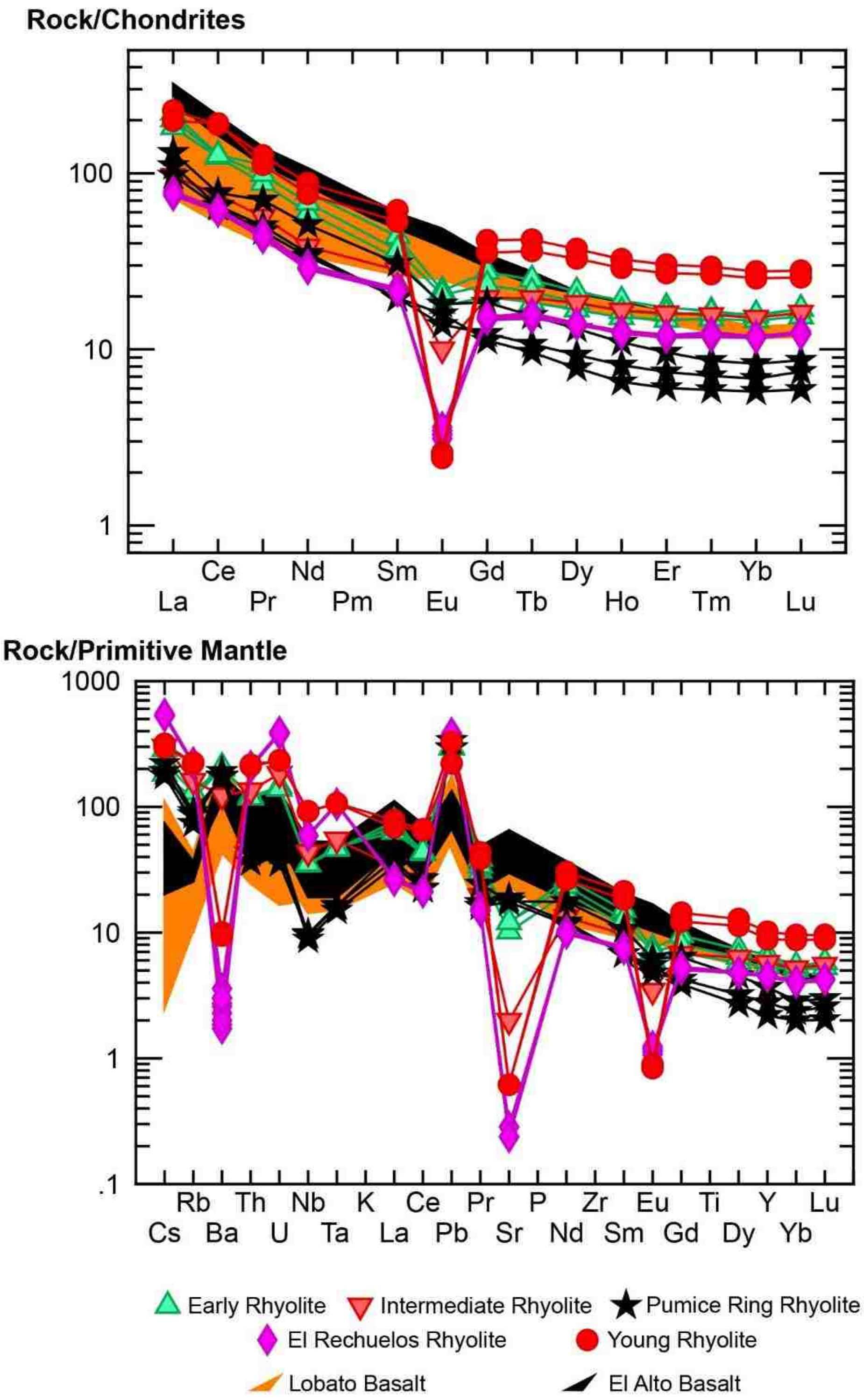

Figure 5.11. Normalized rare earth element diagram and normalized multi-element variation diagram for rhyolites of this study the Lobato and El Alto basalts. Chondrite normalizing values and primitive mantle values from Sun and McDonough (1989).

CHAPTER 6

CONCLUSIONS

The El Rechuelos Rhyolite has not previously been studied in great detail, and there has been disagreement on its classification and relationship to the larger Valles caldera system. This study aimed to resolve this uncertainty, by investigating these six units, in addition to a seventh unit sampled during field work. Methods included updated ^{40}Ar/^{39}Ar geochronology, whole-rock geochemistry, petrography, and electron microprobe analysis. Based on the results of this study, it is concluded that these seven rhyolitic units were erupted during five separate eruptive episodes, each generated from a distinct magma batch. Four of these episodes were pre-caldera events, while the fifth was a syn-caldera event. The pre-caldera events include the eruption of the Early Rhyolite (7.10 ± 0.04 Ma), Intermediate Rhyolite (7.05 ± 0.24 Ma), Pumice Ring Rhyolite (5.61 ± 0.48 Ma), and the El Rechuelos Rhyolite (2.23 ± 0.15 Ma). The syn-caldera event consists of the eruption of the Young Rhyolite (1.19 ± 0.01 Ma), which is most likely a phase of the Bandelier Tuff. New ^{40}Ar/^{39}Ar ages, whole-rock geochemistry, and petrographic observations indicate that only three of the seven units are related to one another, and that only these three rhyolites (dated 2.23 ± 0.15 Ma) should retain the name of El Rechuelos Rhyolite, consistent with the conclusions of Loeffler et al. (1988). Geochemical modeling and analysis suggests that the Young Rhyolite may be a product of fractional crystallization, but the other four units are likely products of varying degrees of partial melting and crustal assimilation, however, further investigation is required to fully constrain the petrogenesis of these rhyolites.

APPENDIX A. SAMPLE LOCATIONS AND ANALYTICAL METHODS USED

Sample Name	Unit	Latitude	Longitude	Thin Section Petrography	Point Count	EPMA	XRF	ICP-MS	^{40}Ar/^{39}Ar
JM-17-O1-KK	Early Rhyolite	N 36°02'411"	W 106°29'084"	X	X		X	X	
JM-17-O2-KK	Early Rhyolite	N 36°02'127"	W 106°29'267"	X		X	X	X	X
JM-17-O3-KK	Early Rhyolite	N 36°01'959"	W 106°29'057"				X	X	
JM-18-M2-KK	Intermediate Rhyolite	N 36°01'292"	W 106°28'465"	X	X	X	X	X	X
JM-17-PR3-KK	Pumice Ring Rhyolite	N 36°05'660"	W 106°24'305"	X	X		X	X	
JM-17-PR4-KK	Pumice Ring Rhyolite	N 36°05'707"	W 106°24'355"				X	X	
JM-17-PR6-KK	Pumice Ring Rhyolite	N 36°05'660"	W 106°24'305"	X		X	X	X	X
JM-17-ERN1-KK	El Rechuelos Rhyolite North	N 36°04'879"	W 106°25'371"	X	X		X	X	
JM-17-ERN3-KK	El Rechuelos Rhyolite North	N 36°04'783"	W 106°25'253"	X		X	X	X	X
JM-17-ERN4-KK	El Rechuelos Rhyolite North	N 36°04'739"	W 106°25'213"				X	X	
JM-17-ERC3-KK	El Rechuelos Rhyolite Central	N 36°03'978"	W 106°25'432"				X	X	
JM-17-ERC4-KK	El Rechuelos Rhyolite Central	N 36°03'905"	W 106°25'339"				X	X	
JM-17-ERC5-KK	El Rechuelos Rhyolite Central	N 36°03'972"	W 106°25'550"	X	X	X	X	X	X
JM-17-ERC6-KK	El Rechuelos Rhyolite Central	N 36°03'972"	W 106°25'550"	X			X	X	
JM-17-ERS2-KK	El Rechuelos Rhyolite South	N 36°02'893"	W 106°25'368"	X	X	X	X	X	X
JM-17-ERS3-KK	El Rechuelos Rhyolite South	N 36°02'859"	W 106°25'368"				X	X	
JM-17-ERS4-KK	El Rechuelos Rhyolite South	N 36°02'925"	W 106°25'389"	X			X	X	
JM-17-I1-KK	Young Rhyolite	N 36°01'696"	W 106°28'639"	X	X		X	X	
JM-17-I2-KK	Young Rhyolite	N 36°01'816"	W 106°28'783"	X		X	X	X	X

APPENDIX B. ^{40}AR/^{39}AR GEOCHRONOLOGY DATA

JM-17-O2-KK Plagioclase

Weight: 34.59 mg J = 0.00111 ± 0.39%

4 amu discrimination = 1.0170 ± 0.15%, $^{40/39}$K = 0.0232 ± 18.12%, $^{36/37}$Ca = 0.000263 ± 1.15%, $^{39/37}$Ca = 0.000702 ± 0.49%

Step	T (C)	t (min.)	^{36}Ar	^{37}Ar	^{38}Ar	^{39}Ar	^{40}Ar	%^{40}Ar*	% ^{39}Ar rlsd	Ca/K	^{40}Ar*/^{39}ArK	Age (Ma)	1s.d.
1	660	12	0.473	5.079	0.302	11.818	182.389	25.5	7.7	2.017871003	3.841827	7.68	0.16
2	740	12	0.130	10.588	0.228	14.598	93.451	64.6	9.5	3.406933993	3.925581	7.84	0.05
3	820	12	0.114	20.376	0.267	17.450	94.433	71.9	11.3	5.488354737	3.695401	7.39	0.06
4	900	12	0.092	31.067	0.279	17.586	85.209	78.7	11.4	8.310443777	3.604148	7.20	0.07
5	980	12	0.080	41.517	0.310	18.847	84.804	84.2	12.2	10.36926157	3.553511	7.10	0.04
6	1050	12	0.069	43.055	0.296	18.362	84.318	88.5	11.9	11.03967488	3.811236	7.62	0.06
7	1120	12	0.062	40.386	0.276	15.907	71.915	90.9	10.3	11.95683901	3.758582	7.51	0.07
8	1190	12	0.056	31.372	0.205	12.253	59.089	89.5	7.9	12.05832536	3.858377	7.71	0.08
9	1250	12	0.059	21.340	0.159	8.686	52.867	82.9	5.6	11.56903649	4.445833	8.88	0.17
10	1400	12	0.098	36.678	0.397	18.626	256.760	94.4	12.1	9.266257676	12.670889	25.20	0.12
							Cumulative %^{39}Ar rlsd =		100.0		Total gas age =	9.70	0.05

note: isotope beams in mV, rlsd = released, error in age includes J error, all errors 1 sigma

(^{36}Ar through ^{40}Ar are measured beam intensities, corrected for decay for the age calculations)

No plateau

No isochron

Wtd mean age = 7.44 0.02

Preffered age = 7.51 0.26

(steps 1-8)

APPENDIX B. ^{40}AR/^{39}AR GEOCHRONOLOGY DATA (CONTINUED)

JM-17-O2-KK Biotite

Weight: 37.12 mg J = 0.001112 ± 0.46%

4 amu discrimination = 1.0170 ± 0.15%, $^{40/39}$K = 0.0232 ± 18.12%, $^{36/37}$Ca = 0.000263 ± 1.15%, $^{39/37}$Ca = 0.000702 ± 0.49%

Step	**T (C)**	**t (min.)**	**^{36}Ar**	**^{37}Ar**	**^{38}Ar**	**^{39}Ar**	**^{40}Ar**	**%^{40}Ar***	**% ^{39}Ar rlsd**	**Ca/K**	**^{40}Ar*/^{39}ArK**	**Age (Ma)**	**1s.d.**
1	600	12	42.195	1.300	10.609	61.603	13268.05	7.6	3.5	0.106846564	16.520202	32.84	2.86
2	630	12	2.242	0.417	1.062	21.733	701.105	7.0	1.2	0.097148066	2.277403	4.56	0.20
3	710	12	3.740	1.101	2.945	73.359	1377.53	21.2	4.2	0.075988679	4.004636	8.02	0.11
4	770	12	2.201	1.162	3.634	104.279	1045.72	38.9	5.9	0.056418516	3.929034	7.87	0.05
5	820	12	1.600	1.436	6.052	178.747	1217.71	61.8	10.1	0.040674852	4.242996	8.49	0.06
6	870	12	1.290	1.757	8.709	259.236	1478.65	74.6	14.7	0.03431515	4.287570	8.58	0.05
7	910	12	0.971	1.398	6.249	183.324	1009.20	72.0	10.4	0.038609828	3.985610	7.98	0.04
8	950	12	0.895	1.334	5.240	152.225	872.978	70.2	8.6	0.044369102	4.046194	8.10	0.05
9	990	12	1.194	1.566	4.893	137.775	892.194	61.2	7.8	0.057548482	3.977098	7.96	0.05
10	1030	12	1.169	1.687	4.153	116.718	807.924	58.0	6.6	0.073179907	4.031673	8.07	0.05
11	1070	12	0.811	1.850	3.482	96.883	639.714	63.3	5.5	0.096681165	4.192414	8.39	0.06
12	1120	12	0.649	3.604	4.261	117.822	665.932	72.2	6.7	0.154875895	4.073233	8.15	0.05
13	1180	12	0.651	15.016	7.345	176.137	869.861	78.8	10.0	0.431683839	3.895992	7.80	0.04
14	1400	12	0.391	9.259	3.677	84.505	445.623	77.4	4.8	0.554830242	3.967585	7.94	0.04
							Cumulative %^{39}Ar rlsd =		100.0		Total gas age =	8.97	0.04

note: isotope beams in mV, rlsd = released, error in age includes J error, all errors 1 sigma

(^{36}Ar through ^{40}Ar are measured beam intensities, corrected for decay for the age calculations)

No plateau

No isochron

Wtd mean age = 8.03 0.02

Preffered age = 8.05 0.18

(steps 7-14)

APPENDIX B. ^{40}AR/^{39}AR GEOCHRONOLOGY DATA (CONTINUED)

JM-18-M2-KK Plagioclase

Weight: 27.29 mg J = 0.001968 ± 0.26%

4 amu discrimination = 0.8353 ± 0.03%, $^{40/39}$K = 0.043 ± 10.80%, $^{36/37}$Ca = 0.000209 ± 0.85%, $^{39/37}$Ca = 0.000623 ± 0.51%

Step	**T (C)**	**t (min.)**	**^{36}Ar**	**^{37}Ar**	**^{38}Ar**	**^{39}Ar**	**^{40}Ar**	**%^{40}Ar***	**% ^{39}Ar rlsd**	**Ca/K**	**^{40}Ar*/^{39}ArK**	**Age (Ma)**	**1s.d.**
1	800	12	1.482	5.614	0.632	20.501	590.894	11.5	5.9	1.79249923	3.111937	11.02	0.06
2	860	12	0.148	5.016	0.227	14.633	77.974	38.5	4.2	2.244082735	1.693883	6.00	0.15
3	920	12	0.086	6.213	0.261	18.121	68.023	66.2	5.2	2.244574167	2.005964	7.11	0.03
4	980	12	0.079	7.612	0.320	22.624	73.962	73.8	6.5	2.202618192	1.968074	6.97	0.06
5	1030	12	0.075	7.683	0.324	23.690	75.193	76.4	6.8	2.123079494	1.984474	7.03	0.03
6	1080	12	0.075	8.540	0.366	26.126	81.998	78.7	7.5	2.139870075	2.049512	7.26	0.06
7	1130	12	0.080	9.011	0.373	28.054	87.570	78.0	8.0	2.102695008	2.037917	7.22	0.05
8	1180	12	0.080	8.122	0.345	26.641	82.119	77.8	7.6	1.99571247	1.909831	6.77	0.04
9	1230	12	0.082	7.594	0.375	27.617	83.191	76.9	7.9	1.799934006	1.849899	6.56	0.04
10	1280	12	0.085	11.625	0.494	37.792	109.450	82.4	10.8	2.013634768	1.994936	7.07	0.05
11	1330	12	0.100	25.153	0.713	52.741	146.773	84.7	15.1	3.122909851	2.041876	7.24	0.06
12	1400	12	0.125	29.141	0.711	51.775	153.913	86.5	14.8	3.686112219	2.060541	7.30	0.03

Cumulative %^{39}Ar rlsd = 100.0

Total gas age = 7.27 0.03

note: isotope beams in mV, rlsd = released, error in age includes J error, all errors 1 sigma

(^{36}Ar through ^{40}Ar are measured beam intensities, corrected for decay for the age calculations)

No plateau

No isochron

Wtd mean age = 7.04 0.01

Preffered age = 7.05 0.24

(steps 3-12)

APPENDIX B. ^{40}AR/^{39}AR GEOCHRONOLOGY DATA (CONTINUED)

JM-17-PR6-KK Biotite

Weight: 38.64 mg J = 0.001028 ± 0.52%

4 amu discrimination = 1.0170 ± 0.15%, $^{40/39}$K = 0.0232 ± 18.12%, $^{36/37}$Ca = 0.000263 ± 1.15%, $^{39/37}$Ca = 0.000702 ± 0.49%

Step	**T (C)**	**t (min.)**	**^{36}Ar**	**^{37}Ar**	**^{38}Ar**	**^{39}Ar**	**^{40}Ar**	**%^{40}Ar***	**% ^{39}Ar rlsd**	**Ca/K**	**^{40}Ar*/^{39}ArK**	**Age (Ma)**	**1s.d.**
1	630	12	14.207	1.886	6.747	163.783	4378.22	5.6	9.4	0.059339654	1.510939	2.80	0.12
2	710	12	10.067	1.411	7.314	216.292	3510.96	16.6	12.4	0.033616717	2.702455	5.01	0.06
3	780	12	6.107	1.327	6.462	216.664	2341.44	24.1	12.4	0.031561136	2.610540	4.84	0.05
4	820	12	2.451	0.952	4.122	147.929	1214.21	41.3	8.5	0.033162885	3.393173	6.28	0.08
5	860	12	2.185	0.832	3.430	122.627	1038.26	38.9	7.0	0.034962794	3.289832	6.09	0.07
6	900	12	2.236	0.721	2.602	87.555	904.388	28.0	5.0	0.042435001	2.892259	5.36	0.04
7	940	12	2.663	0.862	2.934	97.871	1045.92	25.9	5.6	0.04538617	2.764096	5.12	0.05
8	980	12	3.521	1.206	3.951	133.821	1459.49	29.8	7.7	0.046440135	3.248715	6.02	0.12
9	1030	12	3.646	1.870	4.394	143.476	1521.70	30.2	8.2	0.067163841	3.210304	5.94	0.07
10	1090	12	3.393	5.422	4.578	144.378	1441.78	31.5	8.3	0.193530057	3.149716	5.83	0.04
11	1150	12	2.743	10.735	5.241	167.745	1307.21	39.1	9.6	0.329807448	3.037206	5.62	0.05
12	1400	12	1.323	6.284	3.261	99.951	689.13	45.0	5.7	0.324008392	3.042074	5.63	0.04
								Cumulative %^{39}Ar rlsd =	100.0		Total gas age =	5.30	0.04

note: isotope beams in mV, rlsd = released, error in age includes J error, all errors 1 sigma

(^{36}Ar through ^{40}Ar are measured beam intensities, corrected for decay for the age calculations)

No plateau

No isochron

Wtd mean age = 5.51 0.02

Preffered age = 5.61 0.48

(steps 2-12)

APPENDIX B. ^{40}AR/^{39}AR GEOCHRONOLOGY DATA (CONTINUED)

JM-17-PR6-KK Amphibole

Weight: 25.51 mg J = 0.001112 ± 0.46%

4 amu discrimination = 0.8838 ± 0.04%, $^{40/39}$K = 0.0232 ± 18.12%, $^{36/37}$Ca = 0.000263 ± 1.15%, $^{39/37}$Ca = 0.000702 ± 0.49%

Step	T (C)	t (min.)	^{36}Ar	^{37}Ar	^{38}Ar	^{39}Ar	^{40}Ar	%^{40}Ar*	% ^{39}Ar rlsd	Ca/K	^{40}Ar*/^{39}ArK	Age (Ma)	1s.d.
1	750	12	1.640	1.038	0.691	12.310	461.358	-13.7	14.4	0.703618132	-6.808633	-13.71	-0.44
2	850	12	0.193	0.370	0.115	2.184	60.122	-7.2	2.5	1.413972431	-1.737485	-3.49	-1.40
3	950	12	0.152	0.634	0.097	1.633	53.594	3.3	1.9	3.242179754	0.912665	1.83	0.35
4	1100	12	0.904	101.413	3.640	35.534	359.141	24.4	41.5	23.98399898	2.346869	4.70	0.13
5	1250	12	0.538	98.280	3.164	32.785	259.326	42.9	38.3	25.20125536	3.190879	6.39	0.05
6	1400	12	0.215	3.738	0.171	1.218	66.343	-8.3	1.4	25.8049863	-3.558009	-7.15	-0.88
								Cumulative %^{39}Ar rlsd =	100.0		Total gas age =	2.27	0.09

note: isotope beams in mV, rlsd = released, error in age includes J error, all errors 1 sigma

(^{36}Ar through ^{40}Ar are measured beam intensities, corrected for decay for the age calculations)

No plateau

No isochron

Wtd mean age = 6.06 0.05

Preffered age = 4.31 2.31

(steps 3-5)

APPENDIX B. ^{40}AR/^{39}AR GEOCHRONOLOGY DATA (CONTINUED)

JM-17-ERN3-KK Plagioclase

Weight: 51.26 mg J = 0.001095 ± 0.39%

4 amu discrimination = 1.0170 ± 0.15%, $^{40/39}$K = 0.0232 ± 18.12%, $^{36/37}$Ca = 0.000263 ± 1.15%, $^{39/37}$Ca = 0.000702 ± 0.49%

Step	T (C)	t (min.)	^{36}Ar	^{37}Ar	^{38}Ar	^{39}Ar	^{40}Ar	%^{40}Ar*	% ^{39}Ar rlsd	Ca/K	^{40}Ar*/^{39}ArK	Age (Ma)	1s.d.
1	500	12	1.877	0.541	1.142	22.880	592.938	8.1	2.6	0.113058451	2.077821	4.10	0.10
2	550	12	1.317	0.830	1.334	31.741	428.552	10.7	3.6	0.125031909	1.439783	2.84	0.13
3	610	12	1.603	1.516	1.921	50.392	534.376	12.8	5.7	0.143847883	1.353088	2.67	0.13
4	670	12	1.582	2.400	2.358	70.396	593.612	22.6	7.9	0.163016539	1.896204	3.74	0.10
5	730	12	1.380	3.686	2.417	85.938	500.020	19.7	9.7	0.205089806	1.140697	2.25	0.09
6	790	12	0.819	4.858	1.975	90.678	356.298	33.3	10.2	0.256174757	1.295297	2.56	0.04
7	850	12	0.446	6.133	1.562	92.510	237.411	45.9	10.4	0.317010103	1.157423	2.29	0.02
8	920	12	0.305	7.628	1.416	93.515	191.191	54.2	10.5	0.390056848	1.078357	2.13	0.02
9	990	12	0.265	7.675	1.273	85.603	171.433	55.9	9.6	0.428739036	1.084946	2.14	0.01
10	1060	12	0.220	5.886	1.403	95.209	170.843	63.3	10.7	0.295616205	1.101671	2.18	0.01
11	1130	12	0.170	3.290	1.307	90.403	156.589	70.1	10.2	0.174013492	1.166546	2.30	0.01
12	1200	12	0.160	1.323	0.700	43.870	95.362	53.5	4.9	0.14419763	1.086466	2.15	0.05
13	1270	12	0.135	1.057	0.328	18.590	59.501	36.8	2.1	0.271880735	1.049470	2.07	0.03
14	1400	12	0.135	1.441	0.307	17.587	63.394	45.0	2.0	0.39180588	1.406321	2.78	0.02
							Cumulative %^{39}Ar rlsd =		100.0		Total gas age =	2.47	0.01
											No plateau		
											Pseudo isochron age = (steps 6-9)	1.92	0.02
											Wtd mean age =	2.21	0.01
											Preferred age = (steps 5-13)	2.23	0.15

note: isotope beams in mV, rlsd = released, error in age includes J error, all errors 1 sigma

(^{36}Ar through ^{40}Ar are measured beam intensities, corrected for decay for the age calculations)

APPENDIX B. ^{40}AR/^{39}AR GEOCHRONOLOGY DATA (CONTINUED)

JM-17-ERC5-KK Feldspar plus Glass

Weight: 25.11 mg J = 0.001108 ± 0.32%

4 amu discrimination = 0.8838 ± 0.04%, $^{40/39}$K = 0.0232 ± 18.12%, $^{36/37}$Ca = 0.000263 ± 1.15%, $^{39/37}$Ca = 0.000702 ± 0.49%

Step	T (C)	t (min.)	^{36}Ar	^{37}Ar	^{38}Ar	^{39}Ar	^{40}Ar	%^{40}Ar*	% ^{39}Ar rlsd	Ca/K	^{40}Ar*/^{39}ArK	Age (Ma)	1s.d.
1	500	12	3.287	0.584	2.076	49.271	1109.60	0.9	8.1	0.093344042	0.185119	0.37	0.31
2	540	12	3.162	0.671	2.210	52.792	1113.31	5.0	8.7	0.100096855	1.006105	2.01	0.31
3	580	12	3.649	0.803	2.622	61.404	1240.36	1.5	10.1	0.102987684	0.298211	0.60	0.66
4	620	12	3.894	0.946	2.797	67.996	1298.46	-0.4	11.2	0.10956581	-0.071536	-0.14	-0.40
5	660	12	3.355	0.932	2.823	70.120	1251.09	10.3	11.5	0.104674438	1.763675	3.52	0.54
6	700	12	3.213	0.971	2.690	68.770	1122.98	4.2	11.3	0.111195626	0.664104	1.33	0.11
7	760	12	2.733	1.024	2.613	72.657	1035.08	11.8	12.0	0.110991562	1.611308	3.22	0.25
8	840	12	1.833	0.890	1.765	61.872	663.03	7.6	10.2	0.113257251	0.782763	1.56	0.08
9	940	12	0.831	0.452	0.812	37.492	339.29	17.9	6.2	0.094943485	1.530624	3.06	0.31
10	1100	12	0.523	0.615	0.808	52.621	247.49	29.3	8.7	0.092040926	1.290119	2.58	0.05
11	1400	12	0.291	0.164	0.226	12.696	104.09	7.3	2.1	0.101728626	0.505915	1.01	0.11
							Cumulative %^{39}Ar rlsd =		100.0		Total gas age =	1.78	0.07

note: isotope beams in mV, rlsd = released, error in age includes J error, all errors 1 sigma

(^{36}Ar through ^{40}Ar are measured beam intensities, corrected for decay for the age calculations)

No plateau

No isochron

APPENDIX B. ^{40}AR/^{39}AR GEOCHRONOLOGY DATA (CONTINUED)

JM-17-ERS2-KK Feldspar plus Glass

Weight: 41.86 mg J = 0.001047 ± 0.41%

4 amu discrimination = 0.8838 ± 0.04%, $^{40/39}$K = 0.0232 ± 18.12%, $^{36/37}$Ca = 0.000263 ± 1.15%, $^{39/37}$Ca = 0.000702 ± 0.49%

Step	T (C)	t (min.)	^{36}Ar	^{37}Ar	^{38}Ar	^{39}Ar	^{40}Ar	%^{40}Ar*	% ^{39}Ar rlsd	Ca/K	^{40}Ar*/^{39}ArK	Age (Ma)	1s.d.
1	500	12	5.941	0.876	3.036	67.456	2092.50	5.0	7.4	0.098353854	1.500487	2.83	0.07
2	550	12	7.367	1.162	3.735	85.815	2508.25	1.7	9.4	0.102553701	0.487188	0.92	0.97
3	590	12	7.286	1.341	4.345	99.820	2818.40	13.5	10.9	0.101746511	3.686016	6.95	0.61
4	630	12	8.268	1.600	4.753	110.829	2964.33	6.7	12.1	0.109339198	1.724809	3.26	0.17
5	670	12	8.228	1.714	4.963	117.563	2951.42	6.7	12.8	0.110420477	1.628816	3.07	0.38
6	720	12	9.128	1.901	5.345	129.586	3023.55	-1.0	14.2	0.111104995	-0.223388	-0.42	-0.22
7	780	12	7.698	1.863	5.010	123.633	2647.16	2.7	13.5	0.114127	0.563466	1.06	0.27
8	840	12	3.929	1.103	2.870	79.271	1535.35	14.5	8.7	0.105382857	2.700663	5.09	0.54
9	910	12	1.646	0.528	1.138	37.086	669.470	18.0	4.1	0.107828371	3.119115	5.88	0.68
10	980	12	0.917	0.223	0.470	17.283	378.201	18.9	1.9	0.097722262	3.913508	7.38	0.73
11	1060	12	0.655	0.194	0.343	14.486	253.096	13.2	1.6	0.101428854	2.166712	4.09	0.53
12	1150	12	0.396	0.290	0.458	27.130	179.506	27.3	3.0	0.080956879	1.658515	3.13	0.04
13	1400	12	0.428	0.073	0.158	5.115	174.689	19.6	0.6	0.108090213	5.988406	11.28	0.28
							Cumulative %^{39}Ar rlsd =		100.0		Total gas age =	2.97	0.06

note: isotope beams in mV, rlsd = released, error in age includes J error, all errors 1 sigma

(^{36}Ar through ^{40}Ar are measured beam intensities, corrected for decay for the age calculations)

No plateau

No isochron

APPENDIX B. ^{40}AR/^{39}AR GEOCHRONOLOGY DATA (CONTINUED)

JM-17-I2-KK Anorthoclase

Weight: 29.29 mg J = 0.0011 ± 0.36%

4 amu discrimination = 1.0170 ± 0.15%, $^{40/39}$K = 0.0232 ± 18.12%, $^{36/37}$Ca = 0.000263 ± 1.15%, $^{39/37}$Ca = 0.000702 ± 0.49%

Step	**T (C)**	**t (min.)**	**^{36}Ar**	**^{37}Ar**	**^{38}Ar**	**^{39}Ar**	**^{40}Ar**	**%^{40}Ar***	**% ^{39}Ar rlsd**	**Ca/K**	**^{40}Ar*/^{39}ArK**	**Age (Ma)**	**1s.d.**
1	600	12	0.215	0.062	0.189	7.421	74.614	17.5	0.6	0.039003556	1.653429	3.31	0.35
2	660	12	0.037	0.070	0.160	12.168	19.404	59.8	1.0	0.026856671	0.710883	1.42	0.03
3	730	12	0.030	0.131	0.373	26.320	27.508	81.7	2.3	0.023235834	0.693891	1.39	0.02
4	800	12	0.033	0.194	0.569	37.352	33.373	81.5	3.2	0.024247159	0.616433	1.23	0.02
5	870	12	0.034	0.291	0.856	51.368	41.346	84.0	4.4	0.026446829	0.592447	1.19	0.01
6	940	12	0.030	0.420	1.090	64.693	50.550	87.7	5.6	0.030308594	0.608437	1.22	0.01
7	1010	12	0.033	0.600	1.226	80.373	59.608	87.5	6.9	0.034851018	0.587950	1.18	0.01
8	1080	12	0.039	0.804	1.483	103.560	75.695	87.2	8.9	0.036244206	0.590448	1.18	0.01
9	1140	12	0.049	0.988	1.717	125.270	91.657	87.2	10.8	0.036820063	0.593946	1.19	0.01
10	1190	12	0.059	1.141	1.964	145.627	108.185	86.0	12.6	0.036577866	0.601441	1.20	0.01
11	1240	12	0.061	1.680	2.779	208.402	146.967	88.5	18.0	0.037634155	0.597943	1.20	0.01
12	1290	12	0.045	1.708	2.860	220.042	150.154	91.8	19.0	0.036237386	0.600942	1.20	0.01
13	1400	12	0.056	0.630	1.022	76.712	63.765	84.3	6.6	0.038339999	0.607938	1.22	0.01
								Cumulative %^{39}Ar rlsd =	100.0		Total gas age =	1.22	0.01
											Plateau age =	1.19	0.01
											(steps 5-12)		
											Isochron age =	1.09	0.07
											(steps 6-11)		

note: isotope beams in mV, rlsd = released, error in age includes J error, all errors 1 sigma

(^{36}Ar through ^{40}Ar are measured beam intensities, corrected for decay for the age calculations)

APPENDIX C. X-RAY FLUORESCENCE: UNNORMALIZED MAJOR AND TRACE ELEMENTS

Unnormalized Major Elements (weight percent):

Sample	**SiO_2**	**TiO_2**	**Al_2O_3**	**FeO***	**MnO**	**MgO**	**CaO**	**Na_2O**	**K_2O**	**P_2O_5**	**Sum**	**LOI (%)**	**Total**
JM-17-O1-KK	73.5946	0.2434	13.9479	1.5049	0.0711	0.3430	1.2583	4.1450	3.9294	0.0630	99.1005	0.4083	99.5088
JM-17-O2-KK	72.5845	0.2610	14.5536	1.6242	0.0825	0.2890	1.4610	4.2665	3.8121	0.0671	99.0015	0.5768	99.5783
JM-17-O3-KK	72.7656	0.2565	14.3057	1.5530	0.0738	0.3043	1.4385	4.3205	3.8546	0.0621	98.9344	0.4747	99.4091
JM-18-M2-KK	76.4832	0.1193	12.8522	0.6726	0.0908	0.0357	0.4256	3.9738	4.4710	0.0130	99.1370	0.4241	99.5612
JM-17-PR3-KK	69.5654	0.2465	15.1222	2.1862	0.0438	0.7655	2.5720	3.3689	3.3265	0.0639	97.2609	1.9692	99.2300
JM-17-PR4-KK	70.2200	0.2508	15.7852	1.4459	0.0296	0.7347	2.6239	3.7315	2.8512	0.0274	97.7002	1.5170	99.2172
JM-17-PR6-KK	70.4883	0.2324	14.6902	1.9878	0.0454	0.6970	2.5268	3.6734	3.1878	0.0730	97.6020	1.9184	99.5204
JM-17-ERN1-KK	74.6415	0.0803	12.2817	0.5033	0.0555	0.0377	0.4389	3.6473	4.5661	0.0068	96.2590	3.2046	99.4637
JM-17-ERN3-KK	74.9855	0.0800	12.3475	0.5017	0.0556	0.0345	0.4387	3.6676	4.6429	0.0058	96.7598	2.9780	99.7377
JM-17-ERN4-KK	74.7688	0.0795	12.3620	0.5047	0.0568	0.0336	0.4396	3.4910	4.8677	0.0058	96.6095	3.0079	99.6175
JM-17-ERS2-KK	74.5266	0.0807	12.2824	0.5034	0.0556	0.0380	0.4393	3.5447	4.6400	0.0070	96.1177	3.4356	99.5533
JM-17-ERS3-KK	74.6914	0.0791	12.3089	0.5041	0.0555	0.0399	0.4379	3.4993	4.7655	0.0060	96.3876	3.4266	99.8142
JM-17-ERS4-KK	76.9087	0.0807	12.6203	0.5136	0.0569	0.0372	0.4472	3.9096	4.6024	0.0061	99.1827	0.3052	99.4880
JM-17-ERC3-KK	74.3948	0.0795	12.2799	0.5014	0.0557	0.0387	0.4370	3.6023	4.5825	0.0062	95.9779	3.6719	99.6498
JM-17-ERC4-KK	74.7646	0.0795	12.3980	0.5125	0.0559	0.0403	0.4332	3.5051	4.7018	0.0060	96.4970	3.3040	99.8010
JM-17-ERC5-KK	74.3609	0.0791	12.2989	0.4992	0.0552	0.0416	0.4358	3.4801	4.7437	0.0062	96.0007	3.4425	99.4432
JM-17-ERC6-KK	75.3782	0.0797	12.3696	0.5038	0.0554	0.0353	0.4384	3.8164	4.4532	0.0083	97.1382	2.4293	99.5675
JM-17-I1-KK	77.3270	0.0807	11.7075	1.2869	0.0694	0.0000	0.0725	3.8356	4.3482	0.0118	98.7397	0.5046	99.2443
JM-17-I2-KK	77.6204	0.0822	11.7893	1.3213	0.0588	0.0065	0.0808	3.8810	4.3920	0.0101	99.2424	0.5666	99.8090
JM-17-O2-KK®	72.5758	0.2622	14.5253	1.6218	0.0827	0.2933	1.4590	4.2624	3.8163	0.0671	98.9660	0.5768	99.5428
Standard Deviation	0.0061	0.0008	0.0200	0.0017	0.0002	0.0030	0.0014	0.0029	0.0030	0.0000	0.0251	0.0000	0.0251
2-sigma Uncertainty	0.0123	0.0017	0.0400	0.0035	0.0003	0.0061	0.0028	0.0059	0.0061	0.0001	0.0502	0.0000	0.0502

® denotes a duplicate bead made from the same rock powder

APPENDIX C. X-RAY FLUORESCENCE: UNNORMALIZED MAJOR AND TRACE ELEMENTS (CONTINUED)

Unnormalized Trace Elements (ppm):

Sample	Ni	Cr	Sc	V	Ba	Rb	Sr	Zr	Y	Nb
JM-17-O1-KK	6.1740	3.6260	4.7040	10.2900	1351.9100	80.4380	214.3260	157.8780	23.7160	25.2840
JM-17-O2-KK	6.5340	3.0690	3.4650	12.1770	1368.1800	75.6760	258.7860	184.1640	30.7890	24.7500
JM-17-O3-KK	5.0235	2.8565	3.8415	11.8200	1393.3810	83.4980	254.3270	178.3500	26.2010	25.1175
JM-18-M2-KK	5.5608	3.5748	3.1776	2.2839	847.7910	102.3596	41.5074	89.7672	26.5131	31.1802
JM-17-PR3-KK	9.8980	9.8980	5.4880	25.8720	1175.4120	60.1210	383.5720	120.9720	16.9540	6.0760
JM-17-PR4-KK	8.5260	9.3100	5.3900	19.9920	1283.9960	48.5000	410.1300	120.7680	10.2900	6.9580
JM-17-PR6-KK	8.3300	10.0940	4.9000	24.9900	1186.7800	57.0480	380.4360	115.0560	13.2300	5.7820
JM-17-ERN1-KK	3.4825	4.5770	3.1840	3.9800	20.3975	141.9750	4.6765	63.9630	21.0940	42.0885
JM-17-ERN3-KK	5.7130	2.5610	3.4475	3.5460	15.8585	144.0230	4.0385	63.4475	20.5865	41.2715
JM-17-ERN4-KK	3.3660	2.0790	3.8610	2.1780	20.6910	143.9780	4.2570	63.8600	19.7010	42.2730
JM-17-ERS2-KK	3.6445	2.8565	3.7430	1.2805	20.8820	141.9960	5.5160	64.2675	20.5865	41.6655
JM-17-ERS3-KK	3.1520	2.5610	3.9400	1.2805	21.6700	143.0570	4.8265	64.1650	20.9805	42.1580
JM-17-ERS4-KK	2.8420	2.5480	4.2140	2.0580	14.3080	145.6930	3.9200	64.7700	20.7760	42.7280
JM-17-ERC3-KK	3.1520	1.8715	3.1520	2.1670	26.2010	141.2230	6.6980	63.5500	20.6850	41.5670
JM-17-ERC4-KK	3.5460	2.7580	3.2505	1.2805	17.9270	142.2850	4.3340	64.5750	21.0790	42.7490
JM-17-ERC5-KK	3.8415	2.4625	4.0385	1.9700	14.3810	142.0920	5.0235	63.5500	20.6850	41.7640
JM-17-ERC6-KK	2.4500	2.9400	3.9200	3.0380	20.9720	142.1390	4.3120	64.2600	21.0700	42.1400
JM-17-I1-KK	3.8610	4.4550	1.2870	2.3760	70.5870	142.5220	11.4840	205.5880	45.7380	65.6370
JM-17-I2-KK	4.2570	4.0590	1.2870	2.9700	63.7560	143.2990	11.6820	212.7980	40.1940	66.4290
JM-17-O2-KK®	5.2205	2.5610	4.4325	12.2140	1376.2420	76.1620	259.1535	180.8100	30.6335	24.9205
Standard Deviation	0.9288	0.3592	0.6841	0.0262	5.7007	0.3437	0.2599	2.3716	0.1100	0.1206
2-sigma Uncertainty	1.8576	0.7184	1.3683	0.0523	11.4014	0.6873	0.5197	4.7433	0.2199	0.2411

® denotes a duplicate bead made from the same rock powder

APPENDIX C. X-RAY FLUORESCENCE: UNNORMALIZED MAJOR AND TRACE ELEMENTS (CONTINUED)

Unnormalized Trace Elements (ppm):

Sample	Ga	Cu	Zn	Pb	La	Ce	Th	Nd	U
JM-17-O1-KK	14.9940	2.1560	31.4580	20.9720	41.1600	72.7160	9.6040	25.3820	2.8420
JM-17-O2-KK	15.3450	3.3660	36.9270	21.7800	50.0940	78.0120	10.7910	36.5310	3.2670
JM-17-O3-KK	14.7750	9.0620	41.3700	20.5865	47.7725	72.5945	9.5545	28.4665	3.3490
JM-18-M2-KK	14.4978	1.9860	28.8963	22.7397	23.4348	41.0109	10.8237	17.1789	4.2699
JM-17-PR3-KK	16.0720	10.1920	38.7100	21.2660	29.4980	46.3540	3.5280	24.5000	1.3720
JM-17-PR4-KK	16.0720	5.6840	32.4380	24.1080	24.4020	39.9840	2.8420	17.2480	0.9800
JM-17-PR6-KK	15.4840	7.9380	36.3580	21.8540	23.5200	38.5140	2.2540	16.5620	0.8820
JM-17-ERN1-KK	15.8205	0.5970	23.2830	27.1635	18.5070	31.7405	18.1090	13.0345	7.9600
JM-17-ERN3-KK	16.7450	0.1970	24.1325	27.3830	15.2675	37.1345	17.8285	14.9720	6.4025
JM-17-ERN4-KK	16.3350	0.6930	25.3440	27.6210	16.3350	36.6300	17.4240	12.4740	7.2270
JM-17-ERS2-KK	15.2675	1.3790	24.2310	26.7920	18.0255	36.8390	17.8285	13.6915	7.7815
JM-17-ERS3-KK	15.2675	0.0000	23.9355	27.2845	18.5180	38.8090	17.6315	14.6765	7.8800
JM-17-ERS4-KK	16.1700	0.7840	25.0880	26.9500	18.1300	34.2020	17.0520	14.4060	7.3500
JM-17-ERC3-KK	15.7600	0.7880	24.0340	26.9890	18.1240	34.2780	17.1390	12.3125	6.5010
JM-17-ERC4-KK	15.4645	0.8865	24.2310	27.0875	18.5180	32.1110	17.1390	11.5245	7.5845
JM-17-ERC5-KK	16.0555	0.0985	23.9355	27.0875	18.9120	34.8690	16.7450	13.1990	7.7815
JM-17-ERC6-KK	15.9740	1.0780	24.2060	26.8520	15.8760	33.9080	17.8360	12.1520	7.3500
JM-17-I1-KK	21.6810	2.1780	65.5380	16.5330	52.4700	114.8400	16.3350	39.7980	4.1580
JM-17-I2-KK	22.7700	0.9900	63.5580	23.5620	45.5400	114.4440	17.7210	34.4520	4.4550
JM-17-O2-KK®	14.9720	2.9550	35.0660	21.9655	46.3935	76.0420	9.9485	34.6720	2.6595
Standard Deviation	0.2638	0.2906	1.3159	0.1312	2.6166	1.3930	0.5957	1.3145	0.4296
2-sigma Uncertainty	0.5275	0.5812	2.6319	0.2623	5.2333	2.7860	1.1915	2.6290	0.8591

® denotes a duplicate bead made from the same rock powder

APPENDIX D. INDUCTIVELY COUPLED PLASMA MASS SPECTROMETRY TRACE ELEMENT ANALYSES (PPM)

Sample	La	Ce	Pr	Nd	Sm	Eu	Gd	Tb	Dy	Ho	Er	Tm
JM-17-O1-KK	43.1014	75.6446	8.3264	27.9018	5.0143	1.0239	4.0940	0.6919	4.2647	0.8564	2.4296	0.3770
JM-17-O2-KK	52.2873	77.7363	10.5981	36.3405	6.7042	1.2506	5.6450	0.9253	5.4058	1.0693	2.8573	0.4206
JM-17-O3-KK	47.8694	77.1745	9.3747	31.7519	5.6173	1.1779	4.7600	0.7949	4.7168	0.9310	2.6363	0.4057
JM-18-M2-KK	22.8709	46.1127	5.3660	17.9115	4.3052	0.5821	4.0207	0.7266	4.6626	0.9370	2.6455	0.3955
JM-17-PR3-KK	31.0274	47.2027	6.6805	23.7961	4.7103	1.0520	3.7864	0.5829	3.3302	0.6161	1.5862	0.2239
JM-17-PR4-KK	26.1186	40.0057	4.7651	16.3786	3.0036	0.9190	2.3093	0.3553	1.9854	0.3746	0.9989	0.1514
JM-17-PR6-KK	23.0309	39.3702	4.4536	15.7142	2.9895	0.7968	2.5323	0.4027	2.3556	0.4600	1.2265	0.1849
JM-17-ERN1-KK	18.7731	38.3746	4.3454	14.1343	3.3728	0.2010	3.1555	0.6013	3.5798	0.7181	2.0097	0.3141
JM-17-ERN3-KK	18.0921	37.6033	4.1213	13.4317	3.3335	0.2006	3.0645	0.5750	3.5511	0.6944	1.9896	0.3058
JM-17-ERN4-KK	17.7617	37.1056	4.0592	13.3328	3.2666	0.1866	3.0370	0.5717	3.5129	0.7018	1.9333	0.3018
JM-17-ERS2-KK	18.1295	36.9974	4.2306	13.7262	3.3851	0.1998	3.1366	0.5804	3.5555	0.7135	1.9782	0.3162
JM-17-ERS3-KK	18.2983	37.1902	4.2249	13.7436	3.3544	0.1944	3.0950	0.5717	3.5510	0.7031	1.9247	0.3130
JM-17-ERS4-KK	18.2438	37.9671	4.1599	13.6775	3.3702	0.1933	3.1566	0.5773	3.5693	0.7166	1.9794	0.3066
JM-17-ERC3-KK	17.7526	37.0355	4.0558	13.2478	3.2552	0.2000	3.0133	0.5604	3.5155	0.6964	1.9749	0.2987
JM-17-ERC4-KK	17.6939	37.1718	4.0785	13.3645	3.3327	0.1859	3.0568	0.5686	3.4688	0.7076	1.9434	0.3000
JM-17-ERC5-KK	18.1194	37.1307	4.1276	13.4947	3.4290	0.1803	3.0795	0.5624	3.5522	0.7126	1.9657	0.3056
JM-17-ERC6-KK	18.1369	37.7807	4.1573	13.4028	3.2661	0.2060	3.1706	0.5910	3.5827	0.7032	1.9974	0.3067
JM-17-I1-KK	53.8169	115.2670	12.0001	41.0659	9.4362	0.1486	8.5556	1.5713	9.4430	1.8393	5.0063	0.7504
JM-17-I2-KK	46.9597	117.4027	10.6018	35.5864	8.1283	0.1410	7.2836	1.3469	8.3228	1.6357	4.4787	0.6810
JM-17-O2-KK®	53.0191	78.8325	10.6597	36.6502	6.6401	1.1972	5.7613	0.9174	5.4565	1.0578	2.8793	0.4218
Standard Deviation	0.5174	0.7751	0.0436	0.2190	0.0453	0.0377	0.0822	0.0056	0.0359	0.0081	0.0155	0.0008
2-sigma Uncertainty	1.0349	1.5503	0.0872	0.4380	0.0906	0.0755	0.1644	0.0112	0.0717	0.0163	0.0310	0.0017

® denotes a duplicate bead made from the same rock powder

APPENDIX D. INDUCTIVELY COUPLED PLASMA MASS SPECTROMETRY TRACE ELEMENT ANALYSES (PPM) (CONTINUED)

Sample	Yb	Lu	Ba	Th	Nb	Y	Hf	Ta	U	Pb	Rb	Cs
JM-17-O1-KK	2.4776	0.3911	1400.6613	10.4799	24.9707	24.4256	4.6425	1.9507	2.9073	20.9540	82.2767	1.8043
JM-17-O2-KK	2.6432	0.4271	1418.1921	10.1236	24.6931	30.5703	4.9437	1.8796	3.0604	21.0751	73.6708	1.4444
JM-17-O3-KK	2.6821	0.4326	1448.4238	10.0342	24.9827	26.9522	4.9493	1.8761	2.9154	21.3669	83.0561	2.2521
JM-18-M2-KK	2.5727	0.4148	857.8448	11.4653	31.0012	26.0771	3.7078	2.2348	3.8442	22.9690	102.0028	2.3785
JM-17-PR3-KK	1.4051	0.2245	1208.2062	3.6574	6.8169	16.7221	3.4247	0.6601	1.0166	20.6338	58.0969	1.7427
JM-17-PR4-KK	0.9799	0.1494	1329.2354	3.7505	6.9680	9.9641	3.5446	0.6746	0.7499	23.7817	46.7006	1.3957
JM-17-PR6-KK	1.1597	0.1899	1223.4742	3.0920	6.3048	12.5580	3.3131	0.6148	0.9406	20.9007	54.8794	1.5128
JM-17-ERN1-KK	2.0016	0.3112	18.3301	17.9753	41.8391	20.9474	3.0859	4.2585	8.1640	26.8998	141.3424	4.2602
JM-17-ERN3-KK	2.0026	0.3050	12.9612	17.4601	42.0295	20.7082	3.0849	4.2491	8.1730	26.7868	141.3826	4.2819
JM-17-ERN4-KK	2.0075	0.3171	20.8472	17.3537	41.7979	20.4182	3.0977	4.2875	8.0512	27.3410	142.2648	4.2178
JM-17-ERS2-KK	2.0114	0.3096	21.0371	17.5739	41.6983	20.7464	3.0973	4.2034	7.9933	26.7637	140.8087	4.2029
JM-17-ERS3-KK	1.9737	0.3110	18.8889	17.5499	41.7059	20.6126	3.0275	4.2239	7.9911	26.5423	139.5425	4.1502
JM-17-ERS4-KK	2.0426	0.3114	11.8649	17.8757	42.7093	20.8572	3.1164	4.3320	8.2986	27.3931	142.7946	4.3254
JM-17-ERC3-KK	1.9888	0.3176	24.8231	17.3032	41.5590	20.2970	3.0447	4.2676	7.9320	26.4236	137.3026	4.1312
JM-17-ERC4-KK	1.9666	0.3059	15.8732	17.5269	41.7944	20.4369	3.0517	4.2795	8.0143	26.8376	138.4118	4.1764
JM-17-ERC5-KK	1.9737	0.3121	14.1972	17.5261	41.5045	20.1835	3.0150	4.2265	8.0692	26.2974	137.5994	4.1863
JM-17-ERC6-KK	1.9908	0.3117	21.0161	17.6192	41.9163	20.5538	3.1338	4.2999	8.1564	26.8651	138.3629	4.1850
JM-17-I1-KK	4.7111	0.7066	69.6769	17.9775	65.0520	46.1256	7.5845	4.3425	4.8828	15.6609	141.5435	2.5041
JM-17-I2-KK	4.2982	0.6533	66.4861	18.2957	65.8801	40.2293	7.7548	4.3333	4.9345	23.3422	142.6243	2.3455
JM-17-O2-KK®	2.6598	0.4057	1425.1597	9.9998	24.6812	30.5581	4.8802	1.8988	3.0244	21.0552	73.0962	1.4301
Standard Deviation	0.0117	0.0151	4.9268	0.0876	0.0084	0.0087	0.0449	0.0136	0.0254	0.0141	0.4063	0.0101
2-sigma Uncertainty	0.0234	0.0303	9.8536	0.1752	0.0168	0.0173	0.0898	0.0272	0.0509	0.0282	0.8126	0.0202

® denotes a duplicate bead made from the same rock powder

APPENDIX D. INDUCTIVELY COUPLED PLASMA MASS SPECTROMETRY TRACE ELEMENT ANALYSES (PPM) (CONTINUED)

Sample	Sr	Sc	Zr	Ta/Yb	Y/Yb	Th/Yb	Th/Nb
JM-17-O1-KK	214.3239	3.3144	164.6982	0.7874	9.8586	4.2299	0.4197
JM-17-O2-KK	253.2748	3.4379	179.4897	0.7111	11.5655	3.8300	0.4100
JM-17-O3-KK	255.4251	3.2132	179.6826	0.6995	10.0490	3.7412	0.4016
JM-18-M2-KK	41.6426	3.4130	92.7047	0.8686	10.1359	4.4565	0.3698
JM-17-PR3-KK	372.5636	4.4990	116.2195	0.4698	11.9013	2.6030	0.5365
JM-17-PR4-KK	398.4450	4.0911	117.2106	0.6885	10.1689	3.8276	0.5382
JM-17-PR6-KK	368.7563	3.8997	111.1820	0.5301	10.8284	2.6662	0.4904
JM-17-ERN1-KK	4.5516	2.7334	63.1788	2.1275	10.4652	8.9803	0.4296
JM-17-ERN3-KK	4.5523	2.6932	62.8382	2.1218	10.3408	8.7188	0.4154
JM-17-ERN4-KK	4.9421	2.7500	62.4222	2.1358	10.1712	8.6446	0.4152
JM-17-ERS2-KK	5.9671	2.7114	63.6390	2.0898	10.3145	8.7372	0.4215
JM-17-ERS3-KK	5.7487	2.6461	62.8053	2.1401	10.4435	8.8918	0.4208
JM-17-ERS4-KK	4.5706	2.6502	63.7260	2.1208	10.2111	8.7514	0.4185
JM-17-ERC3-KK	6.0388	2.5414	62.1238	2.1458	10.2054	8.7001	0.4164
JM-17-ERC4-KK	4.6309	2.6405	63.1035	2.1761	10.3919	8.9122	0.4194
JM-17-ERC5-KK	4.8821	2.8010	62.0106	2.1414	10.2264	8.8800	0.4223
JM-17-ERC6-KK	5.2661	2.5827	63.1727	2.1599	10.3245	8.8504	0.4203
JM-17-I1-KK	12.5415	0.8381	206.9560	0.9218	9.7907	3.8160	0.2764
JM-17-I2-KK	12.5446	0.9179	213.7943	1.0082	9.3596	4.2566	0.2777
JM-17-O2-KK®	250.4093	3.1604	178.8564	0.7139	3.7597	11.4890	0.4052
Standard Deviation	2.0262	0.1962	0.4478	0.0020	0.0498	0.0541	0.0034
2-sigma Uncertainty	4.0523	0.3924	0.8957	0.0040	0.0995	0.1081	0.0068

® denotes a duplicate bead made from the same rock powder

APPENDIX E. ELECTRON MICROPROBE ANALYSES OF FELDSPARS. UNRELIABLE DATA NOT INCLUDED IN RESULTS HAVE BEEN OMITTED.

Sample	Point	SiO_2	MgO	K_2O	TiO_2	Na_2O	P_2O_5	CaO	FeO	Al_2O_3	MnO	BaO	Total
JM-17-O2-KK	1	62.910	0.000	0.726	0.054	7.971	0.000	4.674	0.260	24.133	0.000	0.111	100.839
Plagioclase 5	2	62.326	0.000	0.667	0.000	7.736	0.000	5.202	0.164	24.487	0.044	0.064	100.690
Rim to Rim	3	62.617	0.000	0.653	0.000	7.565	0.000	5.211	0.167	24.355	0.004	0.180	100.752
	4	60.962	0.020	0.548	0.047	7.180	0.000	6.025	0.177	24.537	0.000	0.000	99.496
	5	61.346	0.022	0.640	0.027	7.553	0.000	5.370	0.144	24.032	0.038	0.000	99.172
	6	61.985	0.002	0.599	0.055	7.540	0.000	5.675	0.182	25.010	0.000	0.113	101.161
	7	61.895	0.000	0.657	0.055	7.661	0.000	5.587	0.202	24.031	0.000	0.051	100.139

Sample	Point	SiO_2	MgO	K_2O	TiO_2	Na_2O	P_2O_5	CaO	FeO	Al_2O_3	MnO	BaO	Total
JM-17-O2-KK	1	56.943	0.032	0.315	0.031	5.617	0.000	9.214	0.223	27.908	0.029	0.014	100.326
Plagioclase 8a	2	56.794	0.041	0.295	0.000	5.805	0.000	9.422	0.287	27.992	0.023	0.079	100.738
Core to Rim	3	56.772	0.004	0.284	0.043	5.521	0.000	9.599	0.184	28.164	0.030	0.000	100.601
	4	57.052	0.030	0.309	0.098	5.940	0.000	9.128	0.270	27.685	0.000	0.202	100.714

Sample	Point	SiO_2	MgO	K_2O	TiO_2	Na_2O	P_2O_5	CaO	FeO	Al_2O_3	MnO	BaO	Total
JM-17-O2-KK	6	59.731	0.000	0.429	0.055	6.728	0.000	7.366	0.177	26.019	0.000	0.056	100.561
Plagioclase 8b	8	59.994	0.000	0.493	0.000	7.055	0.000	6.726	0.230	24.258	0.048	0.030	98.834
Core to Rim	9	61.130	0.000	0.535	0.000	7.239	0.000	6.276	0.223	25.347	0.041	0.075	100.866
	10	62.034	0.000	0.582	0.000	7.559	0.000	5.851	0.215	25.086	0.070	0.124	101.521

Sample	Point	SiO_2	MgO	K_2O	TiO_2	Na_2O	P_2O_5	CaO	FeO	Al_2O_3	MnO	BaO	Total
JM-17-O2-KK	1	60.271	0.010	0.528	0.000	7.089	0.000	6.167	0.190	24.841	0.000	0.036	99.132
Plagioclase 9	2	60.613	0.000	0.529	0.000	7.060	0.000	6.521	0.233	25.383	0.020	0.124	100.483
Rim to Rim	3	60.268	0.022	0.537	0.074	7.438	0.000	6.240	0.194	25.266	0.072	0.126	100.237
	4	60.855	0.000	0.495	0.070	7.145	0.000	6.536	0.254	25.394	0.000	0.000	100.749
	5	61.402	0.004	0.624	0.000	7.561	0.000	5.781	0.206	24.508	0.000	0.000	100.086
	6	59.465	0.000	0.519	0.000	7.432	0.000	6.310	0.207	25.359	0.014	0.000	99.306

APPENDIX E. ELECTRON MICROPROBE ANALYSES OF FELDSPARS (CONTINUED)

Sample	Point	SiO_2	MgO	K_2O	TiO_2	Na_2O	P_2O_5	CaO	FeO	Al_2O_3	MnO	BaO	Total
JM-18-M2-KK	1	63.868	0.000	9.076	0.000	5.084	0.063	0.254	0.139	19.705	0.000	1.280	99.469
Sanidine 2	2	65.555	0.003	8.871	0.000	5.267	0.010	0.284	0.084	19.025	0.000	1.207	100.306
Rim to Rim	3	65.160	0.011	8.811	0.041	5.393	0.000	0.266	0.085	19.996	0.000	1.316	101.079
	4	65.694	0.000	8.796	0.057	5.277	0.003	0.246	0.072	19.538	0.000	1.199	100.882
	5	65.215	0.000	8.655	0.000	5.150	0.013	0.273	0.059	20.013	0.000	1.713	101.091

Sample	Point	SiO_2	MgO	K_2O	TiO_2	Na_2O	P_2O_5	CaO	FeO	Al_2O_3	MnO	BaO	Total
JM-18-M2-KK	1	64.549	0.000	1.672	0.000	8.735	0.000	2.563	0.218	22.026	0.005	0.073	99.841
Plagioclase 3	2	65.049	0.000	1.842	0.000	9.068	0.000	2.198	0.169	21.668	0.018	0.065	100.077
Rim to Rim	3	64.989	0.009	1.544	0.000	9.163	0.000	2.344	0.181	22.030	0.005	0.079	100.344
	4	65.272	0.032	1.853	0.000	8.943	0.000	1.949	0.167	21.457	0.000	0.188	99.861
	5	65.326	0.003	1.732	0.000	9.054	0.000	2.264	0.203	21.891	0.016	0.153	100.642
	6	65.000	0.018	1.487	0.024	9.304	0.000	2.426	0.117	21.789	0.063	0.157	100.385
	7	64.819	0.014	1.686	0.072	9.175	0.020	2.147	0.160	21.753	0.000	0.125	99.971
	8	64.761	0.000	1.299	0.000	8.959	0.028	2.849	0.135	22.663	0.011	0.116	100.821
	9	64.551	0.000	1.343	0.089	9.115	0.000	2.736	0.219	20.897	0.003	0.088	99.041
	10	63.988	0.000	1.438	0.000	8.841	0.000	2.626	0.140	22.332	0.045	0.092	99.502
	11	64.773	0.007	1.413	0.000	9.055	0.015	2.681	0.096	22.480	0.034	0.121	100.675
	12	65.108	0.000	1.461	0.000	9.005	0.000	2.591	0.259	22.690	0.026	0.173	101.313
	13	64.920	0.000	1.454	0.024	8.966	0.000	2.399	0.191	22.227	0.000	0.185	100.366
	14	64.505	0.000	1.312	0.000	9.096	0.000	2.742	0.198	22.576	0.011	0.164	100.604
	15	64.444	0.000	1.301	0.072	8.900	0.000	2.901	0.182	22.551	0.050	0.206	100.607

APPENDIX E. ELECTRON MICROPROBE ANALYSES OF FELDSPARS (CONTINUED)

Sample	**Point**	**SiO_2**	**MgO**	**K_2O**	**TiO_2**	**Na_2O**	**P_2O_5**	**CaO**	**FeO**	**Al_2O_3**	**MnO**	**BaO**	**Total**
JM-18-M2-KK	1	65.200	0.000	1.591	0.000	9.011	0.000	2.547	0.162	22.409	0.063	0.061	101.044
Plagioclase 4	2	64.468	0.000	1.368	0.000	8.875	0.000	2.712	0.126	22.640	0.021	0.098	100.308
Rim to Rim	3	64.682	0.000	1.305	0.113	8.989	0.000	2.801	0.152	22.813	0.000	0.124	100.979
	4	63.830	0.021	1.053	0.032	9.116	0.028	2.707	0.138	22.227	0.000	0.136	99.288
	5	64.001	0.000	1.114	0.113	9.099	0.028	2.999	0.233	21.986	0.000	0.139	99.712
	6	63.982	0.000	1.209	0.000	9.012	0.005	2.874	0.140	22.346	0.000	0.104	99.672
	7	64.445	0.005	1.173	0.016	9.027	0.000	2.937	0.160	22.794	0.040	0.166	100.763
	8	64.520	0.001	1.193	0.072	9.042	0.008	2.984	0.192	22.588	0.000	0.139	100.739
	9	64.757	0.000	1.162	0.008	9.078	0.000	3.059	0.179	22.976	0.000	0.132	101.351
	10	64.239	0.002	1.122	0.000	9.052	0.008	3.020	0.148	23.073	0.000	0.124	100.788
	11	63.813	0.000	1.124	0.000	9.111	0.013	3.148	0.060	22.478	0.000	0.118	99.865
	12	63.998	0.008	1.276	0.008	8.894	0.025	3.167	0.183	23.001	0.037	0.173	100.770
	13	64.490	0.000	1.514	0.064	8.898	0.028	2.769	0.094	22.303	0.032	0.182	100.374
	14	62.633	0.000	1.517	0.000	8.838	0.008	2.910	0.094	22.667	0.000	0.160	98.827
	15	64.393	0.000	1.467	0.000	8.891	0.000	2.968	0.161	22.674	0.037	0.124	100.715

Sample	**Point**	**SiO_2**	**MgO**	**K_2O**	**TiO_2**	**Na_2O**	**P_2O_5**	**CaO**	**FeO**	**Al_2O_3**	**MnO**	**BaO**	**Total**
JM-18-M2-KK	1	64.841	0.000	8.952	0.000	5.011	0.027	0.269	0.139	20.029	0.045	1.724	101.037
Sanidine 5	2	64.863	0.001	8.912	0.025	5.167	0.008	0.213	0.113	19.942	0.000	1.222	100.466
Rim to Rim	3	65.164	0.000	8.971	0.016	5.107	0.000	0.222	0.138	19.945	0.074	1.224	100.861
	4	64.817	0.000	8.806	0.000	5.237	0.000	0.282	0.081	19.864	0.047	1.145	100.279
	5	65.403	0.008	8.649	0.032	5.277	0.007	0.249	0.088	19.509	0.011	0.898	100.131
	7	64.839	0.000	9.090	0.049	4.970	0.025	0.213	0.128	20.152	0.000	1.460	100.926
	8	65.287	0.000	8.846	0.024	4.885	0.000	0.213	0.062	19.699	0.000	1.462	100.478
	9	64.997	0.000	8.919	0.073	5.289	0.007	0.229	0.161	19.050	0.008	1.159	99.892
	10	63.527	0.000	8.947	0.121	5.148	0.000	0.248	0.140	19.922	0.000	1.203	99.256
	11	64.967	0.000	9.040	0.000	4.976	0.000	0.217	0.161	19.839	0.000	1.145	100.345
	12	65.096	0.000	8.985	0.089	5.140	0.002	0.264	0.059	19.317	0.000	0.745	99.697
	13	64.521	0.003	9.030	0.218	5.104	0.007	0.218	0.083	20.019	0.042	1.382	100.627
	14	64.829	0.000	8.989	0.089	5.109	0.005	0.244	0.125	19.900	0.000	1.278	100.568
	15	65.159	0.000	8.708	0.081	5.316	0.000	0.280	0.087	20.131	0.055	1.221	101.038

APPENDIX E. ELECTRON MICROPROBE ANALYSES OF FELDSPARS (CONTINUED)

Sample	Point	SiO_2	MgO	K_2O	TiO_2	Na_2O	P_2O_5	CaO	FeO	Al_2O_3	MnO	BaO	Total
JM-18-M2-KK	1	63.495	0.000	1.186	0.000	8.851	0.003	3.507	0.166	23.257	0.061	0.126	100.652
Plagioclase 7	3	64.038	0.000	1.161	0.048	8.917	0.018	3.321	0.206	22.972	0.048	0.296	101.025
Rim to Rim	4	64.099	0.000	1.232	0.000	8.914	0.000	3.254	0.270	22.979	0.018	0.222	100.988
	5	64.322	0.012	1.235	0.032	8.999	0.040	3.075	0.180	23.031	0.000	0.261	101.187
	6	63.452	0.010	1.123	0.000	9.042	0.000	3.194	0.168	23.087	0.018	0.241	100.335
	7	63.237	0.000	1.060	0.040	8.977	0.000	3.175	0.172	22.388	0.000	0.208	99.257
	8	64.047	0.011	1.156	0.089	8.959	0.053	3.166	0.130	22.885	0.024	0.216	100.736
	9	64.278	0.007	1.134	0.089	8.765	0.025	3.243	0.188	22.497	0.029	0.285	100.540
	10	64.483	0.000	1.187	0.000	8.943	0.025	3.070	0.203	22.952	0.013	0.230	101.106
	11	64.042	0.023	1.147	0.000	8.790	0.005	3.280	0.177	22.847	0.000	0.220	100.531
	12	63.983	0.002	1.205	0.024	8.951	0.020	3.343	0.161	23.084	0.016	0.193	100.982
	13	63.555	0.000	1.232	0.049	8.803	0.008	3.261	0.138	23.132	0.000	0.277	100.455
	14	63.497	0.010	1.234	0.000	8.629	0.000	3.238	0.147	22.512	0.026	0.229	99.522
	15	62.478	0.000	1.204	0.000	8.694	0.000	3.334	0.195	22.933	0.000	0.176	99.014

Sample	Point	SiO_2	MgO	K_2O	TiO_2	Na_2O	P_2O_5	CaO	FeO	Al_2O_3	MnO	BaO	Total
JM-18-M2-KK	1	64.273	0.000	1.701	0.048	8.815	0.030	2.542	0.220	22.399	0.058	0.187	100.273
Plagioclase 8	2	64.636	0.014	1.644	0.000	8.976	0.000	2.559	0.201	22.105	0.021	0.214	100.370
Rim to Rim	3	64.484	0.000	1.497	0.000	9.175	0.020	2.612	0.158	22.242	0.021	0.170	100.379
	4	64.829	0.000	1.573	0.048	9.256	0.018	2.535	0.145	20.821	0.045	0.063	99.333
	5	62.557	0.000	1.120	0.000	8.834	0.000	3.485	0.203	22.667	0.019	0.084	98.969
	7	63.249	0.000	1.460	0.081	8.970	0.010	2.670	0.081	22.531	0.019	0.091	99.162
	8	64.826	0.000	1.526	0.000	9.140	0.003	2.639	0.187	22.371	0.013	0.164	100.869
	9	64.759	0.014	1.361	0.032	9.355	0.000	2.538	0.110	21.687	0.032	0.123	100.011
	10	63.213	0.000	1.776	0.000	9.010	0.008	2.370	0.149	22.082	0.048	0.112	98.768

APPENDIX E. ELECTRON MICROPROBE ANALYSES OF FELDSPARS (CONTINUED)

Sample	Point	SiO_2	MgO	K_2O	TiO_2	Na_2O	P_2O_5	CaO	FeO	Al_2O_3	MnO	BaO	Total
JM-18-M2-KK	1	65.095	0.025	1.485	0.000	9.039	0.025	2.681	0.148	22.535	0.111	0.074	101.218
Plagioclase 9	3	64.744	0.024	1.482	0.008	9.028	0.005	2.651	0.174	22.340	0.048	0.174	100.678
Rim to Rim	4	64.416	0.000	1.376	0.000	9.153	0.013	2.719	0.189	22.426	0.032	0.167	100.491
	5	64.825	0.012	1.318	0.057	9.168	0.000	2.764	0.159	22.611	0.064	0.099	101.077
	6	64.299	0.006	1.265	0.040	9.122	0.000	2.664	0.127	22.660	0.058	0.144	100.385
	7	64.308	0.015	1.318	0.000	8.999	0.000	2.670	0.134	22.490	0.034	0.158	100.126
	8	64.801	0.000	1.259	0.000	9.225	0.023	2.687	0.168	22.412	0.056	0.150	100.781
	9	64.354	0.009	1.295	0.000	9.209	0.005	2.679	0.158	22.758	0.042	0.176	100.685
	10	64.722	0.000	1.206	0.049	9.344	0.000	2.648	0.163	22.504	0.000	0.145	100.781
	11	64.530	0.007	1.315	0.057	8.990	0.005	2.621	0.112	21.210	0.082	0.125	99.054
	12	64.882	0.001	1.325	0.057	8.958	0.025	2.712	0.200	22.230	0.029	0.119	100.538
	13	64.710	0.006	1.366	0.000	9.137	0.033	2.591	0.155	22.169	0.045	0.153	100.365
	14	64.609	0.000	1.419	0.040	9.012	0.000	2.612	0.178	22.578	0.000	0.178	100.626
	15	65.449	0.000	1.607	0.000	9.045	0.023	2.123	0.093	22.458	0.005	0.161	100.964

Sample	Point	SiO_2	MgO	K_2O	TiO_2	Na_2O	P_2O_5	CaO	FeO	Al_2O_3	MnO	BaO	Total
JM-18-M2-KK	1	64.225	0.008	1.097	0.000	8.981	0.000	3.212	0.191	23.439	0.066	0.148	101.367
Plagioclase 10	2	63.338	0.003	0.964	0.041	8.644	0.018	3.744	0.190	23.869	0.077	0.184	101.072
Rim to Rim	3	63.433	0.000	0.904	0.000	8.773	0.000	3.641	0.214	22.722	0.000	0.065	99.752
	4	63.574	0.000	0.873	0.000	8.742	0.005	3.670	0.157	23.580	0.000	0.045	100.646
	5	63.256	0.013	0.887	0.016	8.741	0.010	3.748	0.159	23.361	0.037	0.048	100.276
	6	63.041	0.000	0.906	0.057	8.957	0.015	3.621	0.173	23.480	0.000	0.123	100.373
	7	63.124	0.001	0.875	0.000	8.831	0.010	3.903	0.176	23.430	0.019	0.110	100.479
	8	63.479	0.000	0.921	0.000	8.785	0.010	3.822	0.239	23.576	0.040	0.106	100.978
	9	63.576	0.000	1.031	0.000	8.785	0.000	3.582	0.140	23.130	0.024	0.095	100.363
	10	64.263	0.000	1.314	0.000	8.987	0.000	2.810	0.216	22.526	0.000	0.077	100.193

APPENDIX E. ELECTRON MICROPROBE ANALYSES OF FELDSPARS (CONTINUED)

Sample	Point	SiO_2	MgO	K_2O	TiO_2	Na_2O	P_2O_5	CaO	FeO	Al_2O_3	MnO	BaO	Total
JM-17-PR6-KK	2	59.888	0.000	0.481	0.000	6.910	0.000	7.147	0.120	26.126	0.000	0.049	100.721
Plagioclase 0	3	58.048	0.000	0.456	0.049	7.083	0.000	6.938	0.189	25.439	0.000	0.148	98.350
Rim to Rim	4	58.206	0.006	0.451	0.000	6.928	0.000	6.929	0.168	25.782	0.052	0.000	98.522
	5	59.001	0.000	0.450	0.019	6.948	0.000	7.031	0.188	26.259	0.000	0.050	99.946
	6	58.756	0.000	0.491	0.030	7.232	0.000	6.712	0.145	25.752	0.025	0.115	99.258
	7	60.371	0.000	0.554	0.000	7.251	0.000	6.087	0.088	25.145	0.000	0.043	99.539
	8	60.418	0.020	0.530	0.000	7.535	0.000	5.978	0.063	25.147	0.047	0.044	99.782
	9	57.251	0.016	0.336	0.023	6.621	0.000	7.890	0.142	26.735	0.000	0.048	99.062

Sample	Point	SiO_2	MgO	K_2O	TiO_2	Na_2O	P_2O_5	CaO	FeO	Al_2O_3	MnO	BaO	Total
JM-17-PR6-KK	1	58.709	0.000	0.367	0.042	6.793	0.000	7.335	0.196	26.541	0.000	0.171	100.154
Plagioclase 1	2	57.653	0.000	0.330	0.000	6.073	0.000	8.199	0.307	26.912	0.000	0.073	99.547
Rim to Rim	3	55.993	0.017	0.284	0.046	5.893	0.000	9.573	0.289	28.169	0.000	0.000	100.264
	4	55.401	0.032	0.240	0.000	5.455	0.000	10.016	0.269	28.358	0.000	0.156	99.927
	5	57.792	0.000	0.362	0.076	6.446	0.000	8.024	0.107	26.697	0.025	0.160	99.689
	6	57.075	0.000	0.312	0.000	6.046	0.000	8.131	0.154	26.450	0.000	0.000	98.168
	7	56.738	0.000	0.301	0.076	6.349	0.000	8.405	0.150	26.675	0.000	0.143	98.837
	8	57.064	0.000	0.279	0.004	6.185	0.000	8.840	0.215	27.639	0.041	0.000	100.267
	9	56.365	0.021	0.264	0.038	5.988	0.000	9.204	0.197	27.810	0.014	0.201	100.102
	10	54.751	0.000	0.217	0.000	5.583	0.000	10.147	0.210	28.897	0.000	0.147	99.952
	11	56.311	0.016	0.299	0.023	5.888	0.000	9.210	0.187	27.672	0.000	0.080	99.686
	12	55.657	0.000	0.257	0.000	5.691	0.000	9.733	0.127	28.351	0.025	0.011	99.852
	13	55.625	0.000	0.297	0.015	5.875	0.000	9.225	0.305	24.671	0.000	0.000	96.013
	14	57.110	0.002	0.318	0.053	5.949	0.000	8.658	0.193	27.380	0.000	0.021	99.684
	15	58.193	0.000	0.354	0.106	6.204	0.000	8.041	0.142	26.932	0.016	0.152	100.140
	16	58.241	0.004	0.391	0.000	7.022	0.000	7.089	0.094	25.949	0.016	0.226	99.032
	17	55.123	0.004	0.255	0.015	5.397	0.000	9.781	0.229	28.302	0.019	0.000	99.125
	18	56.245	0.049	0.275	0.034	5.768	0.000	9.728	0.271	28.124	0.000	0.033	100.527
	19	56.152	0.008	0.281	0.000	5.983	0.000	9.277	0.269	28.124	0.060	0.058	100.212
	20	58.430	0.000	0.364	0.034	6.721	0.000	7.741	0.192	26.362	0.003	0.019	99.866

APPENDIX E. ELECTRON MICROPROBE ANALYSES OF FELDSPARS (CONTINUED)

Sample	Point	SiO_2	MgO	K_2O	TiO_2	Na_2O	P_2O_5	CaO	FeO	Al_2O_3	MnO	BaO	Total
JM-17-PR6-KK	1	58.453	0.009	0.355	0.121	6.624	0.000	8.089	0.159	26.559	0.025	0.010	100.404
Plagioclase 2	2	57.457	0.004	0.343	0.061	6.694	0.000	7.730	0.146	26.203	0.016	0.054	98.708
Rim to Core	3	59.742	0.000	0.445	0.000	7.225	0.000	6.750	0.100	25.411	0.000	0.011	99.684
	4	55.337	0.000	0.276	0.000	6.116	0.000	9.473	0.221	27.783	0.025	0.104	99.335
	5	57.840	0.000	0.341	0.000	6.716	0.000	8.293	0.112	26.920	0.000	0.121	100.343
	7	58.137	0.013	0.330	0.000	6.653	0.000	8.223	0.092	26.580	0.014	0.093	100.135
	8	57.392	0.008	0.301	0.000	6.176	0.000	8.657	0.195	27.327	0.000	0.000	100.056
	9	58.292	0.000	0.328	0.133	6.440	0.000	8.336	0.193	27.098	0.000	0.000	100.820
	10	56.956	0.000	0.419	0.000	5.876	0.000	8.579	0.168	27.051	0.047	0.024	99.120
	11	58.929	0.010	0.400	0.049	6.993	0.000	7.448	0.145	26.547	0.041	0.252	100.814
	12	58.299	0.006	0.353	0.042	6.726	0.000	8.150	0.103	26.774	0.000	0.030	100.483
	13	56.939	0.022	0.310	0.019	6.047	0.000	9.110	0.159	27.880	0.000	0.000	100.486
	14	57.112	0.000	0.297	0.000	6.341	0.000	8.730	0.153	27.719	0.063	0.106	100.521
	15	57.886	0.011	0.333	0.129	6.424	0.000	8.419	0.190	26.925	0.000	0.000	100.317
	16	58.765	0.000	0.447	0.068	7.342	0.000	6.868	0.052	25.896	0.019	0.076	99.533
	17	59.741	0.000	0.427	0.004	7.026	0.000	6.860	0.186	26.265	0.008	0.059	100.576
	18	59.214	0.012	0.441	0.000	6.948	0.000	7.077	0.117	26.069	0.000	0.087	99.965
	19	58.388	0.000	0.427	0.098	7.205	0.000	7.137	0.166	26.396	0.000	0.000	99.817
	20	57.713	0.000	0.408	0.057	6.909	0.000	7.078	0.195	26.133	0.000	0.048	98.541

APPENDIX E. ELECTRON MICROPROBE ANALYSES OF FELDSPARS (CONTINUED)

Sample	**Point**	**SiO_2**	**MgO**	**K_2O**	**TiO_2**	**Na_2O**	**P_2O_5**	**CaO**	**FeO**	**Al_2O_3**	**MnO**	**BaO**	**Total**
JM-17-PR6-KK	1	58.522	0.019	0.353	0.004	6.714	0.000	7.930	0.178	27.165	0.033	0.026	100.944
Plagioclase 4	2	58.364	0.000	0.327	0.061	6.859	0.000	8.070	0.210	26.917	0.041	0.052	100.901
Rim to Rim	4	54.358	0.020	0.246	0.000	5.742	0.000	9.848	0.205	28.361	0.016	0.032	98.828
	5	55.766	0.016	0.272	0.000	5.675	0.000	9.656	0.183	28.302	0.008	0.058	99.936
	6	56.800	0.016	0.278	0.053	5.871	0.000	9.419	0.313	27.978	0.000	0.010	100.738
	7	55.111	0.033	0.226	0.000	5.635	0.000	10.405	0.294	28.764	0.000	0.000	100.468
	9	56.124	0.029	0.256	0.000	5.840	0.000	9.772	0.195	28.227	0.025	0.028	100.496
	10	53.737	0.017	0.223	0.000	5.148	0.000	10.305	0.351	28.392	0.000	0.000	98.173
	11	58.535	0.000	0.353	0.023	6.595	0.000	8.077	0.157	26.906	0.019	0.025	100.690
	12	57.828	0.000	0.315	0.000	6.417	0.000	8.490	0.205	27.207	0.003	0.026	100.491
	13	57.047	0.015	0.294	0.000	5.941	0.000	9.056	0.237	27.744	0.014	0.238	100.586
	14	57.128	0.000	0.304	0.072	6.125	0.000	8.844	0.179	27.598	0.000	0.099	100.349
	15	56.832	0.015	0.296	0.045	6.117	0.000	9.103	0.193	27.984	0.000	0.043	100.628
	16	57.378	0.016	0.320	0.000	6.099	0.000	8.955	0.168	27.438	0.041	0.134	100.549
	17	57.837	0.000	0.314	0.000	6.279	0.000	8.780	0.234	27.580	0.000	0.050	101.074
	18	55.202	0.018	0.235	0.027	5.382	0.000	10.734	0.239	28.952	0.025	0.000	100.814
	19	55.677	0.000	0.253	0.000	5.617	0.000	10.329	0.227	28.572	0.022	0.121	100.818
	20	56.297	0.014	0.267	0.030	5.738	0.000	9.966	0.181	28.510	0.000	0.071	101.074

Sample	**Point**	**SiO_2**	**MgO**	**K_2O**	**TiO_2**	**Na_2O**	**P_2O_5**	**CaO**	**FeO**	**Al_2O_3**	**MnO**	**BaO**	**Total**
JM-17-PR6-KK	1	58.029	0.000	0.371	0.000	6.466	0.000	7.626	0.177	26.825	0.000	0.000	99.494
Plagioclase 5a	2	59.846	0.005	0.552	0.072	7.178	0.000	5.927	0.060	25.189	0.000	0.000	98.829
Rim to Rim	3	59.400	0.007	0.475	0.000	6.992	0.000	6.751	0.082	25.730	0.022	0.009	99.468
	4	59.424	0.000	0.506	0.000	7.318	0.000	6.607	0.160	25.830	0.000	0.073	99.918
	5	58.703	0.020	0.472	0.000	6.888	0.000	6.953	0.134	26.222	0.074	0.206	99.672
	6	58.685	0.000	0.458	0.083	6.911	0.000	7.207	0.166	25.976	0.011	0.018	99.515
	7	58.013	0.000	0.445	0.000	6.980	0.000	7.089	0.164	26.131	0.011	0.151	98.984
	9	59.402	0.000	0.471	0.000	6.841	0.000	7.021	0.157	26.026	0.008	0.022	99.948
	10	58.895	0.000	0.476	0.000	6.924	0.000	6.978	0.177	26.283	0.011	0.000	99.744
	11	60.111	0.007	0.512	0.007	7.469	0.000	6.321	0.055	25.377	0.000	0.241	100.100

APPENDIX E. ELECTRON MICROPROBE ANALYSES OF FELDSPARS (CONTINUED)

Sample	**Point**	**SiO_2**	**MgO**	**K_2O**	**TiO_2**	**Na_2O**	**P_2O_5**	**CaO**	**FeO**	**Al_2O_3**	**MnO**	**BaO**	**Total**
JM-17-PR6-KK	16	58.663	0.000	0.384	0.046	6.822	0.000	6.887	0.119	26.697	0.005	0.000	99.623
Plagioclase 5b	17	59.474	0.001	0.448	0.000	6.882	0.000	6.338	0.194	26.074	0.033	0.013	99.457
Rim to Rim	18	56.532	0.000	0.255	0.012	5.585	0.000	9.716	0.310	29.077	0.000	0.000	101.487
	19	55.389	0.002	0.228	0.057	5.348	0.000	10.159	0.247	29.073	0.033	0.153	100.689
	20	56.741	0.008	0.283	0.000	5.879	0.000	9.128	0.216	27.964	0.000	0.000	100.219
	21	56.099	0.000	0.256	0.000	5.664	0.000	9.838	0.230	28.583	0.006	0.000	100.676
	22	55.744	0.012	0.254	0.000	5.770	0.000	10.000	0.219	28.769	0.000	0.000	100.768
	23	55.728	0.000	0.256	0.000	5.735	0.003	10.033	0.182	28.425	0.000	0.000	100.362
	24	55.756	0.012	0.251	0.000	5.536	0.000	10.033	0.265	28.697	0.000	0.049	100.599
	25	55.655	0.028	0.266	0.065	5.566	0.000	9.479	0.126	28.277	0.000	0.026	99.488
	27	55.577	0.011	0.293	0.000	5.683	0.000	9.669	0.224	27.263	0.000	0.041	98.761
	28	56.199	0.015	0.306	0.011	6.189	0.000	9.222	0.221	27.698	0.039	0.142	100.042
	29	57.590	0.008	0.339	0.030	6.689	0.000	8.181	0.139	26.955	0.000	0.052	99.983
	30	58.582	0.013	0.417	0.008	6.863	0.000	7.387	0.151	25.958	0.000	0.000	99.379

APPENDIX E. ELECTRON MICROPROBE ANALYSES OF FELDSPARS (CONTINUED)

Sample	**Point**	**SiO_2**	**MgO**	**K_2O**	**TiO_2**	**Na_2O**	**P_2O_5**	**CaO**	**FeO**	**Al_2O_3**	**MnO**	**BaO**	**Total**
JM-17-ERN3-KK	1	63.265	0.000	1.200	0.102	8.812	0.000	2.890	0.097	21.984	0.014	0.000	98.364
Plagioclase 1	2	64.335	0.000	1.184	0.000	8.574	0.000	3.015	0.075	22.191	0.008	0.063	99.445
Rim to Rim	3	64.091	0.000	1.227	0.000	8.998	0.000	2.816	0.150	21.846	0.000	0.037	99.165
	4	63.904	0.000	1.217	0.015	9.172	0.000	2.877	0.157	22.285	0.003	0.069	99.699
	5	64.131	0.005	1.227	0.000	8.941	0.000	2.904	0.141	22.337	0.000	0.000	99.686
	6	63.689	0.003	1.265	0.095	9.237	0.000	2.713	0.153	22.362	0.033	0.147	99.697
	7	64.186	0.000	1.277	0.080	9.039	0.000	2.682	0.147	22.220	0.000	0.000	99.631
	8	63.677	0.001	1.223	0.004	8.724	0.000	2.734	0.127	22.461	0.000	0.039	98.990
	9	64.508	0.000	1.335	0.019	8.748	0.000	2.585	0.080	21.739	0.011	0.166	99.191
	10	64.381	0.000	1.336	0.000	9.230	0.000	2.578	0.157	22.071	0.000	0.000	99.753
	11	63.994	0.000	1.285	0.042	9.052	0.000	2.658	0.179	22.016	0.000	0.000	99.226
	12	64.033	0.000	1.347	0.000	9.186	0.000	2.610	0.118	22.110	0.000	0.026	99.430
	13	64.301	0.000	1.256	0.000	8.914	0.000	2.630	0.091	21.718	0.022	0.000	98.932
	14	64.227	0.010	1.307	0.000	9.170	0.000	2.685	0.117	22.187	0.000	0.160	99.863
	15	63.806	0.000	1.237	0.042	8.897	0.000	2.827	0.111	22.445	0.000	0.007	99.372
	16	63.636	0.000	1.215	0.000	8.734	0.000	3.000	0.103	22.232	0.014	0.045	98.979
	17	63.339	0.000	1.201	0.000	8.826	0.000	2.985	0.080	22.499	0.000	0.058	98.988
	18	62.666	0.000	1.206	0.027	8.873	0.000	2.815	0.096	22.330	0.030	0.021	98.064
	19	63.243	0.002	1.228	0.000	8.917	0.000	2.910	0.097	21.715	0.000	0.022	98.134

APPENDIX E. ELECTRON MICROPROBE ANALYSES OF FELDSPARS (CONTINUED)

Sample	Point	SiO_2	MgO	K_2O	TiO_2	Na_2O	P_2O_5	CaO	FeO	Al_2O_3	MnO	BaO	Total
JM-17-ERN3-KK	1	64.078	0.000	1.216	0.080	8.900	0.000	2.826	0.133	21.898	0.000	0.037	99.168
Plagioclase 2	2	64.199	0.002	1.182	0.038	8.920	0.000	2.811	0.214	22.345	0.000	0.043	99.754
Rim to Rim	3	63.772	0.006	1.170	0.034	8.697	0.000	2.884	0.105	22.304	0.030	0.054	99.056
	4	63.609	0.000	1.198	0.148	8.845	0.000	2.860	0.120	22.494	0.000	0.121	99.395
	5	64.106	0.018	1.174	0.000	9.019	0.000	2.877	0.096	22.278	0.011	0.028	99.607
	6	63.909	0.000	1.142	0.000	8.587	0.000	2.931	0.211	22.353	0.008	0.103	99.244
	7	64.196	0.002	1.156	0.000	8.649	0.000	2.894	0.103	22.247	0.000	0.000	99.247
	8	65.700	0.006	1.264	0.077	9.010	0.000	2.672	0.113	22.841	0.000	0.036	101.719
	9	63.657	0.010	1.343	0.042	9.225	0.000	2.546	0.124	22.179	0.000	0.006	99.132
	10	64.384	0.006	1.298	0.080	9.232	0.000	2.550	0.145	21.939	0.000	0.000	99.634
	11	64.426	0.028	1.262	0.030	8.807	0.000	2.656	0.073	22.098	0.052	0.021	99.453
	13	64.410	0.007	1.295	0.072	9.077	0.000	2.714	0.150	22.452	0.000	0.000	100.177
	14	62.979	0.000	1.257	0.015	8.788	0.000	2.738	0.083	22.246	0.008	0.000	98.114
	16	63.982	0.000	1.213	0.000	9.286	0.000	2.739	0.058	22.204	0.011	0.000	99.493
	17	64.120	0.000	1.303	0.000	9.006	0.000	2.691	0.102	22.261	0.055	0.000	99.538
	18	64.224	0.000	1.409	0.000	9.086	0.000	2.382	0.192	21.749	0.000	0.048	99.090
	19	63.079	0.008	1.256	0.011	8.807	0.000	2.769	0.153	22.331	0.022	0.071	98.507
	20	63.657	0.000	1.204	0.000	9.026	0.000	2.859	0.182	22.122	0.041	0.000	99.091

APPENDIX E. ELECTRON MICROPROBE ANALYSES OF FELDSPARS (CONTINUED)

Sample	Point	SiO_2	MgO	K_2O	TiO_2	Na_2O	P_2O_5	CaO	FeO	Al_2O_3	MnO	BaO	Total
JM-17-ERN3-KK	1	64.169	0.000	1.241	0.011	8.914	0.000	2.803	0.063	22.251	0.000	0.078	99.530
Plagioclase 3	2	64.090	0.008	1.234	0.011	8.494	0.000	2.711	0.085	22.375	0.011	0.036	99.055
Rim to Rim	3	64.218	0.000	1.237	0.000	8.778	0.000	2.785	0.111	22.275	0.003	0.000	99.407
	4	64.659	0.000	1.285	0.130	8.752	0.000	2.708	0.090	21.918	0.000	0.000	99.542
	5	64.298	0.000	1.302	0.023	8.852	0.000	2.654	0.141	22.259	0.028	0.101	99.658
	6	64.560	0.000	1.353	0.030	9.057	0.000	2.608	0.073	22.268	0.008	0.000	99.957
	7	64.421	0.024	1.283	0.000	8.661	0.000	2.697	0.125	22.208	0.044	0.177	99.640
	8	64.464	0.000	1.249	0.099	8.984	0.000	2.730	0.175	22.329	0.000	0.000	100.030
	9	64.186	0.012	1.256	0.107	8.801	0.000	2.734	0.060	21.340	0.028	0.077	98.601
	10	63.724	0.000	1.250	0.004	8.816	0.000	2.737	0.219	22.194	0.050	0.129	99.123
	11	64.618	0.000	1.357	0.046	8.817	0.000	2.570	0.075	22.188	0.019	0.000	99.690
	12	63.715	0.008	1.160	0.000	8.605	0.000	3.049	0.114	21.919	0.017	0.060	98.647
	13	64.254	0.000	1.257	0.000	8.820	0.000	2.853	0.178	21.745	0.000	0.052	99.159
	14	63.412	0.000	1.288	0.008	8.835	0.000	2.854	0.067	21.998	0.008	0.000	98.470
	15	63.808	0.016	1.213	0.107	8.628	0.000	2.913	0.114	21.882	0.017	0.013	98.711
	16	64.174	0.004	1.239	0.000	8.924	0.000	2.843	0.168	22.330	0.036	0.043	99.761
	17	64.489	0.015	1.242	0.030	8.854	0.000	2.769	0.172	22.418	0.003	0.000	99.992
	18	64.003	0.000	1.262	0.148	8.749	0.000	2.719	0.174	22.582	0.000	0.119	99.756
	19	64.241	0.006	1.268	0.015	8.646	0.000	2.727	0.098	22.159	0.030	0.121	99.311
	20	64.239	0.016	1.230	0.000	8.763	0.000	2.752	0.164	22.045	0.000	0.026	99.235

APPENDIX E. ELECTRON MICROPROBE ANALYSES OF FELDSPARS (CONTINUED)

Sample	Point	SiO_2	MgO	K_2O	TiO_2	Na_2O	P_2O_5	CaO	FeO	Al_2O_3	MnO	BaO	Total
JM-17-ERN3-KK	2	65.208	0.000	11.665	0.000	3.510	0.000	0.165	0.078	19.465	0.011	0.167	100.269
Sanidine 4	3	64.815	0.000	11.597	0.000	3.609	0.000	0.168	0.100	18.906	0.055	0.000	99.250
Rim to Rim	4	64.893	0.008	11.753	0.034	3.624	0.000	0.149	0.081	19.320	0.011	0.021	99.894
	5	64.044	0.000	11.791	0.000	3.469	0.000	0.143	0.053	19.265	0.003	0.144	98.912
	6	64.898	0.010	11.765	0.092	3.523	0.000	0.147	0.149	19.315	0.000	0.071	99.970
	7	64.821	0.002	11.810	0.000	3.647	0.000	0.155	0.159	19.235	0.000	0.000	99.829
	8	64.642	0.007	11.724	0.004	3.389	0.000	0.153	0.080	19.427	0.000	0.000	99.426
	9	63.682	0.000	11.686	0.000	3.566	0.000	0.146	0.076	19.592	0.000	0.126	98.874
	11	65.029	0.008	11.897	0.042	3.629	0.000	0.169	0.094	19.281	0.006	0.079	100.234
	12	65.158	0.002	11.864	0.000	3.516	0.000	0.174	0.072	19.275	0.017	0.060	100.138
	13	64.972	0.000	11.782	0.000	3.617	0.000	0.147	0.135	19.241	0.000	0.000	99.894
	14	64.910	0.000	11.822	0.008	3.456	0.000	0.151	0.062	19.400	0.011	0.000	99.820
	15	64.970	0.014	11.858	0.057	3.634	0.000	0.163	0.164	19.207	0.019	0.000	100.086
	16	64.723	0.018	11.805	0.057	3.545	0.000	0.183	0.115	19.368	0.019	0.141	99.974
	17	64.845	0.000	11.802	0.027	3.424	0.000	0.190	0.158	19.224	0.003	0.000	99.673
	18	64.819	0.009	11.808	0.019	3.475	0.000	0.171	0.042	19.187	0.000	0.043	99.573
	19	65.123	0.000	11.768	0.042	3.463	0.000	0.157	0.103	19.286	0.055	0.013	100.010
	20	64.601	0.000	11.742	0.088	3.602	0.000	0.154	0.017	19.280	0.036	0.043	99.563
	21	64.445	0.000	11.815	0.038	3.568	0.000	0.161	0.091	18.791	0.000	0.068	98.977
	22	64.452	0.009	11.719	0.050	3.485	0.000	0.154	0.049	19.484	0.000	0.028	99.430
	23	65.130	0.001	11.760	0.000	3.270	0.000	0.151	0.000	19.018	0.000	0.009	99.339
	24	64.555	0.000	11.884	0.061	3.364	0.000	0.147	0.127	18.938	0.000	0.028	99.104

APPENDIX E. ELECTRON MICROPROBE ANALYSES OF FELDSPARS (CONTINUED)

Sample	Point	SiO_2	MgO	K_2O	TiO_2	Na_2O	P_2O_5	CaO	FeO	Al_2O_3	MnO	BaO	Total
JM-17-I2-KK	1	67.787	0.000	6.465	0.074	7.002	0.000	0.212	0.161	19.574	0.000	0.006	101.281
Anorthoclase 1	2	67.449	0.000	7.046	0.031	6.573	0.000	0.218	0.200	19.653	0.012	0.075	101.257
Rim to Rim	4	67.397	0.000	7.048	0.000	6.298	0.000	0.231	0.156	19.367	0.000	0.000	100.497
	5	67.055	0.013	7.235	0.000	6.105	0.000	0.217	0.183	19.226	0.000	0.000	100.034
	6	67.337	0.005	7.227	0.000	6.377	0.000	0.224	0.175	19.475	0.019	0.000	100.839
	7	67.663	0.006	7.132	0.023	6.227	0.000	0.205	0.166	19.392	0.000	0.051	100.865
	8	66.842	0.000	7.346	0.113	6.050	0.000	0.194	0.170	19.546	0.052	0.000	100.313
	9	66.444	0.000	7.038	0.105	6.702	0.000	0.254	0.138	18.049	0.000	0.085	98.815
	10	67.121	0.006	6.719	0.101	6.390	0.000	0.283	0.222	19.657	0.000	0.043	100.542

Sample	Point	SiO_2	MgO	K_2O	TiO_2	Na_2O	P_2O_5	CaO	FeO	Al_2O_3	MnO	BaO	Total
JM-17-I2-KK	1	68.402	0.006	6.820	0.109	5.806	0.000	0.173	0.338	17.729	0.000	0.143	99.526
Anorthoclase 2	2	67.265	0.000	6.985	0.000	6.228	0.000	0.242	0.201	18.933	0.022	0.006	99.882
Rim to Core	3	67.236	0.019	7.006	0.000	6.108	0.000	0.234	0.224	19.239	0.000	0.000	100.066
	4	67.047	0.004	7.014	0.062	6.171	0.000	0.219	0.204	18.953	0.010	0.023	99.707
	5	67.475	0.023	6.935	0.000	6.399	0.000	0.233	0.172	19.411	0.000	0.150	100.798

Sample	Point	SiO_2	MgO	K_2O	TiO_2	Na_2O	P_2O_5	CaO	FeO	Al_2O_3	MnO	BaO	Total
JM-17-I2-KK	1	66.730	0.000	7.193	0.000	6.214	0.000	0.187	0.196	19.243	0.000	0.000	99.763
Anorthoclase 7	2	67.236	0.000	7.196	0.000	6.106	0.000	0.200	0.167	19.226	0.005	0.000	100.136
Core to Rim	3	67.536	0.000	7.250	0.086	6.179	0.000	0.202	0.224	19.279	0.053	0.007	100.816
	4	67.611	0.005	7.251	0.031	6.175	0.000	0.218	0.229	19.497	0.068	0.000	101.085
	5	67.530	0.000	6.383	0.000	6.873	0.000	0.294	0.132	19.634	0.000	0.049	100.895

APPENDIX E. ELECTRON MICROPROBE ANALYSES OF FELDSPARS (CONTINUED)

Sample	Point	SiO_2	MgO	K_2O	TiO_2	Na_2O	P_2O_5	CaO	FeO	Al_2O_3	MnO	BaO	Total
JM-17-I2-KK	13	67.182	0.000	6.654	0.109	6.671	0.000	0.190	0.203	19.200	0.000	0.000	100.209
Anorthoclase 13	14	67.063	0.000	7.119	0.019	6.379	0.000	0.217	0.162	19.466	0.020	0.124	100.569
Rim to Rim	15	67.546	0.000	7.193	0.000	6.187	0.000	0.220	0.158	19.435	0.015	0.000	100.754
	16	67.488	0.000	7.326	0.000	6.157	0.000	0.210	0.169	19.047	0.020	0.023	100.440
	17	66.022	0.001	7.223	0.000	5.840	0.000	0.195	0.178	18.881	0.000	0.195	98.535
	18	67.177	0.007	7.323	0.000	6.524	0.000	0.212	0.167	19.516	0.000	0.051	100.977
	19	66.524	0.000	7.127	0.054	5.918	0.000	0.192	0.142	19.379	0.064	0.000	99.400
	21	67.385	0.000	7.305	0.133	6.308	0.000	0.202	0.186	19.320	0.019	0.000	100.858
	22	67.382	0.000	6.995	0.000	6.215	0.000	0.212	0.167	19.247	0.000	0.000	100.218

Sample	Point	SiO_2	MgO	K_2O	TiO_2	Na_2O	P_2O_5	CaO	FeO	Al_2O_3	MnO	BaO	Total
JM-17-I2-KK	23	66.540	0.000	6.975	0.039	6.259	0.000	0.240	0.159	18.490	0.010	0.000	98.712
Anorthoclase 23	24	67.249	0.000	7.261	0.000	6.209	0.000	0.220	0.178	19.236	0.000	0.049	100.402
Rim to Rim	25	66.451	0.000	7.322	0.000	6.105	0.000	0.211	0.208	19.679	0.000	0.000	99.976
	26	67.370	0.000	7.677	0.000	5.894	0.000	0.182	0.126	19.431	0.018	0.010	100.708
	27	67.064	0.000	7.363	0.000	6.188	0.000	0.211	0.217	18.862	0.000	0.000	99.905
	28	67.368	0.000	7.436	0.000	6.036	0.000	0.197	0.231	19.495	0.000	0.000	100.763
	29	67.438	0.000	7.316	0.000	5.868	0.000	0.182	0.178	19.119	0.000	0.000	100.101
	30	67.151	0.000	7.241	0.000	6.240	0.000	0.201	0.230	19.348	0.000	0.000	100.411
	31	66.633	0.011	7.179	0.000	6.069	0.000	0.229	0.206	19.264	0.000	0.000	99.591
	32	67.114	0.007	7.428	0.023	6.123	0.000	0.194	0.180	19.354	0.076	0.010	100.509

APPENDIX F. ELECTRON MICROPROBE SPOT ANALYSES OF MAFIC AND OXIDE MINERALS. UNRELIABLE DATA NOT INCLUDED IN RESULTS HAVE BEEN OMITTED.

Sample	**Point**	**SiO_2**	**MgO**	**K_2O**	**TiO_2**	**Na_2O**	**P_2O_5**	**CaO**	**FeO**	**Al_2O_3**	**MnO**	**F**	**BaO**	**SO_3**	**Cl**	**Cr_2O_3**	**Nb_2O_5**	**Total**	**Mineral**
JM-17-O2-KK-1	6	37.765	14.921	7.627	4.266	0.513	0.000	0.201	15.178	14.963	0.184	0.195	0.860	0.062	0.133	0.000	0.000	96.756	Biotite
	7	38.130	14.520	8.054	4.158	0.784	0.000	0.055	15.601	15.662	0.306	2.641	0.853	0.089	0.138	0.025	0.000	99.873	Biotite
	8	35.696	13.656	7.302	4.292	0.426	0.000	0.283	18.501	14.319	0.616	0.720	0.602	0.059	0.106	0.000	0.006	96.257	Biotite
	9	37.834	14.409	7.878	4.062	0.389	0.000	0.199	14.477	14.935	0.287	0.617	0.517	0.058	0.119	0.000	0.032	95.526	Biotite
	10	0.087	0.140	0.005	0.000	0.221	41.868	58.634	1.279	0.004	0.398	3.275	0.115	0.336	0.894	0.000	0.045	105.720	Apatite
	11	0.128	0.143	0.003	0.100	0.205	41.471	58.570	1.894	0.000	0.314	3.239	0.023	0.190	0.885	0.003	0.000	105.604	Apatite
	12	0.037	1.337	0.000	35.161	0.151	0.000	0.012	56.071	0.169	2.006	0.000	0.144	0.011	0.008	0.088	0.116	95.309	Ilmenite
	13	0.038	1.354	0.000	37.891	0.005	0.000	0.026	55.425	0.183	1.815	0.052	0.080	0.000	0.007	0.044	0.129	97.025	Ilmenite
	14	33.518	0.002	0.007	0.008	0.015	0.000	0.029	0.016	0.000	0.035	0.238	0.143	0.003	0.006	0.026	0.000	33.945	Zircon
	15	0.084	0.600	0.000	5.572	0.000	0.016	0.026	84.087	2.290	0.752	0.000	0.006	0.000	0.001	0.034	0.000	93.468	Magnetite
	16	0.075	0.634	0.001	5.588	0.000	0.054	0.012	85.683	2.132	0.854	0.000	0.000	0.010	0.000	0.096	0.048	95.187	Magnetite
	17	0.086	0.976	0.000	37.174	0.000	0.002	0.021	52.923	0.316	1.536	0.000	0.224	0.002	0.002	0.104	0.098	93.464	Ilmenite
	18	0.088	0.518	0.000	8.485	0.000	0.000	0.014	81.468	2.317	1.254	0.000	0.171	0.000	0.000	0.000	0.005	94.320	Magnetite
	19	0.071	0.829	0.000	5.379	0.000	0.000	0.005	84.040	2.441	1.217	0.000	0.000	0.000	0.000	0.089	0.000	94.071	Magnetite
	20	0.037	0.836	0.000	5.436	0.012	0.000	0.001	85.590	2.022	1.318	0.000	0.092	0.018	0.000	0.104	0.012	95.478	Magnetite
	26	0.138	0.205	0.056	0.000	0.191	41.934	58.387	0.914	0.000	0.396	3.786	0.037	0.285	0.740	0.000	0.035	105.343	Apatite

Sample	**Point**	**SiO_2**	**MgO**	**K_2O**	**TiO_2**	**Na_2O**	**P_2O_5**	**CaO**	**FeO**	**Al_2O_3**	**MnO**	**F**	**BaO**	**SO_3**	**Cl**	**Cr_2O_3**	**Nb_2O_5**	**Total**	**Mineral**
JM-17-O2-KK-2	6	37.595	14.413	8.024	3.823	0.618	0.000	0.144	15.835	14.793	0.355	0.324	0.678	0.083	0.111	0.000	0.004	96.639	Biotite
	7	37.103	14.309	8.647	4.529	0.670	0.000	0.046	16.057	14.776	0.398	0.381	0.937	0.048	0.125	0.010	0.000	97.848	Biotite
	8	36.566	14.000	8.179	4.066	0.640	0.000	0.128	17.022	14.705	0.550	0.433	0.772	0.056	0.102	0.071	0.020	97.105	Biotite
	9	0.218	0.104	0.009	0.000	0.165	41.428	58.714	0.412	0.019	0.255	3.444	0.037	0.116	1.077	0.057	0.017	104.379	Apatite
	10	0.198	0.076	0.003	0.008	0.137	41.372	59.064	0.429	0.002	0.273	3.220	0.000	0.142	0.657	0.000	0.037	104.114	Apatite
	11	0.073	1.432	0.000	37.479	0.000	0.000	0.007	53.017	0.311	2.730	0.027	0.118	0.003	0.000	0.005	0.191	95.382	Ilmenite
	12	0.044	1.390	0.000	38.958	0.017	0.000	0.021	53.105	0.291	2.544	0.000	0.000	0.002	0.000	0.000	0.184	96.556	Ilmenite
	13	0.065	1.386	0.010	38.115	0.000	0.000	0.027	53.624	0.257	2.724	0.000	0.256	0.000	0.000	0.000	0.192	96.656	Ilmenite
	14	0.070	1.477	0.008	38.636	0.038	0.013	0.001	55.082	0.158	2.867	0.000	0.134	0.000	0.000	0.059	0.204	98.747	Ilmenite

Sample	**Point**	**SiO_2**	**MgO**	**K_2O**	**TiO_2**	**Na_2O**	**P_2O_5**	**CaO**	**FeO**	**Al_2O_3**	**MnO**	**F**	**BaO**	**SO_3**	**Cl**	**Cr_2O_3**	**Nb_2O_5**	**Total**	**Mineral**
JM-17-O2-KK-3	10	38.301	13.853	8.333	4.027	0.709	0.000	0.033	15.662	15.427	0.384	0.972	0.623	0.050	0.132	0.032	0.058	98.157	Biotite
	11	37.162	14.311	8.692	3.863	0.639	0.000	0.071	15.391	14.887	0.338	0.456	0.532	0.063	0.127	0.000	0.002	96.313	Biotite
	12	37.566	14.653	8.498	4.178	0.616	0.000	0.049	15.426	15.242	0.293	0.251	0.899	0.040	0.132	0.027	0.000	97.734	Biotite
	13	37.799	14.958	8.529	4.358	0.701	0.000	0.063	14.661	15.153	0.332	0.131	1.084	0.042	0.110	0.008	0.050	97.899	Biotite
	14	0.264	1.137	0.019	5.142	0.045	0.024	0.030	80.884	2.980	1.759	0.000	0.000	0.000	0.000	0.014	0.000	92.298	Magnetite

APPENDIX F. ELECTRON MICROPROBE SPOT ANALYSES OF MAFIC AND OXIDE MINERALS (CONTINUED)

Sample	Point	SiO_2	MgO	K_2O	TiO_2	Na_2O	P_2O_5	CaO	FeO	Al_2O_3	MnO	F	BaO	SO_3	Cl	Cr_2O_3	Nb_2O_5	Total	Mineral
JM-17-O2-KK-4	3	0.178	0.128	0.013	0.008	0.158	42.419	59.954	0.432	0.014	0.335	4.803	0.000	0.106	0.067	0.055	0.000	106.633	Apatite
	4	35.746	14.031	8.295	3.619	0.626	0.033	0.039	18.698	14.324	0.303	1.211	0.963	0.034	0.093	0.000	0.000	97.484	Biotite
	5	34.875	13.065	7.951	3.949	0.545	0.000	0.000	21.844	14.180	0.539	1.449	0.734	0.054	0.112	0.088	0.000	98.750	Biotite
	6	0.068	0.784	0.000	5.324	0.002	0.000	0.006	87.447	2.410	1.210	0.000	0.070	0.009	0.000	0.005	0.002	97.337	Magnetite
	7	0.282	0.266	0.000	6.175	0.000	0.013	0.053	81.422	2.081	0.216	0.000	0.000	0.021	0.092	0.042	0.019	90.661	Magnetite
	8	0.083	0.645	0.000	5.536	0.000	0.033	0.005	85.081	2.080	1.238	0.000	0.165	0.002	0.003	0.018	0.000	94.888	Magnetite
	9	0.079	0.796	0.000	5.061	0.000	0.030	0.001	83.065	2.460	1.594	0.000	0.043	0.005	0.000	0.000	0.118	93.252	Magnetite
	10	0.042	0.729	0.000	5.590	0.009	0.012	0.000	85.064	2.047	1.277	0.000	0.104	0.001	0.000	0.012	0.027	94.914	Magnetite
	11	0.049	0.712	0.000	5.250	0.033	0.000	0.009	84.419	2.159	1.245	0.000	0.103	0.000	0.000	0.000	0.053	94.032	Magnetite
	12	0.069	0.741	0.000	5.401	0.002	0.001	0.000	83.380	2.358	1.535	0.000	0.000	0.000	0.001	0.005	0.077	93.570	Magnetite
	13	0.112	0.673	0.000	5.356	0.000	0.000	0.005	83.739	2.266	1.281	0.000	0.110	0.000	0.001	0.000	0.000	93.543	Magnetite
	14	0.094	0.719	0.000	5.355	0.000	0.000	0.021	83.595	2.250	1.314	0.000	0.025	0.000	0.000	0.071	0.000	93.444	Magnetite

Sample	Point	SiO_2	MgO	K_2O	TiO_2	Na_2O	P_2O_5	CaO	FeO	Al_2O_3	MnO	F	BaO	SO_3	Cl	Cr_2O_3	Nb_2O_5	Total	Mineral
JM-17-O2-KK-7	3	0.157	0.125	0.000	0.088	0.284	37.896	51.422	0.375	0.000	0.288	4.650	0.062	0.323	0.618	0.000	0.009	94.200	Apatite
	4	0.234	0.105	0.000	0.064	0.192	41.508	58.023	0.619	0.008	0.407	4.650	0.052	0.323	0.334	0.030	0.060	104.576	Apatite
	5	0.118	0.202	0.000	0.000	0.203	42.498	58.905	1.152	0.027	0.651	4.566	0.000	0.323	0.369	0.012	0.058	107.078	Apatite
	6	0.328	0.176	0.010	0.036	0.120	42.330	58.610	1.571	0.020	0.726	4.545	0.072	0.137	0.114	0.000	0.054	106.909	Apatite
	7	0.313	0.133	0.013	0.052	0.106	42.225	59.018	1.704	0.000	0.548	5.171	0.000	0.161	0.260	0.000	0.026	107.494	Apatite
	8	0.298	0.108	0.012	0.100	0.215	41.916	60.450	0.195	0.065	0.250	3.920	0.000	0.212	0.518	0.032	0.038	106.561	Apatite
	9	0.027	1.771	0.018	40.096	0.000	0.031	0.054	47.851	0.181	3.941	0.000	0.105	0.000	0.000	0.000	0.112	94.187	Ilmenite
	10	0.099	1.907	0.013	40.888	0.026	0.011	0.085	46.825	0.113	4.059	0.000	0.061	0.000	0.000	0.011	0.097	94.195	Ilmenite
	11	0.038	1.114	0.018	41.754	0.000	0.000	0.047	49.573	0.224	2.406	0.000	0.113	0.017	0.000	0.000	0.096	95.400	Ilmenite
	12	0.056	0.942	0.006	36.360	0.007	0.000	0.004	54.880	0.272	2.129	0.000	0.000	0.000	0.004	0.061	0.141	94.861	Ilmenite
	13	0.035	1.038	0.009	35.867	0.000	0.000	0.041	55.331	0.336	1.905	0.000	0.038	0.000	0.000	0.000	0.118	94.718	Ilmenite
	14	0.009	0.915	0.000	37.170	0.000	0.004	0.019	54.269	0.318	1.763	0.000	0.066	0.000	0.003	0.000	0.111	94.646	Ilmenite
	15	0.075	0.488	0.000	3.889	0.000	0.000	0.021	89.377	1.986	1.076	0.000	0.210	0.002	0.000	0.026	0.042	97.192	Magnetite
	16	0.069	0.459	0.000	3.618	0.000	0.000	0.035	86.977	2.174	1.194	0.000	0.000	0.000	0.000	0.105	0.000	94.631	Magnetite
	17	0.075	0.600	0.000	6.341	0.000	0.000	0.013	81.091	3.617	1.577	0.000	0.091	0.000	0.000	0.061	0.000	93.466	Magnetite
	18	0.121	0.608	0.001	9.433	0.000	0.000	0.024	76.662	3.276	1.563	0.000	0.052	0.006	0.001	0.000	0.038	91.785	Magnetite
	19	0.043	0.956	0.000	36.526	0.010	0.033	0.005	53.554	0.241	1.771	0.009	0.094	0.024	0.001	0.000	0.138	93.401	Ilmenite
	20	0.129	0.627	0.008	11.289	0.040	0.000	0.040	74.207	2.770	1.519	0.000	0.081	0.050	0.082	0.045	0.087	90.955	Magnetite

Sample	Point	SiO_2	MgO	K_2O	TiO_2	Na_2O	P_2O_5	CaO	FeO	Al_2O_3	MnO	F	BaO	SO_3	Cl	Cr_2O_3	Nb_2O_5	Total	Mineral
JM-17-O2-KK-9	7	0.122	0.121	0.000	0.128	0.130	40.941	57.243	1.402	0.022	0.428	4.444	0.045	0.213	0.985	0.026	0.068	104.225	Apatite
	8	37.058	14.940	8.229	3.928	0.779	0.000	0.104	15.074	14.617	0.276	0.195	1.098	0.051	0.121	0.000	0.000	96.361	Biotite
	9	0.223	0.268	0.000	0.389	0.185	39.900	55.124	4.336	0.153	1.125	3.952	0.006	0.089	1.005	0.000	0.038	104.902	Apatite

APPENDIX F. ELECTRON MICROPROBE SPOT ANALYSES OF MAFIC AND OXIDE MINERALS (CONTINUED)

Sample	Point	SiO_2	MgO	K_2O	TiO_2	Na_2O	P_2O_5	CaO	FeO	Al_2O_3	MnO	F	BaO	SO_3	Cl	Cr_2O_3	Nb_2O_5	Total	Mineral
JM-17-O2-KK-10	3	36.968	14.115	7.990	4.092	0.501	0.009	0.171	14.628	14.721	0.385	0.506	0.455	0.036	0.110	0.002	0.000	94.451	Biotite
	4	37.281	15.121	8.266	3.908	0.615	0.000	0.088	15.554	14.671	0.296	0.167	0.841	0.000	0.130	0.000	0.032	96.871	Biotite
	5	0.040	1.243	0.004	38.262	0.029	0.000	0.022	52.987	0.353	1.886	0.000	0.000	0.008	0.003	0.024	0.101	94.961	Ilmenite
	6	0.027	1.196	0.010	37.613	0.015	0.000	0.029	53.058	0.288	2.094	0.000	0.000	0.007	0.004	0.000	0.141	94.481	Ilmenite
	7	0.087	0.597	0.000	5.237	0.000	0.000	0.006	80.949	2.527	1.474	0.000	0.000	0.000	0.000	0.000	0.029	90.906	Magnetite
	8	0.077	0.856	0.002	5.253	0.000	0.025	0.010	82.654	2.699	1.404	0.000	0.000	0.000	0.000	0.039	0.000	93.019	Magnetite
	9	0.064	0.684	0.000	5.227	0.000	0.000	0.000	84.011	2.471	1.624	0.000	0.095	0.000	0.000	0.046	0.000	94.222	Magnetite
	10	0.096	0.730	0.006	5.678	0.000	0.000	0.013	82.320	3.694	1.603	0.000	0.037	0.000	0.000	0.000	0.015	94.192	Magnetite
	11	34.163	0.000	0.038	0.104	0.030	0.000	0.010	0.214	0.023	0.077	0.239	0.000	0.028	0.000	0.025	0.000	34.850	Zircon
	12	36.926	12.483	8.596	3.939	0.348	0.000	0.112	18.571	14.494	0.636	1.193	0.713	0.058	0.117	0.015	0.000	97.673	Biotite
	13	36.220	13.955	8.355	4.443	0.397	0.000	0.141	16.454	14.721	0.238	1.161	0.438	0.047	0.126	0.018	0.000	96.197	Biotite

APPENDIX F. ELECTRON MICROPROBE SPOT ANALYSES OF MAFIC AND OXIDE MINERALS (CONTINUED)

Sample	Point	SiO_2	MgO	K_2O	TiO_2	Na_2O	P_2O_5	CaO	FeO	Al_2O_3	MnO	F	BaO	Total	Mineral
JM-18-M2-KK-1	1	0.000	1.766	0.013	33.794	0.000	0.017	0.019	51.171	0.730	4.436	0.000	0.584	92.530	Ilmenite
	2	0.045	1.787	0.000	39.279	0.000	0.000	0.002	49.961	0.703	4.177	0.000	0.455	96.409	Ilmenite
	3	0.080	1.596	0.005	39.057	0.000	0.000	0.006	48.291	0.800	4.240	0.000	0.626	94.701	Ilmenite
	4	0.235	1.126	0.018	3.170	0.008	0.009	0.025	80.799	1.808	4.768	0.000	0.041	92.007	Magnetite

Sample	Point	SiO_2	MgO	K_2O	TiO_2	Na_2O	P_2O_5	CaO	FeO	Al_2O_3	MnO	F	BaO	Total	Mineral
JM-18-M2-KK-10	11	0.044	1.739	0.000	40.668	0.010	0.000	0.018	46.471	0.679	6.347	0.000	0.426	96.402	Ilmenite
	12	0.102	2.133	0.000	43.892	0.034	0.025	0.005	43.690	0.619	6.408	0.000	0.410	97.318	Ilmenite

APPENDIX F. ELECTRON MICROPROBE SPOT ANALYSES OF MAFIC AND OXIDE MINERALS (CONTINUED)

Sample	Point	SiO_2	MgO	K_2O	TiO_2	Na_2O	P_2O_5	CaO	FeO	Al_2O_3	MnO	F	BaO	SO_3	Cl	Cr_2O_3	Total	Mineral
JM-17-PR6-KK-1	14	45.950	13.384	0.432	1.162	1.354	0.009	10.353	14.157	9.028	0.457	0.025	0.145	0.132	0.018	0.033	96.624	Amphibole
	15	46.591	13.291	0.457	0.829	1.474	0.000	10.410	14.695	9.123	0.359	0.013	0.103	0.061	0.013	0.000	97.411	Amphibole
	16	46.452	13.322	0.454	0.900	1.305	0.000	10.353	14.061	9.070	0.422	0.026	0.000	0.085	0.002	0.003	96.444	Amphibole
	17	47.106	13.745	0.380	0.890	1.356	0.000	10.466	13.799	8.248	0.382	0.051	0.100	0.097	0.056	0.007	96.649	Amphibole
	24	36.920	13.549	8.674	3.402	0.427	0.000	0.065	16.304	15.698	0.217	0.171	0.552	0.146	0.058	0.116	96.214	Biotite
	25	38.136	13.062	8.429	3.075	0.005	0.041	0.321	14.635	15.521	0.100	0.000	0.000	0.117	0.032	0.063	93.530	Biotite
	26	36.897	14.021	8.492	3.499	0.417	0.000	0.043	15.848	15.415	0.142	0.183	0.626	0.167	0.041	0.010	95.715	Biotite
	27	36.415	12.319	8.184	3.431	0.357	0.000	0.196	16.118	16.381	0.199	0.122	0.349	0.101	0.056	0.073	94.237	Biotite

Sample	Point	SiO_2	MgO	K_2O	TiO_2	Na_2O	P_2O_5	CaO	FeO	Al_2O_3	MnO	F	BaO	SO_3	Cl	Cr_2O_3	Total	Mineral
JM-17-PR6-KK-2	7	46.728	13.245	0.478	0.977	1.395	0.000	10.490	14.959	9.109	0.546	0.102	0.053	0.074	0.042	0.040	98.186	Amphibole
	8	46.474	13.809	0.477	0.988	1.381	0.000	10.565	15.173	9.163	0.527	0.000	0.000	0.108	0.000	0.000	98.665	Amphibole
	9	46.500	15.709	0.431	1.258	1.621	0.000	10.387	11.248	10.261	0.250	0.000	0.261	0.088	0.000	0.037	98.051	Amphibole
	10	37.605	13.178	8.014	3.218	0.183	0.000	0.222	15.023	15.257	0.145	0.037	0.504	0.127	0.043	0.000	93.530	Biotite
	11	39.844	11.694	7.281	3.376	0.060	0.000	0.394	14.540	16.265	0.097	0.050	0.117	0.152	0.019	0.007	93.871	Biotite
	12	37.418	13.499	8.366	3.357	0.487	0.000	0.035	16.327	14.736	0.188	0.061	0.542	0.156	0.000	0.013	95.159	Biotite
	13	37.247	12.509	7.786	3.580	0.200	0.005	0.292	15.093	15.612	0.151	0.000	0.360	0.132	0.102	0.000	93.046	Biotite
	14	38.166	13.624	7.871	3.324	0.330	0.000	0.094	16.544	15.651	0.159	0.122	0.529	0.134	0.025	0.023	96.539	Biotite
	15	37.779	14.027	8.431	3.018	0.433	0.000	0.119	16.790	15.690	0.180	0.097	0.442	0.138	0.054	0.000	97.145	Biotite
	16	37.420	14.263	8.530	3.418	0.409	0.000	0.050	16.392	15.543	0.161	0.049	0.439	0.178	0.059	0.017	96.894	Biotite

Sample	Point	SiO_2	MgO	K_2O	TiO_2	Na_2O	P_2O_5	CaO	FeO	Al_2O_3	MnO	F	BaO	SO_3	Cl	Cr_2O_3	Total	Mineral
JM-17-PR6-KK-3	1	44.805	13.096	0.515	1.475	1.793	0.000	10.041	13.733	11.149	0.352	0.000	0.018	0.120	0.030	0.000	97.120	Amphibole
	2	45.645	14.548	0.485	1.723	1.811	0.004	10.252	12.747	10.599	0.130	0.077	0.000	0.133	0.000	0.003	98.125	Amphibole
	3	45.827	14.717	0.434	1.335	1.786	0.000	10.207	11.636	10.613	0.239	0.103	0.169	0.111	0.043	0.088	97.255	Amphibole
	4	45.740	14.409	0.486	1.574	1.896	0.000	10.186	13.073	10.671	0.211	0.089	0.000	0.119	0.013	0.000	98.427	Amphibole
	5	46.131	14.845	0.455	1.632	1.718	0.018	10.234	12.207	10.245	0.247	0.000	0.113	0.074	0.000	0.027	97.946	Amphibole

Sample	Point	SiO_2	MgO	K_2O	TiO_2	Na_2O	P_2O_5	CaO	FeO	Al_2O_3	MnO	F	BaO	SO_3	Cl	Cr_2O_3	Total	Mineral
JM-17-PR6-KK-5	11	43.674	12.416	0.552	1.509	1.887	0.000	10.208	15.375	12.319	0.241	0.013	0.195	0.008	0.038	0.000	98.421	Amphibole
	12	47.238	13.621	0.434	0.897	1.373	0.000	10.553	14.469	8.617	0.525	0.000	0.000	0.002	0.044	0.007	97.770	Amphibole
	13	46.746	15.929	0.419	1.326	1.485	0.000	10.291	11.079	10.222	0.204	0.013	0.035	0.015	0.000	0.206	97.965	Amphibole

APPENDIX F. ELECTRON MICROPROBE SPOT ANALYSES OF MAFIC AND OXIDE MINERALS (CONTINUED)

Sample	Point	SiO_2	MgO	K_2O	TiO_2	Na_2O	P_2O_5	CaO	FeO	Al_2O_3	MnO	F	SO_3	Cl	Cr_2O_3	ZrO_2	HfO_2	La_2O_3	Ce_2O_3	Total	Mineral
JM-17-ERN3-KK-1	1	32.388	0.003	0.000	0.000	0.000	0.004	0.004	0.000	0.011	1.033	0.106	0.006	0.000	0.018	64.389	1.525	0.000	0.000	99.442	Zircon
	2	0.018	0.681	0.007	4.084	0.017	0.000	0.000	84.250	0.974	1.977	0.000	0.000	0.021	0.000	0.000	0.000	0.000	0.000	92.024	Magnetite
	3	0.210	0.000	0.000	44.982	0.090	0.000	0.075	39.398	0.004	1.603	0.092	0.024	0.015	0.005	0.000	0.101	0.000	0.010	86.567	Ilmenite

Sample	Point	SiO_2	MgO	K_2O	TiO_2	Na_2O	P_2O_5	CaO	FeO	Al_2O_3	MnO	F	SO_3	Cl	Cr_2O_3	ZrO_2	HfO_2	La_2O_3	Ce_2O_3	Total	Mineral
JM-17-ERN3-KK-2	1	0.035	0.519	0.000	3.927	0.000	0.007	0.006	83.576	1.018	2.119	0.000	0.035	0.000	0.000	0.000	0.000	0.000	0.005	91.247	Magnetite
	2	0.992	1.114	0.005	39.174	0.012	0.022	0.038	48.190	0.693	4.032	0.000	0.079	0.000	0.000	0.000	0.000	0.000	0.045	94.396	Ilmenite
	3	0.057	0.583	0.000	4.363	0.000	0.000	0.009	82.927	0.967	2.004	0.000	0.042	0.013	0.000	0.000	0.000	0.000	0.027	90.989	Magnetite
	4	0.000	1.138	0.000	38.781	0.009	0.000	0.009	48.681	0.069	3.679	0.000	0.000	0.000	0.012	0.000	0.000	0.000	0.013	92.391	Ilmenite

Sample	Point	SiO_2	MgO	K_2O	TiO_2	Na_2O	P_2O_5	CaO	FeO	Al_2O_3	MnO	F	SO_3	Cl	Cr_2O_3	ZrO_2	HfO_2	La_2O_3	Ce_2O_3	Total	Mineral
JM-17-ERN3-KK-4	1	0.116	0.601	0.000	3.404	0.045	0.000	0.027	82.820	1.129	1.851	0.000	0.000	0.000	0.000	0.000	0.096	0.000	0.000	90.089	Magnetite
	2	0.037	1.217	0.000	39.997	0.000	0.000	0.024	48.644	0.087	3.630	0.061	0.006	0.000	0.000	0.000	0.000	0.000	0.053	93.730	Ilmenite

Sample	Point	SiO_2	MgO	K_2O	TiO_2	Na_2O	P_2O_5	CaO	FeO	Al_2O_3	MnO	F	SO_3	Cl	Cr_2O_3	ZrO_2	HfO_2	La_2O_3	Ce_2O_3	Total	Mineral
JM-17-ERN3-KK-5	1	0.048	0.655	0.002	3.850	0.000	0.000	0.007	84.481	1.004	2.190	0.000	0.009	0.011	0.011	0.000	0.014	0.000	0.000	92.280	Magnetite
	2	0.017	0.568	0.008	3.822	0.058	0.003	0.000	84.875	1.046	1.894	0.000	0.039	0.000	0.024	0.000	0.071	0.000	0.073	92.498	Magnetite
	3	0.011	1.192	0.016	39.389	0.000	0.000	0.013	49.291	0.084	3.616	0.000	0.000	0.000	0.028	0.000	0.115	0.000	0.000	93.755	Ilmenite

Sample	Point	SiO_2	MgO	K_2O	TiO_2	Na_2O	P_2O_5	CaO	FeO	Al_2O_3	MnO	F	SO_3	Cl	Cr_2O_3	ZrO_2	HfO_2	La_2O_3	Ce_2O_3	Total	Mineral
JM-17-ERC5-KK-1	2	30.779	1.751	0.000	2.398	0.000	0.000	10.521	18.153	14.089	0.602	0.000	0.000	0.002	0.000	0.000	0.119	6.007	9.628	94.049	Allanite
	3	0.055	0.958	0.000	42.648	0.010	0.000	0.008	42.643	0.149	2.409	0.000	0.000	0.000	0.012	0.000	0.000	0.000	0.000	88.892	Ilmenite
	4	32.049	0.000	0.000	0.000	0.035	0.247	0.010	0.000	0.000	1.592	0.067	0.013	0.000	0.000	60.806	1.261	0.021	0.040	96.113	Zircon

Sample	Point	SiO_2	MgO	K_2O	TiO_2	Na_2O	P_2O_5	CaO	FeO	Al_2O_3	MnO	F	SO_3	Cl	Cr_2O_3	ZrO_2	HfO_2	La_2O_3	Ce_2O_3	Total	Mineral
JM-17-ERC5-KK-2	1	49.939	15.979	0.000	1.661	0.363	0.037	20.563	10.092	2.996	0.160	0.000	0.027	0.000	0.177	0.000	0.000	0.000	0.005	101.999	Amphibole
	3	32.745	0.003	0.000	0.000	0.000	0.000	0.015	0.000	0.000	1.455	0.053	0.034	0.021	0.000	64.345	1.477	0.000	0.024	100.145	Zircon

Sample	Point	SiO_2	MgO	K_2O	TiO_2	Na_2O	P_2O_5	CaO	FeO	Al_2O_3	MnO	F	SO_3	Cl	Cr_2O_3	ZrO_2	HfO_2	La_2O_3	Ce_2O_3	Total	Mineral
JM-17-ERC5-KK-5	1	30.831	1.786	0.001	2.155	0.056	0.043	10.582	18.084	13.840	0.695	0.177	0.000	0.023	0.000	0.000	0.000	5.751	9.571	93.515	Allanite
	2	29.888	1.701	0.000	0.630	0.046	0.048	10.822	18.132	13.878	0.592	0.076	0.000	0.023	0.000	0.000	0.075	6.062	9.802	91.738	Allanite
	3	0.697	0.128	0.000	0.000	0.000	0.000	0.004	86.659	0.067	0.992	0.000	0.034	0.007	0.006	0.000	0.060	0.028	0.000	88.680	Magnetite

APPENDIX F. ELECTRON MICROPROBE SPOT ANALYSES OF MAFIC AND OXIDE MINERALS (CONTINUED)

Sample	Point	SiO_2	MgO	K_2O	TiO_2	Na_2O	P_2O_5	CaO	FeO	Al_2O_3	MnO	F	SO_3	Cl	Cr_2O_3	ZrO_2	HfO_2	La_2O_3	Ce_2O_3	Total	Mineral
JM-17-ERS2-KK-1	1	32.391	0.000	0.000	0.064	0.036	0.114	0.009	0.032	0.000	0.014	0.238	0.093	0.000	0.000	63.697	1.162	0.000	0.000	97.750	Zircon
	2	0.016	1.306	0.000	40.968	0.000	0.000	0.006	49.203	0.059	3.856	0.000	0.000	0.001	0.000	0.000	0.038	0.000	0.014	95.467	Ilmenite
	3	34.953	15.173	7.123	4.450	0.894	0.047	0.089	12.025	14.762	0.153	0.335	0.072	0.095	0.011	0.000	0.027	0.000	0.158	90.205	Biotite
	4	36.172	15.458	7.253	4.658	0.926	0.021	0.105	12.414	15.056	0.279	0.508	0.083	0.107	0.021	0.000	0.000	0.000	0.220	93.043	Biotite
	5	0.024	1.110	0.000	48.631	0.000	0.008	0.033	38.106	0.098	3.369	0.000	0.009	0.000	0.000	0.015	0.095	0.000	0.016	91.514	Ilmenite

Sample	Point	SiO_2	MgO	K_2O	TiO_2	Na_2O	P_2O_5	CaO	FeO	Al_2O_3	MnO	F	SO_3	Cl	Cr_2O_3	ZrO_2	HfO_2	La_2O_3	Ce_2O_3	Total	Mineral
JM-17-ERS2-KK-2	2	33.374	0.014	0.000	0.001	0.032	0.177	0.009	0.092	0.000	0.000	0.148	0.042	0.000	0.007	65.838	1.550	0.042	0.000	101.264	Zircon
	3	0.029	1.274	0.015	41.012	0.000	0.000	0.003	47.778	0.070	3.940	0.000	0.000	0.000	0.027	0.015	0.086	0.000	0.000	94.249	Ilmenite

Sample	Point	SiO_2	MgO	K_2O	TiO_2	Na_2O	P_2O_5	CaO	FeO	Al_2O_3	MnO	F	SO_3	Cl	Cr_2O_3	ZrO_2	HfO_2	La_2O_3	Ce_2O_3	Total	Mineral
JM-17-ERS2-KK-3	1	39.125	12.403	0.748	7.080	1.959	0.012	13.190	14.418	11.857	0.107	0.184	0.084	0.009	0.050	0.000	0.000	0.000	0.000	101.147	Amphibole
	2	43.830	14.242	0.483	2.308	1.509	0.045	11.913	14.922	9.624	0.128	0.140	0.044	0.032	0.015	0.000	0.000	0.000	0.000	99.169	Amphibole
	4	32.168	0.005	0.000	0.000	0.000	0.138	0.010	0.000	0.000	0.687	0.079	0.048	0.009	0.007	62.191	1.400	0.000	0.036	96.743	Zircon
	5	32.732	0.000	0.006	0.000	0.000	0.000	0.017	0.000	0.000	1.130	0.000	0.013	0.010	0.000	63.086	1.361	0.000	0.000	98.353	Zircon
	6	36.703	12.638	7.785	4.154	0.629	0.015	0.037	19.028	15.493	0.575	0.861	0.042	0.074	0.039	0.000	0.000	0.000	0.000	97.693	Biotite
	7	36.680	12.906	7.707	3.817	0.597	0.022	0.092	19.657	15.873	0.513	0.192	0.142	0.097	0.000	0.000	0.000	0.000	0.000	98.192	Biotite
	8	43.719	8.899	0.165	1.584	1.447	0.043	10.728	20.825	13.203	0.265	0.024	0.104	0.025	0.021	0.000	0.002	0.000	0.036	101.074	Amphibole

Sample	Point	SiO_2	MgO	K_2O	TiO_2	Na_2O	P_2O_5	CaO	FeO	Al_2O_3	MnO	F	SO_3	Cl	Cr_2O_3	ZrO_2	HfO_2	La_2O_3	Ce_2O_3	Total	Mineral
JM-17-ERS2-KK-4	1	48.197	15.375	0.279	1.538	0.741	0.000	12.180	14.998	5.088	0.246	0.000	0.024	0.018	0.045	0.000	0.000	0.000	0.000	98.725	Amphibole
	2	41.836	7.537	0.195	1.716	1.475	0.018	11.473	21.549	16.564	0.283	0.061	0.000	0.006	0.025	0.000	0.030	0.000	0.000	102.741	Amphibole

APPENDIX F. ELECTRON MICROPROBE SPOT ANALYSES OF MAFIC AND OXIDE MINERALS (CONTINUED)

Sample	**Point**	**SiO_2**	**MgO**	**K_2O**	**TiO_2**	**Na_2O**	**P_2O_5**	**CaO**	**FeO**	**Al_2O_3**	**MnO**	**F**	**BaO**	**SO_3**	**Cl**	**Cr_2O_3**	**Nb_2O_5**	**Total**	**Mineral**
JM-17-I2-KK-1	12	0.249	0.093	0.000	11.715	0.055	0.041	0.024	76.713	0.491	1.912	0.000	0.151	0.004	0.000	0.000	0.489	91.937	Magnetite

Sample	**Point**	**SiO_2**	**MgO**	**K_2O**	**TiO_2**	**Na_2O**	**P_2O_5**	**CaO**	**FeO**	**Al_2O_3**	**MnO**	**F**	**BaO**	**SO_3**	**Cl**	**Cr_2O_3**	**Nb_2O_5**	**Total**	**Mineral**
JM-17-I2-KK-2	6	33.978	0.000	0.000	0.000	0.034	0.000	0.001	0.461	0.000	0.069	0.000	0.006	0.038	0.000	0.000	0.091	34.678	Zircon
	7	0.140	0.036	0.006	11.801	0.000	0.000	0.018	79.805	0.362	2.325	0.000	0.169	0.000	0.008	0.000	0.404	95.072	Magnetite
	8	0.152	0.071	0.003	10.757	0.010	0.000	0.006	78.997	0.323	2.098	0.000	0.199	0.009	0.005	0.099	0.097	92.825	Magnetite
	9	0.120	0.072	0.012	9.827	0.031	0.000	0.010	78.774	0.226	2.694	0.000	0.113	0.004	0.000	0.056	0.186	92.125	Magnetite
	10	33.795	0.000	0.000	0.134	0.007	0.000	0.038	0.713	0.000	0.005	0.000	0.000	0.038	0.000	0.028	0.000	34.758	Zircon
	13	31.552	3.895	0.000	0.174	0.000	0.000	0.185	61.213	0.045	5.132	0.000	0.128	0.028	0.000	0.040	0.009	102.401	Fayalite
	14	31.062	3.714	0.000	0.007	0.000	0.000	0.161	58.065	0.012	5.120	0.000	0.000	0.000	0.010	0.000	0.000	98.149	Fayalite
	15	31.385	3.509	0.000	0.000	0.088	0.008	0.180	61.318	0.015	5.292	0.000	0.000	0.024	0.007	0.017	0.029	101.870	Fayalite
	16	31.703	3.070	0.007	0.017	0.045	0.098	0.178	53.538	0.274	5.600	0.000	0.000	0.004	0.006	0.001	0.000	94.540	Fayalite
	17	30.789	3.738	0.000	0.000	0.035	0.007	0.118	59.118	0.002	5.933	0.000	0.000	0.000	0.000	0.000	0.000	99.740	Fayalite
	18	5.962	0.230	0.025	0.000	0.018	0.326	0.124	78.241	2.146	1.532	0.000	0.000	0.000	0.080	0.000	0.002	88.668	Magnetite

Sample	**Point**	**SiO_2**	**MgO**	**K_2O**	**TiO_2**	**Na_2O**	**P_2O_5**	**CaO**	**FeO**	**Al_2O_3**	**MnO**	**F**	**BaO**	**SO_3**	**Cl**	**Cr_2O_3**	**Nb_2O_5**	**Total**	**Mineral**
JM-17-I2-KK-3	3	0.136	0.039	0.000	11.667	0.027	0.002	0.048	77.561	0.314	2.506	0.000	0.076	0.000	0.000	0.000	0.146	92.522	Magnetite
	4	0.166	0.080	0.002	9.530	0.061	0.000	0.007	81.012	0.393	2.048	0.000	0.182	0.007	0.000	0.000	0.100	93.588	Magnetite
	5	0.163	0.066	0.012	13.024	0.024	0.000	0.016	75.324	0.484	1.890	0.000	0.065	0.000	0.000	0.021	0.328	91.417	Magnetite

Sample	**Point**	**SiO_2**	**MgO**	**K_2O**	**TiO_2**	**Na_2O**	**P_2O_5**	**CaO**	**FeO**	**Al_2O_3**	**MnO**	**F**	**BaO**	**SO_3**	**Cl**	**Cr_2O_3**	**Nb_2O_5**	**Total**	**Mineral**
JM-17-I2-KK-6	7	31.244	3.647	0.005	0.024	0.000	0.000	0.174	61.043	0.000	5.319	0.000	0.000	0.000	0.002	0.011	0.000	101.469	Fayalite
	8	31.430	3.734	0.005	0.014	0.000	0.000	0.152	61.687	0.000	5.258	0.000	0.022	0.017	0.000	0.000	0.033	102.352	Fayalite
	9	31.549	3.708	0.000	0.034	0.029	0.000	0.165	60.445	0.000	5.185	0.000	0.000	0.000	0.013	0.000	0.024	101.149	Fayalite

Sample	**Point**	**SiO_2**	**MgO**	**K_2O**	**TiO_2**	**Na_2O**	**P_2O_5**	**CaO**	**FeO**	**Al_2O_3**	**MnO**	**F**	**BaO**	**SO_3**	**Cl**	**Cr_2O_3**	**Nb_2O_5**	**Total**	**Mineral**
JM-17-I2-KK-9	1	0.152	0.112	0.000	8.106	0.068	0.000	0.017	81.837	0.288	2.844	0.000	0.000	0.000	0.000	0.004	0.250	93.678	Magnetite
	2	0.152	0.111	0.000	9.686	0.000	0.000	0.003	79.598	0.309	2.422	0.000	0.055	0.024	0.000	0.001	0.253	92.614	Magnetite

Sample	**Point**	**SiO_2**	**MgO**	**K_2O**	**TiO_2**	**Na_2O**	**P_2O_5**	**CaO**	**FeO**	**Al_2O_3**	**MnO**	**F**	**BaO**	**SO_3**	**Cl**	**Cr_2O_3**	**Nb_2O_5**	**Total**	**Mineral**
JM-17-I2-KK-10	4	0.175	0.108	0.003	6.202	0.000	0.020	0.020	82.283	0.309	2.990	0.000	0.117	0.000	0.000	0.010	0.015	92.252	Magnetite
	5	0.166	0.148	0.010	7.792	0.008	0.000	0.008	81.470	0.250	3.002	0.000	0.002	0.006	0.000	0.094	0.097	93.053	Magnetite

APPENDIX G. ELECTRON MICROPROBE TRANSECT ANALYSES OF BIOTITE AND AMPHIBOLE IN PUMICE RING RHYOLITE. UNRELIABLE DATA NOT INCLUDED IN RESULTS HAVE BEEN OMITTED.

Sample	Point	SiO_2	MgO	K_2O	TiO_2	Na_2O	P_2O_5	CaO	FeO	Al_2O_3	MnO	F	BaO	SO_3	Cl	Cr_2O_3	Total
JM-17-PR6-KK	1	45.981	13.129	0.495	1.093	1.418	0.000	10.502	14.986	9.138	0.564	0.000	0.000	0.252	0.027	0.000	97.579
Amphibole 1	2	46.155	14.165	0.411	1.130	1.676	0.000	9.933	12.943	10.242	0.287	0.102	0.000	0.302	0.000	0.040	97.343
Rim to Rim	3	43.849	13.583	0.537	1.781	1.893	0.019	10.261	13.177	11.789	0.173	0.204	0.000	0.098	0.000	0.000	97.278
	4	43.511	13.337	0.545	1.869	1.917	0.010	10.145	13.052	12.328	0.203	0.128	0.017	0.300	0.000	0.087	97.395
	5	42.551	12.133	0.854	1.939	1.987	0.000	9.767	15.227	12.795	0.240	0.151	0.034	0.105	0.056	0.040	97.802
	6	46.829	13.535	0.455	1.207	1.291	0.002	10.308	14.314	8.979	0.470	0.089	0.000	0.039	0.010	0.023	97.512
	7	43.359	13.471	0.531	1.456	1.975	0.000	10.090	13.352	12.430	0.189	0.063	0.071	0.106	0.004	0.000	97.069
	8	42.913	12.806	0.638	2.048	2.232	0.000	9.815	14.526	12.780	0.426	0.038	0.000	0.094	0.060	0.040	98.386
	9	42.338	12.237	0.562	1.944	2.003	0.000	10.121	14.233	12.328	0.211	0.051	0.105	0.103	0.046	0.047	96.298
	10	43.298	12.939	0.574	2.105	2.038	0.000	10.036	13.989	12.467	0.205	0.026	0.000	0.080	0.000	0.000	97.746
	11	43.427	13.259	0.538	1.869	2.018	0.000	10.142	13.826	12.503	0.219	0.013	0.000	0.101	0.015	0.037	97.959
	12	42.994	12.883	0.718	1.852	2.088	0.000	9.961	14.164	12.590	0.292	0.000	0.036	0.127	0.032	0.043	97.773
	13	45.230	14.203	0.444	1.526	1.657	0.000	10.360	12.338	10.620	0.252	0.000	0.082	0.091	0.000	0.081	96.884

Sample	Point	SiO_2	MgO	K_2O	TiO_2	Na_2O	P_2O_5	CaO	FeO	Al_2O_3	MnO	F	BaO	SO_3	Cl	Cr_2O_3	Total
JM-17-PR6-KK	18	41.191	11.360	7.032	2.520	0.041	0.000	0.372	15.239	15.155	0.075	0.185	0.095	0.096	0.055	0.000	93.326
Biotite 1a	19	37.868	12.978	8.233	3.312	0.061	0.000	0.288	15.862	16.177	0.255	0.160	0.000	0.141	0.025	0.066	95.353
Rim to Rim	20	37.738	13.058	8.146	3.633	0.132	0.000	0.263	14.694	16.339	0.188	0.050	0.000	0.132	0.043	0.000	94.385
	21	37.065	12.688	8.179	2.866	0.070	0.225	0.328	14.833	14.020	0.126	0.098	0.031	0.178	0.028	0.020	90.708
	22	37.570	12.740	7.984	2.958	0.334	0.000	0.174	15.381	17.013	0.097	0.086	0.118	0.135	0.067	0.033	94.639
	23	38.255	12.794	7.957	3.076	0.072	0.033	0.241	15.457	16.691	0.253	0.049	0.000	0.168	0.027	0.023	95.069

Sample	Point	SiO_2	MgO	K_2O	TiO_2	Na_2O	P_2O_5	CaO	FeO	Al_2O_3	MnO	F	BaO	SO_3	Cl	Cr_2O_3	Total
JM-17-PR6-KK		38.860	12.195	7.439	2.936	0.031	0.017	0.359	15.287	16.848	0.207	0.197	0.285	0.138	0.072	0.017	94.789
Biotite 1b		39.704	11.158	7.098	2.785	0.065	0.128	0.917	14.404	16.830	0.215	0.050	0.000	0.183	0.016	0.020	93.548
Rim to Rim		39.178	12.693	8.025	3.261	0.261	0.000	0.307	15.511	14.811	0.188	0.098	0.337	0.065	0.048	0.027	94.758

APPENDIX G. ELECTRON MICROPROBE TRANSECT ANALYSES OF BIOTITE AND AMPHIBOLE IN PUMICE RING RHYOLITE (CONTINUED)

Sample	**Point**	**SiO_2**	**MgO**	**K_2O**	**TiO_2**	**Na_2O**	**P_2O_5**	**CaO**	**FeO**	**Al_2O_3**	**MnO**	**F**	**BaO**	**SO_3**	**Cl**	**Cr_2O_3**	**Total**
JM-17-PR6-KK	1	46.228	14.952	0.401	1.477	1.718	0.000	10.358	12.389	9.695	0.135	0.000	0.115	0.075	0.015	0.232	97.787
Amphibole 2	2	44.339	13.685	0.436	1.383	1.540	0.000	10.554	13.757	10.506	0.387	0.013	0.000	0.064	0.032	0.054	96.738
Rim to Rim	3	46.513	13.987	0.394	1.207	1.369	0.000	10.279	14.760	9.205	0.441	0.000	0.145	0.129	0.000	0.010	98.439
	4	45.447	14.360	0.480	1.678	1.688	0.000	10.248	12.614	10.464	0.225	0.000	0.000	0.113	0.006	0.199	97.521
	5	47.316	14.054	0.397	0.811	1.416	0.000	10.487	14.245	8.990	0.379	0.051	0.000	0.104	0.000	0.070	98.299
	6	46.760	13.638	0.422	1.056	1.357	0.000	10.488	14.296	8.987	0.471	0.013	0.000	0.095	0.001	0.000	97.579

Sample	**Point**	**SiO_2**	**MgO**	**K_2O**	**TiO_2**	**Na_2O**	**P_2O_5**	**CaO**	**FeO**	**Al_2O_3**	**MnO**	**F**	**BaO**	**SO_3**	**Cl**	**Cr_2O_3**	**Total**
JM-17-PR6-KK	6	44.954	14.219	0.479	1.385	1.735	0.000	10.222	12.981	11.183	0.209	0.000	0.017	0.127	0.000	0.023	97.534
Amphibole 3a	7	45.701	14.759	0.460	1.255	1.654	0.000	10.249	12.576	10.517	0.141	0.000	0.004	0.122	0.000	0.067	97.505
Rim to Rim	8	45.586	14.750	0.451	1.601	1.715	0.000	10.234	12.525	10.398	0.182	0.218	0.000	0.147	0.000	0.027	97.742

Sample	**Point**	**SiO_2**	**MgO**	**K_2O**	**TiO_2**	**Na_2O**	**P_2O_5**	**CaO**	**FeO**	**Al_2O_3**	**MnO**	**F**	**BaO**	**SO_3**	**Cl**	**Cr_2O_3**	**Total**
JM-17-PR6-KK	9	38.102	12.420	7.984	3.355	0.268	0.000	0.185	15.472	14.933	0.218	0.111	0.276	0.161	0.066	0.000	93.489
Biotite 3a	10	38.385	13.057	8.109	3.447	0.168	0.000	0.209	15.786	14.993	0.234	0.037	0.020	0.121	0.044	0.013	94.597
Rim to Rim	11	39.788	13.029	7.791	3.231	0.095	0.000	0.194	15.333	16.049	0.156	0.161	0.000	0.187	0.032	0.000	95.971

Sample	**Point**	**SiO_2**	**MgO**	**K_2O**	**TiO_2**	**Na_2O**	**P_2O_5**	**CaO**	**FeO**	**Al_2O_3**	**MnO**	**F**	**BaO**	**SO_3**	**Cl**	**Cr_2O_3**	**Total**
JM-17-PR6-KK	12	40.356	10.645	6.341	2.483	0.087	0.000	0.451	14.435	17.018	0.146	0.112	0.077	0.166	0.089	0.003	92.342
Biotite 3b	13	36.650	13.382	8.739	3.939	0.476	0.000	0.011	17.342	16.409	0.215	0.121	0.925	0.219	0.053	0.000	98.418
Rim to Rim	14	36.205	13.085	8.548	3.370	0.466	0.000	0.070	16.678	15.965	0.199	0.037	0.556	0.128	0.089	0.007	95.367

Sample	**Point**	**SiO_2**	**MgO**	**K_2O**	**TiO_2**	**Na_2O**	**P_2O_5**	**CaO**	**FeO**	**Al_2O_3**	**MnO**	**F**	**BaO**	**SO_3**	**Cl**	**Cr_2O_3**	**Total**
JM-17-PR6-KK	15	46.067	12.913	0.536	0.970	1.356	0.000	10.623	15.472	8.888	0.457	0.000	0.000	0.078	0.041	0.020	97.412
Amphibole 3b	16	46.391	15.533	0.414	1.283	1.637	0.000	10.041	11.699	10.254	0.204	0.051	0.000	0.079	0.028	0.186	97.773
Rim to Rim	17	45.765	15.243	0.437	1.335	1.731	0.007	10.158	11.721	10.123	0.130	0.077	0.024	0.108	0.000	0.304	97.131
	18	44.493	13.001	0.489	1.212	1.797	0.013	10.221	14.287	11.194	0.189	0.114	0.000	0.108	0.000	0.000	97.070

APPENDIX G. ELECTRON MICROPROBE TRANSECT ANALYSES OF BIOTITE AND AMPHIBOLE IN PUMICE RING RHYOLITE (CONTINUED)

Sample	Point	SiO_2	MgO	K_2O	TiO_2	Na_2O	P_2O_5	CaO	FeO	Al_2O_3	MnO	F	BaO	SO_3	Cl	Cr_2O_3	Total
JM-17-PR6-KK	1	44.274	12.920	0.514	1.681	1.827	0.016	10.205	14.461	11.220	0.235	0.254	0.047	0.121	0.066	0.000	97.719
Amphibole 4	2	44.506	13.648	0.459	1.393	1.701	0.000	10.188	12.421	10.760	0.230	0.038	0.000	0.148	0.054	0.007	95.525
Rim to Rim	3	44.330	13.672	0.469	1.480	1.879	0.000	10.341	13.271	11.191	0.173	0.331	0.013	0.103	0.000	0.000	97.114
	4	45.920	14.763	0.432	1.381	1.516	0.000	10.200	11.157	9.984	0.299	0.000	0.051	0.089	0.000	0.108	95.900
	5	44.146	14.232	0.456	1.380	1.601	0.000	10.071	13.323	10.931	0.179	0.000	0.000	0.105	0.000	0.020	96.444

Sample	Point	SiO_2	MgO	K_2O	TiO_2	Na_2O	P_2O_5	CaO	FeO	Al_2O_3	MnO	F	BaO	SO_3	Cl	Cr_2O_3	Total
JM-17-PR6-KK	6	39.834	9.447	5.840	2.085	0.133	0.000	0.544	15.299	13.012	0.183	0.147	0.000	0.092	0.228	0.000	86.731
Biotite 4a	7	39.343	12.252	7.549	2.942	0.155	0.000	0.315	14.683	14.912	0.148	0.297	0.176	0.127	0.072	0.033	92.863
Rim to Rim	8	39.241	12.569	7.559	3.026	0.083	0.000	0.301	15.077	15.226	0.092	0.210	0.115	0.164	0.070	0.000	93.629
	9	31.065	10.866	6.558	2.658	0.094	0.000	0.135	11.808	12.596	0.102	0.012	0.088	0.065	0.553	0.000	76.470
	10	39.065	12.133	7.404	3.201	0.187	0.000	0.280	15.990	14.826	0.186	0.111	0.318	0.123	0.074	0.060	93.894

Sample	Point	SiO_2	MgO	K_2O	TiO_2	Na_2O	P_2O_5	CaO	FeO	Al_2O_3	MnO	F	BaO	SO_3	Cl	Cr_2O_3	Total
JM-17-PR6-KK	11	37.519	14.194	8.512	3.591	0.386	0.000	0.064	15.550	15.254	0.057	0.160	0.419	0.055	0.071	0.017	95.766
Biotite 4b	12	38.180	13.311	8.243	3.340	0.220	0.000	0.178	15.794	15.380	0.226	0.012	0.348	0.033	0.064	0.000	95.310
Rim to Rim	13	35.877	13.498	8.194	3.325	0.277	0.000	0.110	14.869	14.913	0.161	0.098	0.097	0.108	0.135	0.020	91.611
	14	37.649	13.881	8.476	3.535	0.402	0.000	0.084	15.318	15.690	0.148	0.061	0.735	0.144	0.072	0.000	96.153
	15	37.178	14.205	8.747	3.552	0.456	0.000	0.024	16.350	15.697	0.285	0.061	0.655	0.154	0.041	0.000	97.370

JM-17-PR6-KK	1	44.759	13.677	0.484	1.503	1.790	0.000	10.265	13.299	11.266	0.200	0.089	0.000	0.025	0.026	0.037	97.377
Amphibole 5	2	45.896	14.887	0.476	1.498	1.723	0.000	10.420	12.640	10.633	0.217	0.051	0.000	0.004	0.000	0.000	98.424
Rim to Rim	3	44.804	12.766	0.431	1.101	1.641	0.000	9.875	15.537	11.406	0.295	0.201	0.007	0.070	0.000	0.000	98.049
	4	45.917	15.403	0.413	1.049	1.751	0.000	10.138	12.081	9.766	0.165	0.000	0.000	0.055	0.000	0.000	96.738
	6	45.913	15.105	0.441	1.350	1.682	0.000	10.331	11.807	9.845	0.195	0.000	0.046	0.012	0.021	0.094	96.837
	7	46.235	14.791	0.492	1.428	1.833	0.035	10.486	13.187	11.482	0.238	0.000	0.080	0.015	0.000	0.000	100.302
	8	44.799	14.235	0.487	1.426	1.805	0.017	10.370	12.754	10.953	0.228	0.141	0.000	0.025	0.000	0.034	97.215
	9	44.626	13.870	0.507	1.504	1.875	0.000	10.322	14.153	11.397	0.214	0.000	0.009	0.021	0.025	0.030	98.547
	10	44.452	13.608	0.518	1.531	1.672	0.000	10.445	14.012	10.884	0.254	0.000	0.060	0.037	0.032	0.000	97.498

APPENDIX G. ELECTRON MICROPROBE TRANSECT ANALYSES OF BIOTITE AND AMPHIBOLE IN PUMICE RING RHYOLITE (CONTINUED)

Sample	Point	SiO_2	MgO	K_2O	TiO_2	Na_2O	P_2O_5	CaO	FeO	Al_2O_3	MnO	F	BaO	SO_3	Cl	Cr_2O_3	Total
JM-17-PR6-KK	14	37.252	13.549	8.509	3.691	0.395	0.000	0.043	16.921	15.316	0.161	0.049	0.600	0.069	0.074	0.007	96.598
Biotite 5	15	38.913	13.033	8.287	3.333	0.064	0.000	0.170	14.749	14.886	0.159	0.025	0.156	0.058	0.017	0.000	93.835
Rim to Rim	16	38.816	13.278	8.637	3.539	0.042	0.000	0.071	15.490	15.375	0.183	0.000	0.040	0.055	0.064	0.000	95.576
	17	41.036	11.770	7.045	2.939	0.105	0.000	0.373	15.368	15.457	0.156	0.074	0.197	0.089	0.022	0.073	94.668

Sample	Point	SiO_2	MgO	K_2O	TiO_2	Na_2O	P_2O_5	CaO	FeO	Al_2O_3	MnO	F	BaO	SO_3	Cl	Cr_2O_3	Total
JM-17-PR6-KK	21	46.197	13.273	0.503	0.900	1.355	0.000	10.362	14.907	9.179	0.481	0.228	0.000	0.023	0.028	0.000	97.334
Amphibole 6	22	44.417	14.461	0.472	1.669	1.857	0.000	10.131	11.764	11.391	0.149	0.090	0.184	0.026	0.001	0.061	96.635
Rim to Rim	23	46.449	13.698	0.426	0.841	1.298	0.000	10.569	14.530	8.513	0.490	0.025	0.029	0.041	0.034	0.027	96.951
	24	46.631	13.289	0.478	0.882	1.266	0.000	10.490	14.644	8.679	0.533	0.000	0.000	0.078	0.022	0.007	96.994
	25	46.467	13.280	0.459	0.922	1.395	0.000	10.498	15.109	8.884	0.414	0.000	0.018	0.043	0.040	0.000	97.520

Sample	Point	SiO_2	MgO	K_2O	TiO_2	Na_2O	P_2O_5	CaO	FeO	Al_2O_3	MnO	F	BaO	SO_3	Cl	Cr_2O_3	Total
JM-17-PR6-KK	26	36.837	13.287	8.082	3.282	0.448	0.000	0.158	15.873	15.511	0.167	0.000	0.621	0.047	0.073	0.040	94.410
Biotite 6	27	36.651	11.878	7.037	3.062	0.079	0.502	2.289	14.085	15.308	0.175	0.361	0.277	0.111	0.066	0.000	91.714
Rim to Rim	28	40.688	10.864	6.627	2.842	0.077	0.031	0.648	14.234	17.188	0.194	0.050	0.004	0.047	0.087	0.000	93.540
	29	39.797	11.625	6.973	2.864	0.125	0.045	0.460	14.899	16.399	0.105	0.124	0.095	0.027	0.085	0.027	93.579
	30	37.782	13.989	8.075	3.759	0.437	0.000	0.121	15.425	15.089	0.207	0.049	0.756	0.029	0.057	0.047	95.788

APPENDIX H. FRACTIONAL CRYSTALLIZATION MODELING DATA. PARTITION COEFFICIENTS SOURCED FROM GERM DATABASE.

Basalt Partition Coefficients

Element	Plagioclase	CPX	OPX	Olivine	Magnetite
Rb	0.215	0.13	0.0006	0.04	0
Sr	1.8	0.1395	0.109	0.02	0
Y	0.027	1	0	0.138	0
Zr	0.2	0.27	0.02	0.06	0
Nb	0.01	0.0345	0.003	0.009	0
Ba	2.08	0.04	0.0035	0.03	0.028
Sc	0.07	2.805	2.075	0.08	1.96
Cr	0.34	8.075	4.22	2.06	153
Ni	0.5	2.91	1.1	12.2	29
Cs	0.135	0.13	0	0.05	0
La	0.22	0.084	0.084	0.012	0.062
Ce	0.09	0.7045	0.0843	0.009	0.2
Nd	0.04	0.382	0.382	0.0003	0.25
Sm	0.036	0.736	0.375	0.0037	0.3
Eu	0.865	0.63	0.388	0.01	0.062
Tb	0.11	0.73	0.508	0.00518	0.11
Yb	0.03	0.6	0.5585	0.0087	0.11
Lu	0.037	0.58	0.5305	0.018	0.14
Hf	0.09	0.48	0.01	0.04	0.14
Ta	0.06	0.04	0	0.03	0.23
Pb	0.76	0.00733	0.0013	0.000274	0
Th	0.07	0.04	0.013	0.02	0.1
U	0.08	0.05	0.017	0.003509	0.11

Andesite Partition Coefficients

Element	Plagioclase	Amphibole	CPX	OPX	Olivine	Magnetite
Rb	0.16	0.4	0.03	0.01	0.03	0.15
Sr	5.28	0.01	0.28	0.01	0.02	0.11
Y	0.066	0	2.4	0.46	0	0.64
Zr	0.15	0.5	0.33	0.11	0.02	0.38
Nb	1.3	0.2	2.1	0.78	0.11	0
Ba	0.56	0.3	0	0.13	0.02	0.26
Sc	0.01	10.55	11.45	3.45	0.18	2.5
Cr	0.01	40	144	82	2.5	216.5
Ni	0.335	6.8	6.8	12.395	16.765	14.3
Cs	0.03	0.2	0.405	0.38	0.01	0.51
La	0.18	0.31	0.185	0.165	0.006	0.335
Ce	0.12	0.33	0.28	0.175	0.01	0.27
Nd	0.09	0.825	0.57	0.24	0.02	0.4
Sm	0.06	1.45	1.04	0.245	0.01	0.42
Eu	0.75	1.7	0.96	0.245	0.05375	0.32
Tb	0.15	2.0	1.55	0.315	0.11	0.52
Yb	0.1	1.35	1.165	0.425	0.165	0.355
Lu	0.1	1.3	1.13	0.495	0.2435	0.38
Hf	0.03	0.43	0.275	0.12	0.015	0.46
Ta	0.03	0.59	0.43	0.11	0	0
Pb	0.61	0.12	0.87	0.52	0.43	2.9
Th	0.01	0.19	0.1	0.13	0.0001	0.235
U	0.1955	0.008	0	0	0.01	0

Rhyolite Partition Coefficients

Element	Quartz	Plagioclase	Sanidine	Biotite	Amphibole
Rb	0	0.17	0.55	2.46	0.37
Sr	0	7.8	8.4	0.25	0.75
Y	0	0.55	0.086	2.3	20
Zr	0	0.18	0.069	0.19	0.91
Nb	0	0.08	0.1	4.6	3
Ba	0	0.47	7	6.4	0.92
Sc	0	0.01	0.029	20	14
Cs	0	0.03	0.024	4.4	0.01
La	0	0.3	0.129	15.1	0.36
Ce	0	0.22	0.065	0.234	0.68
Nd	0	0.19	0.054	0.339	1.6
Sm	0	0.12	0.026	0.392	2.3
Eu	0	2	3.3	0.501	3.2
Tb	0	0.14	0.018	3.9	2.4
Yb	0	0.1	0.015	0.165	1.8
Lu	0	0.1	0.012	0.208	1.8
Hf	0	0.03	0.034	0.6	0.52
Ta	0	0.03	0.015	1.5	0.43
Pb	0	0.84	0.83	0.21	0.61
Th	0	0.03	0.022	1	0.16
U	0	0.13	0.7	1.2	0

REFERENCES

Aldrich, M.J., 1986, Tectonics of the Jemez Lineament in the Jemez Mountains and Rio Grande Rift: Journal of Geophysical Research, v. 91, p. 1753–1762, doi: 10.1029/jb091ib02p01753.

Aldrich, M.J., Jr and Dethier, D.P., 1990, Stratigraphic and tectonic evolution of the northern Española basin, Rio Grande rift, New Mexico: Geological Society of America Bulletin, v. 102, p. 1695-1705.

Anderson, A.T., 1976, Magma mixing: petrological process and volcanological tool: Journal of Volcanology and Geothermal Research, v. 1, p. 3-33, doi: 10.1016/0377-0273(76)90016-0.

Bachmann, O., and Bergantz, G., 2008, The Magma Reservoirs That Feed Supereruptions: Elements, v. 4, p. 17-21, doi: 10.2113/gselements.4.1.17.

Bachmann, O., and Huber, C., 2016, Silicic magma reservoirs in the Earth's crust: American Mineralogist, v. 101, p. 2377–2404, doi: 10.2138/am-2016-5675.

Bailey, R., Smith, R., and Ross, C., 1969, Stratigraphic nomenclature of volcanic rocks in the Jemez Mountains, New Mexico: U.S. Geological Survey, Bulletin 1274-P, p. 1-19

Balsley, S.D., 1988, The petrology and geochemistry of the Tshirege Member of the Bandelier Tuff, Jemez Mountains, New Mexico, U.S.A. [M.S. Thesis]: University of Texas at Arlington, 188 p.

Blake, S., 1981, Volcanism and the dynamics of open magma chambers: Nature, v. 289, p. 783-785, doi: 10.1038/289783a0.

Chapin, C.E., 1979, Evolution of the Rio Grande rift—a summary: *in* Riecker, R. E., ed., Rio Grande rift: Tectonics and magmatism: Washington, D.C., American Geophysical Union, p. 1-5.

Cole, J.W., Milner, D.M., and Spinks, K.D., 2005, Calderas and caldera structures: a review: Earth-Science Reviews, v. 69, p. 1-26, doi: 10.1016/j.earscirev.2004.06.004.

Cook, G.W., Wolff, J.A., and Self, S., 2016, Estimating the eruptive volume of a large pyroclastic body: the Otowi Member of the Bandelier Tuff, Valles caldera, New Mexico: Bulletin of Volcanology, v. 78, p. 1-11, doi: 10.1007/s00445-016-1000-0.

Crowe, B.M., Linn, G.W., Heiken, G., and Bevier, M.L., 1978, Stratigraphy of the Bandelier Tuff in the Pajarito Plateau: applications to waste management: Department of Energy Informal Report LA-7225-MS, 57p., doi: 10.2172/6870764.

Dalrymple, G.B., Cox, A., Doell, R.R., and Grommé, C.S., 1967, Pliocene geomagnetic polarity epochs: Earth and Planetary Science Letters, v. 2, p. 163-173, doi: 10.1016/0012-821x(67)90122-7.

Deligne, N.I., Coles, S.G., and Sparks, R.S.J., 2010, Recurrence rates of large explosive volcanic eruptions: Journal of Geophysical Research, v. 115, doi: 10.1029/2009jb006554.

Dethier D.P., Aldrich, M.J., Jr, and Shafiqullah, M., 1986, New K-Ar ages for Micocene volcanic rocks from the northeastern Jemez Mountains and Tejana Mesa, New Mexico: Isochron West, no. 47, p. 12-14.

Eichler, C.M., 2012, Petrogenesis of the East Fork Member Rhyolites, Valles caldera, New Mexico, USA [M.S. Thesis]: University of Nevada, Las Vegas, 141 p.

Gardner, J.N., Goff, F., Garcia, S., and Hagan, R., 1986, Stratigraphic relations and lithologic variations in the Jemez volcanic field, New Mexico: Journal of Geophysical Research, v. 91, p. 1763-1778.

Gardner, J.N., and Goff, F., 1984, Potassium-argon dates from the Jemez Mountains volcanic field: Implications for tectonic activity in the north-central Rio Grande rift: New Mexico Geological Society, Guidebook 35, p.75-81.

GERM Partition Coefficient (Kd) Database, 2019, (http://earthref.org/KDD/).

Ginibre, C., Worner, G., Kronz, A., 2004, Structure and Dynamics of the Laacher See Magma Chamber (Eifler, Germany) from Major and Trace Element Zoning in Sanidine: a Cathodoluminescence and Electron Microprobe Study: Journal of Petrology, v. 45, no. 11, p. 2197-2223.

Goff, F., Rowley, J., Gardner, J.N., Hawkins, W., Goff, S., Charles, R., Wachs, D., Maassen, L., and Heiken, G., 1986, Initial results from VC-1, First Continental Scientific Drilling Program Core Hole in the Valles caldera, New Mexico: Journal of Geophysical Research, v. 91, p. 1742-1752.

Goff , F., Gardner, J.N., Baldridge, W.S., Hulen, J.B., Nielson, D.L., Vanniman, D., Heiken, G., Dungan, M.A., and Broxton, D., 1989, Excursion 17B: volcanic and hydrothermal evolution of the Valles caldera and Jemez volcanic field: New Mexico Bureau of Mines and Mineral Resources Memoir, v. 46 p. 381-434.

Goff F., Gardner J.V., and Valentine G.A., 1990, Geology of St. Peter’s Dome area, Jemez Mountains, New Mexico: New Mexico Bureau of Mines and Mineral Resources Geologic Map 69, scale 1:24,000.

Goff, F., and Gardner, J.N., 2004, Late Cenozoic geochronology of volcanism and mineralization in the Jemez Mountains and Valles caldera, north central New Mexico: *in* Mack, G.H. and Giles, K.A., eds., The Geology of New Mexico: A Geologic History: Socorro, NM, New Mexico Geological Society, Special Publication 11, p. 295-312.

Goff, F., Warren, R.G., Goff, C.J., and Dunbar, N., 2014, Eruption of reverse-zoned upper Tshirege Member, Bandelier Tuff from centralized vents within Valles caldera, New Mexico: Journal of Volcanology and Geothermal Research, v. 276, p. 82–104, doi: 10.1016/j.jvolgeores.2014.02.018.

Golombek, M.P., 1983, Geology, structure, and tectonics of the Pajarito fault zone in the Española basin of the Rio Grande rift, New Mexico: Geological Society of America Bulletin, v. 94, p. 192-205, doi: 10.1130/0016-7606(1983)94<192:gsatot>2.0.co;2.

Green, T.H., 1995, Significance of Nb/Ta as an indicator of geochemical processes in the crust-mantle system: Chemical Geology, v. 120, p. 347–359, doi: 10.1016/0009-2541(94)00145-x.

Heiken, G., Goff, F., Stix, J., Tamanyu, S., Shafiqullah, M., Garcia, S., and Hagan, R., 1986, Intracaldera volcanic activity, Toledo caldera, New Mexico: Journal of Geophysical Research, v. 91, p. 1799-1815.

Heiken, G., Goff, F., Gardner, J., Baldridge, W., Hulen, J., Nielson, D., and Vaniman, D., 1990, The Valles/Toledo caldera complex, Jemez volcanic field, New Mexico: Annual Reviews in Earth and Planetary Sciences, v. 18, p. 27-53.

Hibbard, M.J., 1995, Petrography to petrogenesis: Englewood Cliffs, NJ, Prentice Hall, 587 p.

Idleman, B., 2000, LabSPEC, v.3.1c.

Johnson, D.M., Hooper, P.R., and Conrey, R.M., 1999, XRF analysis of rocks and minerals for major and trace elements on a single low dilution Li-tetraborate fused bead: JCPDS-International Center for Diffraction Data, p. 843-867.

Jowitt, S.M., and Ernst, R.E., 2013, Geochemical assessment of the metallogenic potential of Proterozoic LIPs of Canada: Lithos, v. 174, p. 291–307, doi: 10.1016/j.lithos.2012.03.026.

Jowitt, S.M., Cooper, K., Squire, R.J., Thébaud, N., Fisher, L.A., Cas, R.A., and Pegg, I., 2014, Geology, mineralogy, and geochemistry of magnetite-associated Au mineralization of the ultramafic–basalt greenstone hosted Crusader Complex, Agnew Gold Camp, Eastern Yilgarn Craton, Western Australia; a Late Archean intrusion-related Au deposit?: Ore Geology Reviews, v. 56, p. 53–72, doi: 10.1016/j.oregeorev.2013.07.009.

Justet, L., 2003, Effects of basalt intrusion on the multi-phase evolution of the Jemez volcanic field, NM [Ph.D. Dissertation]: University of Nevada, Las Vegas, 248 p.

Karlstrom, K.E., Amato, J.M., Williams, M.L., Heizler, M.,Shaw, C.A., Read, A.S., and Bauer, P., 2004, Proterozoic tectonic evolution of the New Mexico region, *in* Mack, G.H. and Giles, K.A., eds., The Geology of New Mexico: A Geologic History: Socorro, NM, New Mexico Geological Society, Special Publication 11, p. 1-34.

Kelley, S., McIntosh, W., Goff, F., Kempter, K., Wolff, J., Esser, R., Braschayko, S., Love, D., and Gardner, J., 2013, Spatial and temporal trends in pre-caldera Jemez Mountains volcanic and fault activity: Geosphere, v. 9, p. 614-646, doi: 10.1130/GES00897.1.

Kingsbury, C.G., Kamo, S.L., Ernst, R.E., Söderlund, U., and Cousens, B.L., 2018, U-Pb geochronology of the plumbing system associated with the Late Cretaceous Strand Fiord Formation, Axel Heiberg Island, Canada: part of the 130-90 Ma High Arctic large igneous province: Journal of Geodynamics, v. 118, p. 106–117, doi: 10.1016/j.jog.2017.11.001.

Knaack C., Cornelius, S., and Hooper, P.R., 1994, Trace element analysis of rocks and minerals by ICP-MS, GeoAnalytical Lab, Washington State University.

L'Heureux, I. and Folwer, A.D., 1994, A nonlinear dynamical model of oscillatory zoning in plagioclase: American Mineralogist, v. 79, p. 885-891.

Le Bas, M.J., Le Maitre, R.W., Streckeisen, A., and Zanettin, B.A., 1986, Chemical classification of volcanic rocks based on the total alkali-silica diagram: Journal of Petrology, v. 27, p. 745-750.

Leudke, R.G., and Smith, R.L., 1978, Map showing distribution, composition, and age of late Cenozoic volcanic centers in Arizona and New Mexico: USGS Miscellaneous Investigations, Map I-1091-A.

Lipman, P.W., 2000, Calderas: *in* Encyclopedia of Volcanoes, H. Sigurdsson, (Ed.), Academic Press, San Francisco, p. 643-662.

Liu, H.-Q., Xu, Y.-G., Tian, W., Zhong, Y.-T., Mundil, R., Li, X.-H., Yang, Y.-H., Luo, Z.-Y., and Shang-Guan, S.-M., 2014, Origin of two types of rhyolites in the Tarim Large Igneous Province: Consequences of incubation and melting of a mantle plume: Lithos, v. 204, p. 59–72, doi: 10.1016/j.lithos.2014.02.007.

Loeffler, B.M., Vaniman, D.T., Baldridge, W.S., and Shafiqullah, M., 1988, Neogene rhyolites of the northern Jemez volcanic field, New Mexico: Journal of Geophysical Research, v. 93, p. 6157–6167, doi: 10.1029/jb093ib06p06157.

Loomis, T., 1982, Numerical simulations of crystallization processes of plagioclase in complex melts: the origin of major and oscillatory zoning in plagioclase: Contributions to Mineralogy and Petrology, v. 81, iss. 3, p. 219-229.

Magnani, M.B., Miller, K.C., Levander, A., and Karlstrom, K.E., 2004, The Yavapai-Mazatzal: A long-lived tectonic element in the lithosphere of southwestern North America: Geological Society of America Bulletin, v. 116, no. 9, p. 1137-1142.

Magnani, M.B., Levander, A., Miller, K.C., Eshete, T., and Karlstrom, K.E., 2005, Seismic investigation of the Yavapai-Mazatzal transition zone and the Jemez Lineament in northeastern New Mexico: The Rocky Mountain Region—An Evolving Lithosphere: Tectonics, Geochemistry, and Geophysics Geophysical Monograph Series, p. 227–238, doi: 10.1029/154gm16.

Manley K., 1982, Geologic map of the Cañones Quadrangle, Rio Arriba County, New Mexico: U.S. Geological Survey Miscellaneous Field Studies Map MF-1440, scale 1:24,000.

Mason, B.G., Pyle, D.M., and Oppenheimer, C., 2004, The size and frequency of the largest explosive eruptions on Earth: Bulletin of Volcanology, v. 66, p. 735-748, doi: 10.1007/s00445-004-0355-9.

McDougall, I., and Harrison, T.M., 1999, Geochronology and thermochronology of the ^{40}Ar/^{39}Ar method: New York, Oxford University Press, 269 p.

Morgan, P., Seager, W.R., and Golombek, M.P., 1986, Cenozoic thermal, mechanical and tectonic evolution of the Rio Grande Rift: Journal of Geophysical Research, v. 91, p. 6263-6276, doi: 10.1029/jb091ib06p06263.

Newhall, C.G., and Self, S., 1982, The volcanic explosivity index (VEI): an estimate of explosive magnitude for historical volcanism: Journal of Geophysical Research, v. 87, p. 1231–1238.

Pallister, J.S., Hoblitt, R.P., and Reyes, A.G., 1992, A basalt trigger for the 1991 eruptions of Pinatubo volcano?: Nature, v. 356, p. 426–428, doi: 10.1038/356426a0.

Pearce, J.A., Harris, N.B.W., and Tindle, A.G., 1984, Trace Element Discrimination Diagrams for the Tectonic Interpretation of Granitic Rocks: Journal of Petrology, v. 25, p. 956–983, doi: 10.1093/petrology/25.4.956.

Pearce, J.A., 1996. A user's guide to basalt discrimination diagrams. In: Wyman, D.A. (Ed.), St. John's, Newfoundland, Canada: Geological Association of Canada Short Course Notes, 12, pp. 79–113.

Phillips, E.H., Goff, F., Kyle, P.R., McIntosh, W.C., Dunbar, N.W., Gardner, J.N., 2007, The ^{40}Ar/^{39}Ar age constraints on the duration of resurgence at the Valles caldera, New Mexico: Journal of Geophysical Research, v. 112, B08201, doi: 10.1029/2006JB004511.

Renne, P.R., Swisher, C.C., Deino, A.L., Karner, D.B., Owens, T.L., DePaolo, D.J., 1998, Intercalibration of standards, absolute ages and uncertainties in ^{40}Ar/^{39}Ar dating: Chemical Geology, v. 145, p. 117-152.

Rollinson, H.R., 1993, Using geochemical data: evaluation, presentation, interpretation: Essex, Longman Scientific and Technical, 352 p.

Rowe, M.C., Wolff, J.A., Gardner, J.N., Ramos, F.C., Teasdale, R., Heikoop, C.E., 2007, Development of a Continental Volcanic Field: Petrogenesis of Pre-caldera Intermediate And Silicic Rocks and Origin of the Bandelier Magmas, Jemez Mountains (New Mexico, USA): Journal of Petrology: v. 48, no. 11, p. 2063-2091.

Rudnick, R.L., and Fountain, D.M., 1995, Nature and composition of the continental crust: A lower crustal perspective: Reviews of Geophysics, v. 33, p. 267–309, doi: 10.1029/95rg01302.

Scherbakov, V.D., Plechov, P.Y., Izbekov, P.E., Shipman, J.S., 2010, Plagioclase zoning as a n indicator of magma processes at Bezymianny Volcano, Kamchhatka: Contributions to Mineralogy and Petrology, v. 162, iss. 1, p. 83-99.

Self, S., Goff, F., Gardner, J.N., Wright, J.V., and Kite, W.M., 1986, Explosive rhyolitic volcanism in the Jemez Mountains: Vent locations, caldera development and relation to regional structure: Journal of Geophysical Research, v. 91, p. 1779-1798, doi: 10.1029/jb091ib02p01779.

Self, S., Wolff, J.A., Spell, T.L., Skuba, C.E., and Morrissey, M.M., 1991, Revisions to the stratigraphy and volcanology of the post-0.5 Ma units and the volcanic section of VC-1 core hole, Valles Caldera, New Mexico: Journal of Geophysical Research, v. 96, no. B3, p. 4107-4116, doi: 10.1029/90jb02090.

Self, S., 2006, The effects and consequences of very large explosive volcanic eruptions: Philosophical Transactions of the Royal Society A: Mathematical, Physical and Engineering Sciences, v. 364, p. 2073-2097, doi: 10.1098/rsta.2006.1814.

Shaw, C.A., and Karlstrom, K.E., 1999, The Yavapai-Mazatzal crustal boundary in the Southern Rocky Mountains: Rocky Mountains Geology, v. 34, no. 1, p. 37-52.

Singer, B.S., and Kudo, A.M., 1986, Assimilation-fractional crystallization of Polvadera Group rocks in the northwestern Jemez Volcanic Field, New Mexico: Contributions to Mineralogy and Petrology, v. 94, p. 374–386, doi: 10.1007/bf00371445.

Smith, R.L., and Bailey, R.A., 1966, The Bandelier Tuff: A study of ash-flow eruption cycles from zoned magma chambers: Bulletin of Volcanology, v. 29, no.1, p. 83-103.

Smith, R.L., and Bailey, R.A., 1968, Resurgent cauldrons: Geological Society of America Memoir, no. 116, p. 613-662.

Smith, G.A., and Lavine, A., 1996, What is the Cochiti Formation?: New Mexico Geological Society Guidebook, v. 47, p. 219-224.

Smith, R.L., Bailey, R.A., and Ross, C.S., 1961, Structural evolution of the Valles caldera, New Mexico, and its bearing on the emplacement of ring dikes: U.S. Geological Survey Professional Paper 424-D, p. 145-149.

Smith, R.L., Bailey, R.A., and Ross, C.S., 1970, Geologic map of the Jemez Mountains, New Mexico, U.S. Geological Survey, Misc Invest Map I-571, Scale 1:250,000.

Spell, T.L., and Harrison, T.M., 1993, 40Ar/39Ar geochronology of the post-Valles caldera rhyolites, Jemez Mountains volcanic field, New Mexico: Journal of Geophysical Research, v. 98, p. 8031-8051.

Spell, T.L., Kyle, P.R., and Baker, J., 1996a, Geochronology and geochemistry of the Cerro Toledo rhyolite: New Mexico Geological Society Guidebook, v. 47, p. 263-268.

Spell, T.L., McDougall, I., and Doulgeris, A.P., 1996b, Cerro Toledo Rhyolite, Jemez volcanic field, New Mexico: ^{40}Ar/^{39}Ar geochronology of eruptions between two caldera-forming events: Geological Society of America Bulletin, v. 108, p. 1549-1566.

Staudacher, T., Jessberger, E.K., Dörflinger, D., and Kiko, J., 1978, A refined ultra high-vacuum furnace for rare gas analysis: Journal of Physics and Earth Sciences Instrumentation, v. 11, p. 781-784.

Sun, S.S., and McDonough, W.F., 1989, Chemical and isotopic systematic of oceanic basalts; implications for mantle composition and processes: In: Magmatism in the ocean basins, Saunders, A.D. and Norry, M.J. (Eds.), Geological Society of London, v. 42, p. 313-345. London.

Tian, W., Campbell, I.H., Allen, C.M., Guan, P., Pan, W., Chen, M., Yu, H., and Zhu, W., 2010, The Tarim picrite–basalt–rhyolite suite, a Permian flood basalt from northwest China with contrasting rhyolites produced by fractional crystallization and anatexis: Contributions to Mineralogy and Petrology, v. 160, p. 407–425, doi: 10.1007/s00410-009-0485-3.

Tepley, F.J., Davidson, J.P., Tilling, R.I., and Arth, J.G., 2000, Magma Mixing, Recharge and Eruption Histories Recorded in Plagioclase Phenocrysts from El Chichón Volcano, Mexico: Journal of Petrology, v. 41, p. 1397–1411, doi: 10.1093/petrology/41.9.1397.

Warshaw, C.M., and Smith, R.L., 1988, Pyroxenes and fayalites in the Bandelier Tuff, New Mexico: Temperatures and comparison with other rhyolites: American Mineralogist, v. 73, p. 1025–1037.

Wendt, I., and Carl, C., 1991, The statistical distribution of the mean squared weighted deviation: Chemical Geology: Isotope Geoscience section, v. 86, iss. 4. P. 275-285.

WoldeGabriel, G., Warren, R.G., Broxton, D.E., Vaniman, D.T., Heizler, M.T., Kluk, E.C., and Peters, L., 2001, Episodic volcanism, petrology, and lithostratigraphy of the Pajarito Plateau and adjacent areas of the Espanola Basin and the Jemez Mountains, in, Crumpler, L.S., and Lucas, S. (Eds.), Volcanology in New Mexico: New Mexico Museum of Natural History and Science Bulletin, v. 18, p. 97-129.

Wolff, J.A., Rowe, M.C., Teasdale, R., Gardner, J.N., Ramos, F.C., and Heikoop, C.E., 2005, Petrogenesis of pre-caldera mafic lavas, Jemez Mountains Volcanic Field (New Mexico, USA): Journal of Petrology, v. 46, p. 407-439.

CURRICULUM VITAE

Kelsy Jo Konkright
kjkonkright@gmail.com

Education

University of Nevada Las Vegas (UNLV) **Las Vegas, Nevada, USA**
Master of Science, Geoscience (Focus: Volcanology/Igneous Petrology) 2016 – Present

Thesis: Petrogenesis of the El Rechuelos Rhyolite, Jemez Mountains Volcanic Field, New Mexico, USA

Honors

AEG Student Night Best Poster, 2018
Geosymposium Best Poster Research Presentation, 2018
Bernada French Scholarship, Fall 2016, Spring 2018, Fall 2018
Edwards and Olswang Geology Scholarship, Spring 2017
Graduate Access Funds Scholarship, Fall 2016, Spring 2017

University of Alaska Anchorage (UAA) **Anchorage, Alaska, USA**
Bachelor of Science, Geological Sciences 2013 – 2016

Honors

Graduated Magna Cum Laude
Dean's List or higher recognition each semester
Geological Society of America Field Camp Scholarship, 2016

Abstracts and Publications

Konkright, K.J. and Spell, T.L., 2018, Petrogenesis of the El Rechuelos Rhyolite, Jemez Mountains Volcanic Field, New Mexico, USA: Geological Society of America Abstracts with Programs. Vol. 50, No. 5, doi: 10.1130/abs/2018RM-314206

Taylor, W.J., Chameroy, E.J., Ely, R.M., Konkright, K.J., Medema, J., Peck, A.M., and Rafferty, K.C., 2017, Seismic hazard and paleoseismicity in southern Nevada: the California Wash Fault: Geological Society of America Abstracts with Programs. Vol. 49, No. 6, doi: 10.1130/abs/2017AM-300654